MCDEVITT, DANIEL. Proton Radiative Capture on ^{48}Ti. (Under the direction of Dr. G. E. Mitchell and Dr. J. F. Shriner, Jr.) The ^{48}Ti(p,γ)^{49}V reaction was studied in the energy range E_p = 2.0–2.8 MeV. This research was performed at the High Resolution Laboratory at Triangle Universities Nuclear Laboratory. Capture spectra were obtained for 27 compound nuclear resonances whose resonance parameters (energy, spin, parity, and particle widths) had been determined in earlier experiments. The γ rays were measured with a Compton-suppressed HPGe detector. A total of ten $1/2^+$ resonances, nine $1/2^-$ resonances and eight $3/2^-$ resonances were studied.

The primary motivation for these measurements was to provide a data set suitable for testing the applicability of conventional statistical models in this mass region. A secondary motivation was to evaluate the "low level population" method (which works very well in heavier nuclei) in this mass region. The relative populations of 10 of the first 12 excited states of ^{49}V were determined (the relative populations of two of the low-lying states could not be obtained due to γ-ray resolution limitations). The average relative populations were similar for the three types of resonances.

The experimental relative populations were compared with calculations performed with the statistical model code DICEBOX. Results for a variety of radiative strength function models yielded qualitatively similar results. These simulations agree only qualitatively with the experimental relative populations. Although the simulations suggest that the low level population method may work in this nuclide, the experimental results are at best ambiguous. Thus the statistical approach provides a reasonable qualitative description (but not a quantitative description) of the relative population of low-lying states in ^{49}V.

PROTON RADIATIVE CAPTURE ON ^{48}Ti

by

DANIEL B. MCDEVITT

A dissertation submitted to the Graduate Faculty of
North Carolina State University
in partial fulfillment of the
requirements for the Degree of
Doctor of Philosophy

Department of Physics

Raleigh

2003

APPROVED BY:

Mohamed A. Bourham	D. Ronald Tilley
Gary E. Mitchell, Co-chair of Advisory Committee	John F. Shriner, Jr., Co-chair of Advisory Committee

To my brother

Charles T. McDevitt

without whose suggestion to me
while serving my country in South
Korea this endeavor would probably
not have been undertaken.

Biography

Daniel B. McDevitt

Personal:

Born 21 May 1968, Pocatello, Idaho

Education:

B.S. in nuclear engineering, University of Arizona, 1992

B.S. in electrical engineering, University of Arizona, 1992

M.S. in physics, North Carolina State University, 2000

Academic Positions:

Teaching Assistant, North Carolina State University, 1996-2000

Research Assistant, North Carolina State University, 2000-2003

Military

Commissioned, 2LT, United States Army Signal Corps, December 1992

1993–1994, Tongducheon and Song–Ji–Ri, South Korea, 122d Signal Battalian and 5/17th Cavalry

1995, Guantanamo Bay, Cuba, Operation Sea Signal

1996 Fort Lewis, WA 2–8 Field Artillery

Acknowledgments

Many thanks are owed to Dr. Gary E. Mitchell for his patience, valued advice and assistance during data analysis and dissertation preparation. His many approaches to problem–solving are especially appreciated. I am also grateful for Dr. John F. Shriner, Jr. for his insights into the experimental equipment and methods and for detailed advice concerning the dissertation.

A huge debt of gratitude is owed the TUNL technical staff. Without their perseverance and willingness to interrupt their schedules to correct many equipment problems, this thesis would not have been possible. Richard O'Quinn's valued help with equipment and timely sense of humor on many trying occasions is much appreciated. Bret Carlin and Patrick Mulkey deserve credit for their efforts in helping repair numerous electronic circuits. Bret Carlin's help is especially appreciated since many times it was required just as he was leaving for home. I am especially indebted to Sidney Edwards for his willingness to interrupt his retirement to repair the VAX system. Robert Timberlake and the other Duke Instrument shop employees willingness to interrupt their work to repair broken equipment is greatly appreciated. I am much indebted to Paul Carter for help in troubleshooting numerous accelerator related problems and for his commitment to helping me collect data by solving a three-month long problem in the three remaining days prior to his retirement. Many thanks to John Dunham for his assistance with many accelerator repairs.

Most especially I want to thank the tireless efforts of Chris Westerfeldt. His hard efforts significantly reduced my time here. TUNL would be a poorly functioning laboratory without his dedication to work and his problem solving abilities. His many informal Automechanics 101 lectures will also never be forgotten.

I'm grateful for my colleagues Bill Beal, Stephen Lokitz and Lance McLean for helping collect data and inadvertently setting the TUNL record for longest continuous

time spent accumulating data. Undraa Agvaanluvsan's candid advice during discussions of nuclear theory is also much appreciated.

My family has been my rock of stability during this long and trying time. My gratitude for their patience and support cannot be adequately expressed in words. I look forward to returning the many favors they granted me over the course of this often–times difficult period.

Contents

List of Tables

List of Figures

Chapter 1

Introduction

Nuclear level densities and radiative strength functions have received increased interest recently. Nuclear level densities are important for understanding nuclear reaction rates in general and are particularly important (and uncertain) for nuclei far from stability. Nuclear structure physicists have focused recently on properties of nuclei far from stability – this is exemplified by the proposed Rare Isotope Accelerator (RIA). Nuclear level densities have been well studied for stable nuclei, and semi-empirical approaches have been developed that work reasonably well. However, the physical interpretation of the parameters used in these phenomenological models is unclear. Therefore extrapolation to nuclei far from stability is questionable. Recent efforts have focused on models with a clearer physical interpretation of the model parameters, such as the Shell Model Monte Carlo method. These models have had success and also provide explicit predictions for detailed behavior such as the parity dependence of nuclear level densities. To examine such detailed properties require the determination of the quantum numbers of individual nuclear states. An effort to develop a rapid method for the determination of the spin of nuclear resonances was one of the motivations for this experiment.

There is also a recent increase in interest in nuclear astrophysics. The s- and r- processes that involve medium-mass nuclei are determined by the competition between neutron

capture and β decay, and the neutron-capture cross section is determined in large part by the level density and the radiative strength function. The networks that are involved in stewardship applications, such as the radiochemistry of archival nuclear data, are very similar to the networks involved in nucleosynthesis. Thus nuclear level densities and radiative strength functions are important for both pure and applied physics.

The radiative strength function is relatively better understood for higher energies, for heavier nuclei, and for E1 transitions. However, the primary interest for astrophysics, for RIA, and for stewardship applications is for light and medium nuclei. Since neutron capture is of crucial interest, the behavior of the radiative strength functions at low energies is very important.

Level densities in light and medium nuclei seem to be better understood than radiative strength functions in this mass region. In the present experiment the proton capture reaction was studied for compound nuclear (CN) resonances in ^{49}V. Our group had previously studied elastic and inelastic scattering on ^{48}Ti and had obtained a large amount of information on the properties of the CN resonances in ^{49}V. The goal of the present experiments was to obtain detailed capture spectra from resonances of known spin and parity and to measure a sufficient number of resonances in order to reduce effects of fluctuations from resonance to resonance. Such a systematic study has apparently never been performed in this mass region.

An additional issue that is important (and contentious) is the degree to which statistical models should (or do) work in this mass region. It is well established that the CN resonances in this mass region obey Random Matrix Theory, a purely statistical theory. However, the status of the radiative decay is less well established. The present results are compared with the extreme statistical model as formulated in the computer program DICEBOX.

These data can also be used to test whether a method of determining the spins of resonances that has proven very successful in neutron capture in heavier nuclei also

applies in medium nuclei. This method is called the low level population (LLP) method; the method relies on the fact that if one starts from CN resonances with different spin and the radiative decay is purely statistical, then the low-lying levels with spin closer to the resonance spin are more strongly populated. In practice, to enhance the effect one measures transitions from low-lying states with quite different spins and determines the ratio of the intensities. This simple method has been shown to work extremely well for neutron capture in heavier nuclei such as silver. Since the resonances in ^{49}V were known to behave statistically and DICEBOX simulations suggested that this method might work in ^{49}V, the method was evaluated using the capture spectra. A rapid and accurate method of determining resonance spins would be of significant value in purifying the existing proton resonance data sets and therefore in testing detailed predictions of level density models.

This thesis is composed of 9 chapters and 5 appendices. Chapter 2 provides background concerning the capture reaction and the general characteristics of radiative decay. Level densities are briefly summarized in Chapter 3, including model development from Bethe's constant temperature function through the development of the Shell Model Monte Carlo method. The standard models for the radiative strength functions are also briefly discussed. Chapter 4 describes the LLP method and the computer code DICEBOX that simulates the radiative decay using Monte Carlo methods. The experimental equipment and data collection techniques are discussed in Chapter 5. Preliminary analysis of γ-ray spectra, including the fits of the spectral lines and the energy and efficiency calibrations of the γ-ray detectors, are discussed in Chapter 6. Chapter 7 presents the experimental results for the relative population of the low-lying levels. In Chapter 8 these experimental results are compared with various model calculations in which the radiative strength functions are varied. In addition, these results are compared with DICEBOX predictions, and the LLP method is evaluated. Chapter 9 provides a summary and conclusions.

More extensive results from the experimental measurements and the model calculations are provided in the appendices. Appendix A lists the intensities of the 33 γ rays

studied for each of the 27 ^{49}V resonances measured. Tables and figures for the experimental relative population of the low-lying levels are presented for each of the 27 resonances in Appendix B. Appendix C displays the DICEBOX predictions for the relative populations in the same format as in Appendix B. In Appendix D the experimental results and DICEBOX predictions are compared for specific tests of the LLP method. The last appendix, Appendix E, shows the excitation functions used in selecting the 27 ^{49}V resonances studied.

Chapter 2

Capture Reactions

As discussed in the Introduction, a primary motivation for the present proton capture measurements was to evaluate a method for determining the total angular momentum and parity of resonances. This chapter will first review compound nuclear resonances, including discussion of angular momentum and cross sections. The focus is then on the capture reaction and a description of the electromagnetic transitions in the exit channel.

2.1 Resonance Formalism

The observation of neutron cross sections that were larger than nuclear dimensions [Fer34] provided the first experimental evidence for the formation of nuclear resonances. Subsequent measurements with protons by Hafsted and Tuve [Haf35] and by many others provided a firm experimental foundation. The widths of these sharp, well isolated resonances indicated a lifetime of the order of $\sim 10^{-15}$ seconds, much longer than the time needed to traverse the nuclear diameter ($\sim 10^{-21}$ seconds).

Bohr [Boh36] proposed the independence hypothesis – that the formation and decay of these "quasi-stationary" (compound nuclear) states are independent. In a typical reaction of this type, projectile a is incident on target nucleus X, forming a compound nucleus C^* which subsequently decays into a residual nucleus Y and decay product b. This

is represented as $a + X \rightarrow C^* \rightarrow b + Y$. Bohr's model followed from the assumption of strong, very short range internucleon forces. The initial energy of the projectile is rapidly shared among the target nucleons, which strongly inhibits immediate decay of the compound nucleus. This virtual or "quasi-stationary" state subsequently decays into reaction products. These resonances are identified by large, localized increases in the cross section of a particular reaction at particular energies. Due to the finite lifetime of a resonance there is an uncertainty in its energy; this width Γ [Bla92] is defined by

$$\Gamma = \frac{\hbar}{\tau}, \tag{2.1}$$

where τ is the mean lifetime of the compound nucleus formed.

These resonances form a discrete spectrum at energies above the nucleon separation energy in the compound nucleus. At higher energies the average width becomes comparable to the average spacing between adjacent levels, and the levels overlap. Discrete compound states in the ^{48}Ti(p,γ) reaction are characterized by several quantum numbers – total angular momentum J, parity π, and isospin T – that reflect the fundamental and approximate symmetries of the nucleus.

Following Bohr's compound nuclear hypothesis there were many theoretical attempts to model resonance reaction cross sections. The approach that is normally used for proton and neutron resonance reactions is the R-matrix theory by Wigner and Eisenbud [Wig47]. This approach describes the resonance reaction cross sections with a small set of observables. Blatt and Biedenharn [Bla52] used the collision matrix formalism of Wigner and Eisenbud to obtain a general expression for the differential cross section for resonance reactions. Lane and Thomas extended the theory to capture reactions and provided a detailed description of R-matrix theory [Lan58]. Vogt [Vog59] provides an excellent review of this approach. From this point on in this chapter, the discussion is restricted to the proton capture reaction.

2.1.1 Angular Momentum Coupling

It is convenient to describe the formation and decay of resonances in terms of entrance and exit channels. The entrance channel for a proton-induced reaction involves three different angular momenta: the spin i of the incident proton, the spin A of the target nucleus, and the orbital angular momentum ℓ between the incident proton and the target. These three angular momenta may be coupled by first combining any two of the three angular momenta to an intermediate value and then combining with the remaining angular momentum. For processes that do not involve polarization, the channel spin representation is the most convenient. The angular momenta of the target and projectile are combined to form the channel spin s, which is then combined with the orbital angular momentum ℓ to form the total angular momentum J:

$$\vec{J} = (\vec{i} + \vec{A}) + \vec{\ell} = \vec{s} + \vec{\ell}. \tag{2.2}$$

In the capture reaction, the compound nucleus decays by emitting a γ ray that carries away angular momentum L and leaves the nucleus in a state C. The angular momentum relation for the exit channel is

$$\vec{J} = \vec{C} + \vec{L}. \tag{2.3}$$

An illustration of the angular momenta involved in this type of reaction is shown in Figure 2.1.

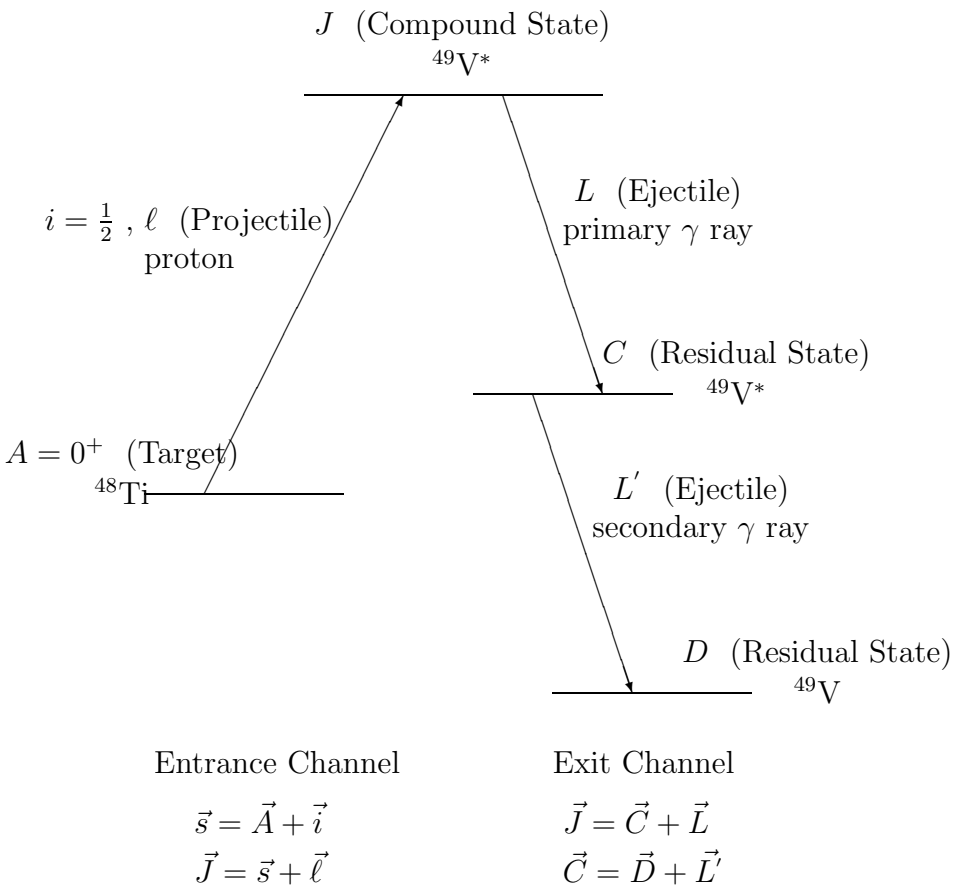

Figure 2.1: Angular momentum coupling scheme. The coupling scheme is shown for the ^{48}Ti(p,γ) reaction in the channel spin representation. A proton (projectile) with intrinsic spin 1/2 and orbital angular momentum ℓ couples with a ^{48}Ti nucleus (target) of spin 0 to form an excited state of ^{49}V (compound state) with spin J. In the exit channel, the excited state of ^{49}V (compound state) with spin J decays to another state of ^{49}V (residual state) with spin C by emission of a γ ray carrying L units of angular momentum. In this example, the residual state C decays to another state of ^{49}V (also labeled as a residual state) with spin D by emission of a secondary γ ray carrying $L^{'}$ units of angular momentum.

2.1.2 Resonance Cross Sections

For an unpolarized beam, the differential cross section can be written as

$$\begin{aligned}\frac{d\sigma}{d\Omega} &= \left(\frac{\lambda\!\!\!^{-}}{\hat{\imath}\hat{A}}\right)^2 \sum (-1)^{s-\ell_1+\ell_2-2J_2+C-L_1+L_2}\, \overline{Z}(\ell_1\, J_1\, \ell_2\, J_2; s\, k) \\ &\quad \overline{Z}_1(L_1\, J_1\, L_2\, J_2; C\, k)\, \langle C\, L_1|S|J_1\, s_1\, \ell_1\rangle \langle C\, L_2|S|J_2\, s_2\, \ell_2\rangle^* \\ &\quad Q_k P_k(\cos\theta). \end{aligned} \tag{2.4}$$

The summation is over s, ℓ_1, ℓ_2, L_1, L_2, J_1, J_2, and k; the symbol $\hat{a}$ denotes $\sqrt{2a+1}$. This equation was obtained by Blatt and Biedenharn [Bla52] with a correction by Huby [Hub54]. In equation (2.4), θ is the angle between the beam direction and the γ-ray detector axis, P_k is the Legendre polynomial of degree k, Q_k is the correction coefficient for the finite detector size, and $\lambda\!\!\!^{-}$ is the reduced wavelength of the incident particle.

The two Z terms, $\overline{Z}$ and $\overline{Z}_1$, account for the angular momentum combinations in the entrance and exit channels, respectively. The $\overline{Z}$ term was defined by Blatt and Biedenharn [Bla52] and modified by Huby [Hub54]. The $\overline{Z}_1$ term is a modified version [Bie60] of the coefficient proposed by Sharpe [Sha54] that accounts for γ rays in the exit channel [Fer65, Vav96]. The $\overline{Z}$ coefficients are zero unless $\vec{J}_1 = \vec{s} + \vec{\ell}_1$ and $\vec{J}_2 = \vec{s} + \vec{\ell}_2$ and thus reflect conservation of angular momentum; similarly the $\overline{Z}_1$ coefficients are zero unless $\vec{J}_1 = \vec{C} + \vec{L}_1$ and $\vec{J}_2 = \vec{C} + \vec{L}_2$.

The dynamics for the reaction in Eq. (2.4) is contained in the scattering matrix [Wig47]. Biedenharn [Bie60] showed that if only a single level contributes to the cross section, the scattering matrix element is

$$\langle C\, L_1|S|J_1\, s_1\, \ell_1\rangle \approx \frac{e^{i\xi_\ell} g_{s\ell} g_L}{E_r - E - \frac{i\Gamma}{2}}. \tag{2.5}$$

In this equation, Γ is the resonance total width, and $g_{s\ell}$ and g_L are the square roots of the partial widths for the proton entrance channel and the γ-ray exit channel. The Breit-Wigner capture cross section is [Bla92]

$$\sigma_{cap} = \pi \lambda\!\!\!^{-2} \frac{\Gamma_p \Gamma_\gamma}{[(E_p - E_r)^2 + \frac{\Gamma^2}{4}]}, \tag{2.6}$$

where Γ_p and Γ_γ are the partial widths for the incident proton and the emitted γ ray, and $\lambda\!\!\!^{-}$ is the reduced wavelength of the incident proton.

2.2 Radiative Transitions

2.2.1 Selection Rules

For radiative transitions from an initial state J_i to a final state J_f, conservation of angular momentum requires that

$$\vec{J_i} = \vec{J_f} + \vec{L}. \tag{2.7}$$

The allowed values for the total angular momentum L and the projection on the z-axis M are therefore

$$|J_i - J_f| \leq L \leq J_i + J_f, \tag{2.8}$$

$$M = m_i - m_f, \tag{2.9}$$

where m_i and m_f are the z-projections of the initial and final state total angular momenta.

If both $J_i = 0$ and $J_f = 0$, there will be no transitions consisting of a single γ ray between the states [Bla92]. Although such γ-ray transitions are forbidden by the selection rules, de-excitation can occur through other processes. This restriction only applies for 0 to 0 transitions: single γ-ray transitions do occur for $J_f = J_i$ as long as J is nonzero.

Since parity is conserved in electromagnetic transitions, the type of multipole radiation is further restricted. When an initial state with parity π_i decays to a final state with parity π_f by emission of a γ ray of multipolarity L, conservation of parity requires

Table 2.1: Example of possible multipole values.

J_i^π	J_f^π	Possible EL	Possible ML
$\frac{5}{2}^+$	$\frac{7}{2}^-$	$E1, E3, E5$	$M2, M4, M6$
$\frac{5}{2}^-$	$\frac{7}{2}^-$	$E2, E4, E6$	$M1, M3, M5$
$\frac{5}{2}^+$	$\frac{7}{2}^+$	$E2, E4, E6$	$M1, M3, M5$
$\frac{5}{2}^-$	$\frac{7}{2}^+$	$E1, E3, E5$	$M2, M4, M6$

$$\pi_i = \pi_f \pi_L. \tag{2.10}$$

The parity π_L depends on whether the γ ray is electric or magnetic in nature. For a γ ray of electric character, $\pi_L = (-1)^L$; for a γ ray of magnetic character, $\pi_L = (-1)^{(L+1)}$. As an example of angular momentum and parity conservation applied to γ-ray transitions, the possible transitions involving $J_i = \frac{5}{2}$ and $J_f = \frac{7}{2}$ are listed in Table 2.1.

2.2.2 Multipole Moments

The previous section used symmetry conservation laws to determine selection rules for radiative decay. These rules define the *possibility* for decay. However, one would like to know the *probability* for decay. The probability of emission is directly related to the rate of energy emitted for the particular radiation. This energy rate of emission is determined by the multipole moments produced by the charges and currents of the emission source.

To model the charges and currents, consider the case of a single spinless nucleon of mass M and charge e, moving in a potential. The equations describing the charge density ρ and current density $\vec{j}$ as the nucleon makes a transition from an initial state φ_i to a final state φ_f are [Bla92]

$$\rho = e\,\varphi_f^*(\vec{r})\varphi_i(\vec{r}), \tag{2.11}$$

$$\vec{j} = \frac{e}{2M}\left[\varphi_f^*(\vec{p}\,\varphi_i) + (\vec{p}\,\varphi_f)^*\varphi_i\right], \tag{2.12}$$

where $\vec{p} = -i\hbar\vec{\nabla}$ is the linear momentum operator of the nucleon. (The equations involving electromagnetic theory in this subsection and the next are expressed in Gaussian units.)

For a nucleus of mass A and charge Z, the total charge and current densities are the sum of the contributions of the individual nucleons given in equation 2.11 and 2.12. The nucleons are considered point particles moving independently in a potential well; quark or meson-exchange contributions to the multipole moments are neglected. The long wavelength approximation $\kappa R \ll 1$ is assumed, with κ the wave number of the emitted radiation and R the nuclear radius. In other words, the radiation wavelength is considered much larger than the size of the nucleus. This is a good approximation for the γ-ray energies in the present experiments.

For a classical system, the electric and multipole moments, Q_{LM} and M_{LM}, are related to the current and charge density by [Bla92]

$$Q_{LM} = \int r^L\, Y_{LM}^*(\theta,\phi)\,\rho(\vec{r})\,dV, \tag{2.13}$$

and

$$M_{LM} = -\frac{1}{c(L+1)}\int r^L\, Y_{LM}^*(\theta,\phi)\vec{\nabla}\cdot(\vec{r}\times\vec{j}\,)\,dV. \tag{2.14}$$

There is also an intrinsic spin contribution arising from the proton and neutron nuclear magnetic moments μ_N. This is characterized by the magnetization $\vec{M}$. The classical description of the electric and magnetic multipole moments for this effect are [Bla92]

$$Q'_{L,m} = -\frac{i\kappa}{L+1}\int r^L\, Y^*_{Lm}(\theta,\phi)\,\vec{\nabla}\cdot(\vec{r}\times\vec{M})\,dV, \tag{2.15}$$

$$M'_{L,m} = -\int r^L\, Y^*_{L,m}(\theta,\phi)\,\vec{\nabla}\cdot\vec{M}\,dV. \tag{2.16}$$

The quantum counterparts to equations (2.13) and (2.14) are obtained by substituting equations (2.11) and (2.12) into these equations. The results are [Bla92]

$$\hat{Q}_{Lm} = e\sum_{k=1}^{\mathrm{Z}}\int r_k^L\, Y^*_{Lm}(\theta_k,\phi_k)\varphi_f^*\varphi_i\,dV, \tag{2.17}$$

and

$$\hat{M}_{Lm} = -\frac{1}{L+1}\frac{e\hbar}{2Mc}\sum_{k=1}^{\mathrm{Z}}\int r_k^L\, Y^*_{Lm}(\theta_k,\phi_k)\,\vec{\nabla}\cdot(\varphi_f^*\vec{L}_k\varphi_i)\,dV, \tag{2.18}$$

where $\vec{L}_k = -i\vec{r_k}\times\vec{\nabla}_k$ is the angular momentum operator.

For the intrinsic spin contributions, the quantum description requires replacing the magnetization with the magnetization density $\vec{M}(i,f;\vec{r})$ [Bla92]:

$$\vec{M}(i,f;\vec{r}) \;=\; \frac{e\hbar}{2Mc}\,\mu\,\{\varphi_f^*\vec{\varrho}\varphi_i\}, \tag{2.19}$$

where μ is the magnetic moment of the particle expressed in Bohr magnetons ($\mu = 2.78$ or -1.91 for a proton or neutron, respectively), and $\vec{\varrho}$ is the Pauli spin operator with components σ_x, σ_y, and σ_z. The brace in (2.19) denotes a sum over the two spin values.

Substituting into Eqs. (2.15) and (2.16) yields the quantum expressions for the electric and magnetic multipole moments for the intrinsic spin magnetization:

$$\hat{Q}'_{Lm} = -\frac{i\kappa}{L+1}\,\frac{e\hbar}{2Mc}\sum_{k=1}^{A}\mu_k\int r_k^L\, Y^*_{Lm}(\theta_k,\phi_k)\,\vec{\nabla}\cdot(\varphi_f^*\vec{r}_k\times\vec{\sigma}_k\varphi_i)\,d\tau, \tag{2.20}$$

and

$$\hat{M'}_{Lm} = -\frac{e\hbar}{2Mc}\sum_{k=1}^{A}\mu_k \int r_k^L\, Y^*_{Lm}(\theta_k,\phi_k)\,\vec{\nabla}\cdot(\varphi_f^*\vec{\varrho}_k\varphi_i)\,d\tau. \tag{2.21}$$

It should be noted that in equations (2.20) and (2.21) the integrations are over all of the nucleons. μ_k is the magnetic moment (intrinsic spin component of the magnetic moment) of the k^{th} nucleon, measured in Bohr magnetons, and $\vec{\varrho}_k$ is the corresponding Pauli spin operator. The integrations in equations 2.13 and 2.14 are over only the protons. Collectively the equations (2.17), (2.18), (2.20), and (2.21) relate the type of radiation to the charge and spin distributions of the nucleus in its initial and final state.

2.2.3 Transition Probabilities

The present goal is to determine the probability of emission for a photon of given energy, multipole, and electric or magnetic character. To achieve this one starts with the Poynting vector. At large distances from the nucleus the energy flow is

$$|\vec{S}| \;\cong\; \frac{c}{4\pi}\vec{E}^2 \;\cong\; \frac{c}{4\pi}\,\vec{H}^2, \tag{2.22}$$

where $|\vec{S}|$ has dimensions energy/area/time. $\vec{E}$ and $\vec{H}$ are the time-varying electric and magnetic fields, respectively. For pure electric and magnetic multipoles, the energy $U_M(\ell,m;\Omega)\,d\Omega$, emitted per second through solid angle $d\Omega$ (the emission rate) is [Bla92]

$$U_E(L,m;\theta\phi) \;=\; \frac{c}{2\pi\kappa^2}\,Z_{Lm}(\theta\phi)\,|a_E(L,m)|^2, \tag{2.23}$$

$$U_M(L,m;\theta\phi) \;=\; \frac{c}{2\pi\kappa^2}\,Z_{Lm}(\theta\phi)\,|a_M(L,m)|^2. \tag{2.24}$$

Here $Z_{Lm}(\theta\phi)$ is the angular distribution function containing the angular components (see

[Bla92], Chapter XII, section B), and κ is the wave number of the electromagnetic radiation. $a_E(L,m)$ and $a_M(L,m)$ are the amplitudes of the electric and magnetic radiations:

$$a_E(L,m) = \frac{-4\pi\kappa^{L+2}}{(2L+1)!!}\left(\frac{L+1}{L}\right)^{1/2}\left(\hat{Q}_{Lm} + \hat{Q}'_{Lm}\right), \tag{2.25}$$

$$a_M(L,m) = \frac{4\pi}{(2L+1)!!}\left(\frac{L+1}{L}\right)^{1/2}\left(\hat{M}_{Lm} + \hat{M}'_{Lm}\right), \tag{2.26}$$

where $(2L+1)!! \equiv 1 \cdot 3 \cdot 5 \cdots (2L+1)$.

The probability for emission of one quanta of a particular energy per unit time is obtained by dividing the emission rate, equations (2.23) and (2.24), by $\hbar\omega$. Combining equations (2.23), (2.24), (2.25), and (2.26) then yields the transition probabilities $T_E(Lm)$ and $T_M(Lm)$ for electric and magnetic multipoles [Bla92]:

$$T_E(L,m) = \frac{8\pi(L+1)}{\hbar L[(2L+1)!!]^2}\left(\frac{E_\gamma}{\hbar c}\right)^{2L+1}\left|Q_{Lm} + Q'_{Lm}\right|^2, \tag{2.27}$$

$$T_M(L,m) = \frac{8\pi(L+1)}{\hbar L[(2L+1)!!]^2}\left(\frac{E_\gamma}{\hbar c}\right)^{2L+1}\left|M_{Lm} + M'_{Lm}\right|^2, \tag{2.28}$$

where $\mathrm{E}_\gamma = \kappa\hbar c$.

Equations (2.27) and (2.28) can be combined to form a general expression for the probability per unit time of the emission of a photon of energy E_γ and character XL:

$$T_{fi} \equiv \frac{\Gamma_\gamma}{\hbar} = \frac{8\pi(L+1)}{\hbar L[(2L+1)!!]^2}\left(\frac{E_\gamma}{\hbar c}\right)^{2L+1} B(XL). \tag{2.29}$$

T_{fi} is the inverse of the mean life τ, and X represents the appropriate electric E or magnetic M multipole type. $B(XL)$, the sum of the squares of the appropriate (electric or magnetic)

multipole moments, contains the information about the nuclear processes, while the other factors in (2.29) are kinematic. B is called the reduced transition probability.

Determination of $B(XL)$ requires the initial and final state wave functions. However, estimates for $B(XL)$ can be obtained from models. Weisskopf [Wei51] provided estimates that give a reasonable comparison of relative transition rates [Kra88]. Weisskopf assumed that the transitions were the result of a single proton moving independently in the nucleus within a square well potential. His estimates were

$$B_W(EL) = \frac{(1.2)^{2L}}{4\pi}\left(\frac{3}{L+3}\right)^2 A^{2L/3}\,\mathrm{e}^2\mathrm{fm}^{2L} \tag{2.30}$$

for electric multipole radiation, and

$$B_W(ML) = \frac{10}{\pi}(1.2)^{2L}\left(\frac{3}{L+3}\right)^2 A^{(2L-2)/3}\,\mu_\mathrm{N}^2\mathrm{fm}^{2L-2} \tag{2.31}$$

for magnetic multipole radiation. For the first few values of XL, the Weisskopf estimates are:

$$\begin{aligned}
B_W(E1) &= 0.06446A^{2/3}\,\mathrm{e}^2\mathrm{fm}^2\\
B_W(E2) &= 0.05940A^{4/3}\,\mathrm{e}^2\mathrm{fm}^4\\
B_W(E3) &= 0.05940A^{2}\,\mathrm{e}^2\mathrm{fm}^6\\
B_W(M1) &= 1.790\,\mu_\mathrm{N}^2\\
B_W(M2) &= 1.650A^{2/3}\,\mu_\mathrm{N}^2\mathrm{fm}^2\\
B_W(M3) &= 1.650A^{4/3}\,\mu_\mathrm{N}^2\mathrm{fm}^4.
\end{aligned} \tag{2.32}$$

Taken together with the general expression for transition probabilities, Eq. (2.29), several results are clear: For the same multipole, electric transitions are strongly favored over magnetic. For the same type of transition (electric or magnetic) the lowest order allowed multipole is strongly favored. For a given L, higher energy transitions are favored by the term $\left(\frac{E_\gamma}{\hbar c}\right)^{2L+1}$.

E(L) transitions are expected to be $\sim 10^5$ stronger than E(L+1) transitions, and M(L) transitions are similarly preferred over M(L+1) transitions. E(L) transitions are $\sim 10^2$ stronger than corresponding M(L) transitions [Kra88]. However, the parity selection rules discussed earlier show that E(L) transitions will compete with M(L+1) transitions and M(L) with E(L+1) transitions. In the former case, E(L) transitions will strongly dominate the M(L+1) transitions: the observed multipole radiation is essentially pure EL. The latter case is not as clear: the E(L+1) contribution may be comparable with the M(L) contribution. The mixture of the two multipoles is expressed as a mixing ratio δ:

$$\delta_{E2/M1} \equiv \sqrt{\frac{\Gamma_{E2}}{\Gamma_{M1}}}, \tag{2.33}$$

and

$$\delta_{E3/M2} \equiv \sqrt{\frac{\Gamma_{E3}}{\Gamma_{M2}}}. \tag{2.34}$$

The phase convention is given by Rose and Brink [Ros67].

2.2.4 Branching Ratios

As illustrated in the ^{49}V decay scheme, Fig. 2.2, there may be several γ-ray transitions from a particular state. For example, the 1140.53-keV state decays to four lower energy states. The probability for decay to a particular final state is called the branching ratio. The branching ratios for the decay of the 1140.53-keV state are listed in Table 2.2. The same information is often expressed in terms of "relative intensities;" typically the most intense γ ray is assigned a relative intensity of 100. Relative intensities for these four γ rays are also listed in Table 2.2.

Table 2.2: Branching ratios and relative intensities for the 1140.53-keV level in ^{49}V [Nud03].

γ-ray Energy (keV)	Multipolarity	Intensity	Branching Ratio
392.7	$M1 + E2$	10.5 ± 1.0	0.056 ± 0.005
987.61	$E1 + M2$	31.4 ± 1.7	0.168 ± 0.008
1049.79	$E1 + M2$	44.5 ± 2.1	0.24 ± 0.01
1140.7	$E1 + M2$	100. ± 4.	0.536 ± 0.012

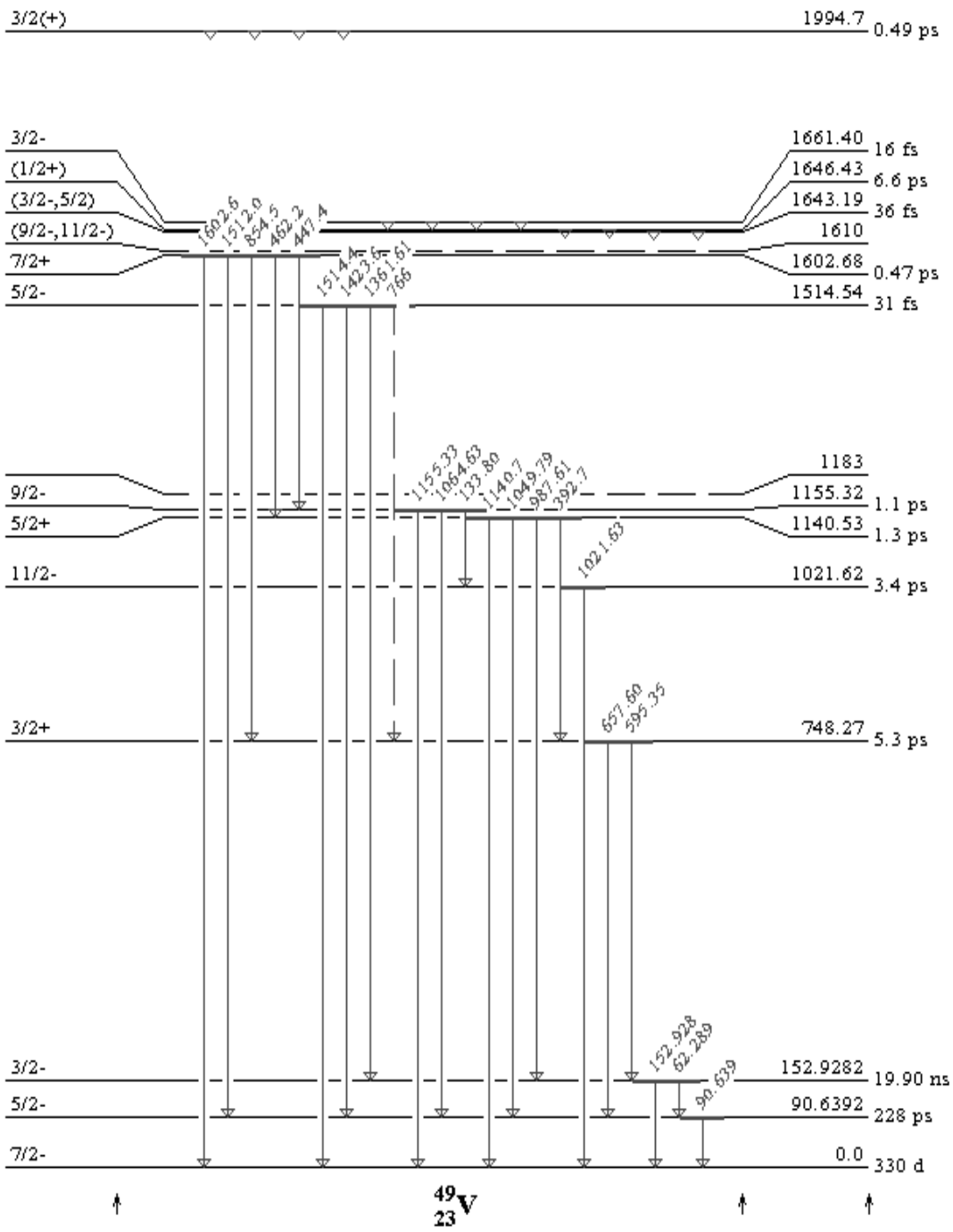

Figure 2.2: Low-lying levels in ^{49}V.

Chapter 3

Level Densities and Radiative Strength Functions

Statistical descriptions play an important role in understanding many aspects of nuclear physics. For γ-ray transitions, the radiative strength function $f_{XL}^{J_i^\pi}(E_\gamma)$ is one key property. The radiative strength function can be related to the average radiative width of type XL

$$< \Gamma_{XL}^{J_i^\pi} > = \frac{f_{XL}^{J_i^\pi}(E_\gamma)\, E_\gamma^{2L+1}}{\rho(E_i, J_i^{\pi_i}),}, \tag{3.1}$$

where $\rho(E_i, J_i^{\pi_i})$ is the average level density for states with J_i^π at energy E_i [Zan98]. The two key factors are the level density and the radiative strength function. The level density is considered first.

3.1 Level Density Models

3.1.1 Constant Temperature Function Model

Bethe initiated theoretical modeling of level densities with his landmark papers in 1936 and 1937 [Bet36, Bet37]. These papers were the basis for many later models. Bethe argued that since the level separation decreases very rapidly (approximately exponentially) with excitation energy, a statistical mechanics approach was appropriate. He considered two extreme models of nucleon interaction: the Fermi gas model and the liquid drop model. The Fermi gas model has been used very extensively in nuclear physics.

The Fermi gas model assumes that the interaction of nucleons is similar to the interaction of gas molecules: two nucleons are in close proximity for only a short time. Furthermore, since the nucleon kinetic energies are much smaller than the rest mass energies, nonrelativistic physics can be used. All possible energy levels available to the nucleons are assumed to be equally probable. The energy levels are assumed to be equally spaced near the Fermi level.

The level energy, U, was assumed to be related to the nuclear temperature, τ, by $U = a\tau^n$, where a is the "level density parameter". For the Fermi gas model n = 2, and the average level separation D is:

$$D(U) = 2\frac{U^3}{a}\sqrt{\pi}e^{-2\sqrt{aU}}. \tag{3.2}$$

The level spacing D is the inverse of the level density ρ. The angular momentum dependence of the spacing is usually expressed as

$$D(J) \sim \left[\frac{2\sigma^3}{2J+1}\right] e^{\left[\frac{(J+\frac{1}{2})^2}{2\sigma^2}\right]}, \tag{3.3}$$

where σ is the spin cutoff parameter. Combining these two expressions yields Bethe's general

level density formula, the Constant Temperature Formula, (CTF):

$$D(U,J) \sim \frac{U^3}{a}\sqrt{\pi}e^{-2\sqrt{aU}}\left[\frac{2\sigma^3}{2J+1}\right]e^{\left[\frac{(J+\frac{1}{2})^2}{2\sigma^2}\right]}. \tag{3.4}$$

This model described the level density data that was available at the time but does not include pairing and shell effects. Once these effects were established esperimentally, the CTF was modified appropriately.

3.1.2 Backshifted Fermi Gas Model

One of the early corrections to the CTF was by Newton [New56]. He modified the CTF to account for differences in the predicted and experimental level energies that were attributed to pairing. Newton redefined the ground state of Bethe's Fermi gas model to account for pairing effects. He assumed pairing correction functions that were subtracted from the actual excitation energy.

This subtraction effectively "back-shifted" the nuclear excitation energy, resulting in this modified CTF model being called the Back-shifted Fermi Gas (BSFG) model. Gilbert and Cameron [Gil65] expanded on Newton's model, devising a procedure to account for nuclear shell effects. The resulting expressions for a for spherical nuclei is:

$$a/A = 0.00917S + 0.142, \tag{3.5}$$

and for deformed nuclei is

$$a/A = 0.00917S + 0.120, \tag{3.6}$$

where S is the shell correction (see [Gil65] for details).

Numerous corrections have been made to this model to account for phenomena observed as the available data increased [Hui72, Ign75, Kat78]. However, the model remains

phenomenological. Physical understanding of the parameters is limited, and therefore extrapolation to new mass regions is questionable. An improved model is desired. For example, ideally one would like to know the level density of a nucleus far removed from the line of stability before performing radioactive beam experiments. One model that shows promise of answering this need uses the Shell-model Monte Carlo (SMMC) method.

3.1.3 Shell Model Monte Carlo Method

Past shell model calculations involving two-body correlations were limited in the size of the model space. Traditional diagonalization of the Hamiltonian quickly becomes impractical when applied to medium and heavy nuclei. The SMMC method circumvents this problem by using path integrals in a fluctuating auxillary field. Monte Carlo sampling techniques and numerical integration are then employed to solve for the level density [Lan93, Nak97].

The SMMC calculations accurately predicted level densities for ^{60}Ni, ^{68}Zn and ^{56}Fe [Nak98]. In order to demonstrate the advantages of the SMMC method over the phenomenological models, one would like to predict effects not considered in the earlier models. One such prediction is a parity asymmetry in the level densities for nuclei near ^{56}Fe. This prediction is important since the level density models used in current astrophysical calculations do not include such effects [Nak98]. If the prediction of parity asymmetry by the SMMC calculations could be verified for nuclei near the stability line, confidence in the use of this model for nuclei far from the line of stability would be enhanced. Thus there is a need for spectroscopic information on nuclei near ^{56}Fe that is sufficient to determine whether or not there is a parity dependence in the level density.

3.2 Radiative Strength Functions

The other factor that determines the average probability of γ-ray decay is the strength function, $f_{XL}(E_\gamma)$. The method tested in this dissertation and mentioned above re-

lies on the population of low-lying levels by sequential γ-ray decay from the resonance state. Knowledge about the radiative strength function is critical for predicting these relative populations and thus to application of this method. More generally the relative population of the low-lying levels can be used to test level density and strength function models. The rest of this section describes the standard radiative strength function models.

3.2.1 E1 Models

The average relative strength of E1 transitions compared with M1 transitions for A$\geq$100 is almost an order of magnitude greater: f_{E1} / f_{M1} = 7$\pm$1 [Zan98]. As a result most of the available data is for E1 transitions.

One of the earliest radiative strength function models for E1 transitions was the single particle model of Blatt and Weisskopf [Bla92]

$$f_{E1}^{SP} = C\,\frac{A^{2/3}}{D}, \tag{3.7}$$

where A is the atomic mass of the nucleus, D is the average spacing in the compound nucleus, and C is a constant.

As more data became available the single particle model could not explain the values of the total or partial widths for radiative decay [Axe62]. The breakdown was most pronounced in the energy region near the neutron or proton separation energies.

The model that superseded the single particle model was the Giant Dipole Resonance (GDR) model. In a simple hydrodynamic model the protons are considered as vibrating against the neutrons. The restoring force is the nuclear symmetry energy that acts to restore the excess neutron density [Dov72]. Brink [Bri55] hypothesized that formation of these Giant Dipole Resonances was independent of nuclear excitation energy. This implied that the radiative strength function depended only on the photon energy and that GDR resonances based on excited states should all be similar in size and shape. The Brink Hypothesis coupled with the GDR model fit the available data quite well. The strength

function was characterized by a photoabsorption peak whose centroid varies from about 22 MeV for ^{16}O to 13.5 MeV for ^{208}Pb. The GDR shape was Lorentzian [Kop90]

$$f_{E1}(E_\gamma) = \frac{1}{3\pi^2\hbar^2c^2}\frac{\sigma_0 E_\gamma \Gamma^2}{(E_\gamma^2 - E^2)^2 + E_\gamma^2\Gamma^2}, \tag{3.8}$$

where σ_0, Γ, and E are the empirical GDR parameters, and E_γ is the photon energy in MeV.

As additional data became available, there was evidence that the Brink Hypothesis also breaks down near and below the neutron binding energy. Axel [Axe62] proposed a strength function more suitable for the regions near separation energies; his proposed energy dependence was E^5. Equation (3.8) explains GDRs in spherical nuclei [Zan98] with the Axel proposal correcting for discrepencies between theoretical and experimental results.

For non-spherical nuclei something was needed to account for the observation that although the centroid and strength of the GDR changes monotonically with mass number A, the widths, Γ, do not. This effect was attributed to increased nuclear deformation resulting from higher temperature and spin. As the temperature is increased, surface vibrations begin to occur. These low frequency, large amplitude vibrations tend to broaden the width of the GDR. Further increases in energy bring the Coriolis and centrifugal forces into play, which further increase the total width [Hab99]. While the strength function still shows a GDR form, this spreading with increasing excitation energy led to modification of the spherical GDR formula (Equation (3.8)). This modified width [Dov72] is

$$\Gamma(E_\gamma, T) = \Gamma_G \frac{E_\gamma^2 + 4\pi^2T^2}{E_G^2}, \tag{3.9}$$

where Γ_G and E_G are giant resonance parameters derived from photoabsorption experiments [Kop90]. The modified temperature [Kad83] is expressed as

$$T = \sqrt{(E_x - E_\gamma - \triangle)/a}, \tag{3.10}$$

and includes the Fermi gas level density parameter a, the pairing energy $\triangle$, and the excitation energy E_x.

When these revisions are included, the GDR formula becomes

$$f_{E1}(E\gamma, T) = \frac{1}{3(\pi\hbar c)^2} \frac{\sigma_0 E_\gamma \Gamma_G \Gamma(E_\gamma, T)}{(E_\gamma^2 - E_G^2)^2 + E_\gamma^2 \Gamma(E_\gamma, T)^2}. \tag{3.11}$$

At lower energies, the strength function needed revision because this expression does not go to zero as $E_\gamma \rightarrow 0$. Treating the excited nucleus as a Fermi liquid with quasiparticle fragmentation, Kadmenskii, Markushev, and Furman (KMF) obtained a strength function for the "tail" region below the nuclear binding energy [Kad83]

$$f_{E1}(E_\gamma, T) = \frac{1}{3(\pi\hbar c)^2} 0.7 \frac{\sigma_0 E_G \Gamma_G \Gamma(E_\gamma, T)}{(E_\gamma^2 - E_G^2)^2}. \tag{3.12}$$

3.2.2 M1 Models

As noted at the beginning of this section, M1 transitions are weaker than E1 transitions (by a factor of about seven), and consequently are more difficult to measure. The available experimental data for M1 transitions are limited. The simplest model of M1 transitions is the single particle model

$$f_{M1}^{SP} = \frac{C'}{D}, \tag{3.13}$$

where a typical value for the constant C' is 6×10^{-9} MeV^{-3} [Gun95]. The other standard model uses a Lorentzian giant resonance formula. Typical parameter values [Boh75] for the Lorentzian are $\Gamma_G = 4$ MeV and $E = 41A^{-1/3}$ (MeV). σ_0 is usually adjusted to match experimental f_{E1}/f_{M1} values near the neutron binding energy.

3.2.3 E2 Models

The E2 admixture to the dominant E1 decay is believed to have an upper limit of 10% [Pos81]. The models used for the E2 strength function are the single particle and giant resonance models [Kop90]. The single particle model has the form

$$f_{E2}^{SP} = C'' \frac{A^{4/3}}{D}, \tag{3.14}$$

with experimental values for f_{E2}^{SP} found to be approximately 5×10^{-11} MeV^{-5} [Gun95]. The giant resonance formula for the E2 strength function is [Kop90]

$$f_{E2}(E_\gamma) = 5.22\times10^{-8} \frac{\sigma_0 E_\gamma^{-1} \Gamma^2}{(E_\gamma^2 - E^2)^2 + E_\gamma^2 \Gamma^2}, \tag{3.15}$$

where $E = 63A^{-1/3}$ MeV, $\Gamma = 6.11 - 0.012A$ MeV and $\sigma_0 = 1.5\times10^{-4}\mathrm{Z}^2\mathrm{A}^{-1/3}/\Gamma$ mb.

De-excitation through multipoles higher than E2 is rare and occurs for low energy transitions only if the spin difference is very large. In this experiment we shall only consider E1, M1, and E2 transitions.

Chapter 4

Low Level Population Method and DICEBOX Model

This chapter describes the Low Level Population (LLP) method for determining resonance spins and a model that simulates γ-ray cascades from nuclear resonances using Monte Carlo methods. As discussed in the introduction, there is a two-fold motivation for the experiments described in this thesis: one is to evaluate the applicability in the nuclear fp shell of the LLP method that has been successfully used for spin determination in heavy nuclei. The second and more general motivation was to provide detailed capture spectra to be used to evaluate radiative strength function and level density models. As discussed in chapter 3, a method that reliably and rapidly discriminates between (for example) $p_{1/2}$ and $p_{3/2}$ states for fp shell nuclei would be highly desirable; therefore we have tested the LLP method. To evaluate the various radiative strength function and level density models is a major and difficult effort. As a first step we utilize a relatively simple but successful Monte Carlo code (DICEBOX).

4.1 Low Level Population Method (LLP)

The link between the population of low-lying levels and the spin, J, of a resonance has long been known and attributed to the statistical properties of the radiative decay [Wet70]. Early experimental confirmations of the correlation of low level population with resonance spin were obtained in studies of isomeric decays in^{167}Er, ^{177}Hf, and ^{165}Ho [Hui60, Poe70], of s-wave neutron capture in ^{167}Er and ^{187,189}Os [Wet70], of s- and p-wave neutron capture in ^{238}U and ^{113}Cd [Gun97], and (most recently) of s- and p-wave neutron capture on ^{107,109}Ag and ^{117}In [Zan98].

This approach assumes that both resonance states and bound states above a certain level can be described statistically. This condition ensures many different possible γ-ray cascades from the resonance to the low-lying states. As discussed in Chapter 2, the dipole (E1 and M1) transitions will dominate. This fact coupled with the additional fact that the average multiplicity (number of steps from resonance to ground) is 3 or 4 [Mue50, Dra60], increases the probability for decay to low-lying levels with spins closer to that of the resonance.

The link between the resonance parity and the population of low-lying levels has not been studied extensively. The most recent study of the possible correlation between resonance parity and low level populations was undertaken at the GELINA facility [Zan98]. Correlations were observed between the parity of the resonance state and the γ-ray intensities for the low-lying levels. The parity dependence of the population of the low-lying levels was attributed to differences in the multiplicity. As discussed below, the DICEBOX model predicts a dependence of the population of the low-lying states on resonance spin and parity.

4.1.1 Resonance Identification using LLP

An illustration of the correlation between resonance spin values and low level populations is shown in Figure 4.1. Illustrated are three resonances with different spins. Below

each resonance is a region of densely spaced intermediate levels. The level density is sufficiently high that the decay probability involving these levels is statistical. Near the ground state lie two levels of different spin. If one assumes only E1 transitions, for the first resonance a multiplicity of at least four is required to populate the $J = 9/2$ level. On the other hand, the first resonance may populate the $J = 1/2$ level in one step. On the basis of these observations, it is reasonable to expect that this $J = 1/2$ level is more strongly populated than the $J = 9/2$ level. For the other two resonances, the $J = 9/2$ level is expected to be populated more as the resonance spin is increased. Thus the population of this 9/2 level will increase as the resonance spin increases. As a result the ratio of the intensity of the γ rays from the 9/2 level to the intensity of the γ rays from the 1/2 level should reflect the resonance J value. This is the basis of the low level population method.

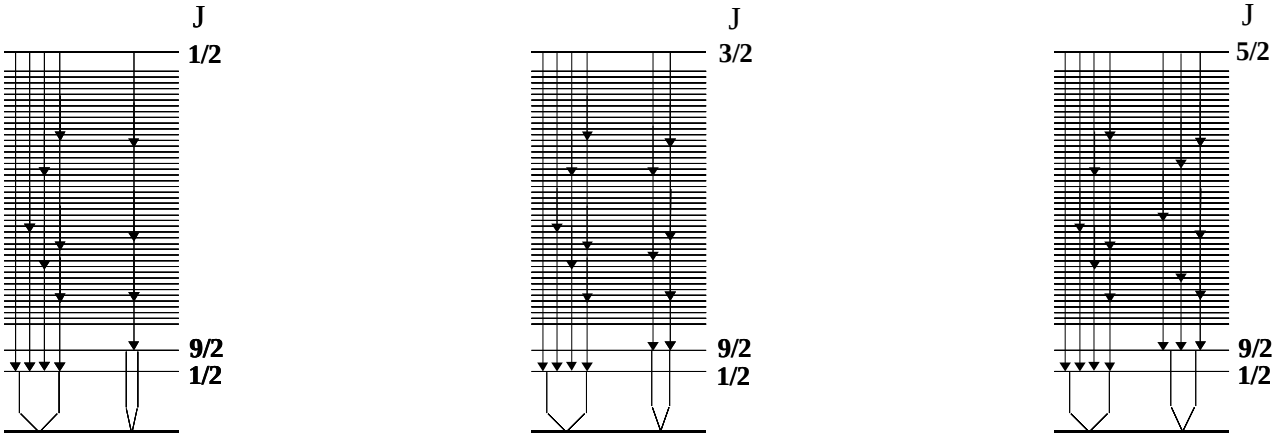

Figure 4.1: Population of low-lying levels for different resonance spin values. See text for details.

4.1.2 Experimental Support for the LLP Method

As mentioned previously, Zanini's results provide the most comprehensive experimental demonstration of the success of the low level population method to determine resonance spins and parities. As an illustration, consider his results for the ^{107}Ag(n,γ)^{108}Ag reaction. The ground state of ^{107}Ag has spin and parity $J^\pi = \frac{1}{2}^-$. Therefore, s-wave reso-

nances for this reaction can have $J^\pi = 0^-$ or 1^-. The p-wave resonances can have spin and parity $J^\pi = 0^+$, 1^+ or 2^+.

To evaluate the ratio, Zanini chose γ rays originating from two levels with widely differing spin values. The two γ rays have energies 300.1 keV (emitted from the 379.2 keV, 1^- level) and 329.2 keV (from the 485.1 keV, 4^- or 5^- level). The intensity ratio of these two γ rays for a number of resonances showed a clear separation between resonances of different J^π, as is evident in Figure 4.2 [Low99].

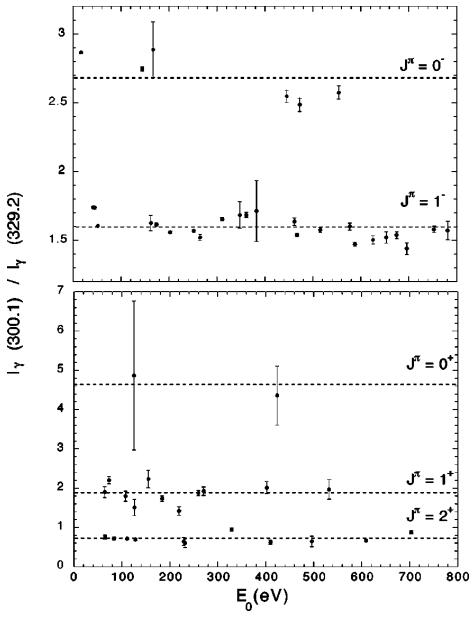

Figure 4.2: Example of low level population method for ^{108}Ag. This figure is reproduced from [Low99].

Although evaluating the applicability of the LLP method in fp shell nuclei is a primary motivation of this research, a more general issue concerns the level density and strength function models. One way to evaluate the models is to compare the observed population of states via radiative transitions with the model predictions. The computer code DICEBOX simulates the processes described here [Bec98].

4.2 DICEBOX Program

DICEBOX is a computer program that simulates γ-ray cascades using Monte-Carlo techniques. The resonance energy, spin, and parity are inputs; information on the low-lying states is also input to the program. DICEBOX simulates the population of lower levels for γ-ray decay from that resonance by assuming that γ-ray widths obey the Porter-Thomas distribution [Por56]. The goal is the comparison of the observed level populations with the predictions of radiative strength function and level density models. Since some of the transitions from the low-lying levels are obscured due to finite resolution, we consider only the relative population of 10 of the low-lying levels. The details are discussed in chapter 7. The parameters for these models can be adjusted in DICEBOX for each γ-ray cascade simulation. Options available include two different level density models, four different strength functions for E1 decay, and two different E2 and M1 radiative strength functions.

4.2.1 DICEBOX Model Assumptions

DICEBOX assumes that the resonance decay is purely statistical. There are also several additional assumptions:

- Below a certain energy, E_{crit}, the properties of all of the levels are known. This includes energies E, spins J, parities π, branching ratios I, multipole mixture coefficients δ, and the internal conversion coefficients α.
- Above this critical energy, the levels are treated as unknown and are randomly distributed according to one of the *a priori* level density formulae, $\rho(E, J)$, described below.
- Decay to the levels above E_{crit} is simulated with Monte Carlo techniques. The partial widths for the transition from level a to level b are

$$\Gamma_{ab} = \sum_{X,L} y^2_{X\,L}(E_a - E_b)^{2L+1} \frac{f_{XL}(E_\gamma)(E_a - E_b)}{\rho(E_a, J_a^{\pi_a})}, \tag{4.1}$$

where $y_{X\,L}$ is a randomly generated number drawn from a normal distribution with zero mean and unit variance. This parameter ensures a Porter-Thomas distribution for the partial widths.

- Partial widths from an initial level a to two different final levels b and c, Γ_{ab} and Γ_{ac} (where $b \neq c$) are statistically independent.
- All γ-ray cascades begin from a single resonance level with known energy E_1, spin J_1, and parity π_1.

4.2.2 Level Density Models Included in DICEBOX

The two DICEBOX level density models are the Constant Temperature Formula (CTF) [Gun95, Gil65]

$$\rho(E, J) = f_J \frac{1}{T} e^{(E-E_0)/T}, \tag{4.2}$$

and the Back Shifted Fermi Gas model (BSFG) [Gil65]

$$\rho(E, J) = f_J \frac{e^{2\sqrt{a}\sqrt{(E-E_1)}}}{12\sqrt{2}\sigma a^{\frac{1}{4}}(E - E_1)^{\frac{5}{4}}}. \tag{4.3}$$

Here T is the nuclear temperature, a is the "level density parameter", E is the level energy, E_0 and E_1 are energy backshifts, σ is the spin cutoff parameter, and

$$f_J = \frac{2J+1}{2\sigma^2} e^{\frac{-(J+\frac{1}{2})^2}{2\sigma^2}} \tag{4.4}$$

is the relative probability of a randomly chosen level having spin J. The values E_0, E_1, σ,

T, and a are input values [Gil65]. As explained in section 4.3, DICEBOX uses Monte Carlo techniques to simulate the energy levels between E_{crit} and the resonance energy level by discretizing one of the two level density functions, ρ(E,J). These level densities are discussed in chapter 3.

4.2.3 Photon Strength Function Models in DICEBOX

DICEBOX provides a choice of several models for the photon strength functions, $f_{XL}(E_\gamma)$ for E1, M1, and E2 transitions. Several of these models contain a Lorentzian resonance photoabsorption cross section parameter

$$\sigma_{\gamma\, abs}(E_\gamma; \sigma_0, E_0, \Gamma) \;=\; \frac{\sigma_0 E_\gamma^2 \Gamma^2}{(E_\gamma^2 - E_0^2)^2 + (E_\gamma \Gamma)^2}, \tag{4.5}$$

where E_γ is the γ-ray energy, and σ_0 is the maximum cross section with energy E_0 and damping width Γ.

E1 Strength Functions

DICEBOX provides four choices for the E1 photon strength function. The first option uses a single particle approximation and results in a constant strength function,

$$f_{E1}(E_\gamma) \;=\; \kappa_{E1}. \tag{4.6}$$

The second option uses the giant dipole resonance (GDR) model with two modes of vibrations: along the axis of symmetry ($i = 1$) and perpendicular to the axis of symmetry ($i = 2$).

$$f_{E1}(E_\gamma) \;=\; \frac{1}{3\pi^2\hbar^2c^2}\frac{1}{E_\gamma}\sum_{i=1}^{2}\sigma_{\gamma\, abs}(E_\gamma; \sigma_{0i}^{(E1)}, \Gamma_i^{(E1)}). \tag{4.7}$$

Option three uses a modified version of the GDR where the width is assumed to be energy and temperature dependent and the photoabsorption cross section, Eq. 4.5, is modified to

$$f_{E1}(E_\gamma, E_f) = \frac{1}{3\pi^2\hbar^2c^2}\frac{1}{E_\gamma}\sum_{i=1}^{2}\sigma_{\gamma\,abs}(E_\gamma, E_f; \sigma_{0i}^{(E1)}, E_{0i}^{(E1)}, \Gamma_i^{(E1)}), \tag{4.8}$$

where

$$\sigma_{\gamma\,abs}(E_\gamma, E_f; \sigma_0, E_0, \Gamma) = \frac{\sigma_0 E_\gamma^2 \Gamma\tilde{\Gamma}}{(E_\gamma^2 - E_0^2)^2 + (E_\gamma\tilde{\Gamma})^2} \tag{4.9}$$

and

$$\tilde{\Gamma} = \frac{E_\gamma^2 + 4\pi^2(E_f - \Delta)/a}{E_0^2}\Gamma. \tag{4.10}$$

Option four accounts for the behavior of the photon strength functions at lower γ-ray energies using the KMF model

$$f_{E1}(E_\gamma, E_f) = \frac{1}{3\pi^2\hbar^2c^2}\,F\sum_{i=1}^{2}\frac{\sigma_{0i}^{(E1)}, \Gamma_i^{(E1)}\tilde{\Gamma_i^{E1)}}E_{0i}^{(E1)}}{[E_\gamma^2 - (E_{0i}^{(E1)})^2]^2}, \tag{4.11}$$

where

$$F = (1 + 2f_1'/3)^{\frac{1}{3}}/(1 + 2f_1)^{\frac{1}{2}} \tag{4.12}$$

contains the Fermi liquid theory free parameters f_1 and f_1'. This model is described in detail in [Kad83]. In all cases the user inputs values for E_{0i}, σ_{0i}, Γ_i, F, Δ and κ_{E1}.

M1 Strength Functions

The two choices for the M1 strength function are a single particle model

$$f_{M1}(E_\gamma) = \kappa_{M1}, \tag{4.13}$$

and a giant magnetic resonance model

$$f_{M1}(E_\gamma) = \frac{1}{3\pi^2\hbar^2c^2}\frac{1}{E_\gamma}\sum_{i=1}^{2}\sigma_{\gamma\,abs}(E_\gamma;\sigma_{0i}^{(M1)},E_{0i}^{(M1)},\Gamma_i^{(M1)}). \tag{4.14}$$

Here the two different sets of parameters for $i = 1$ and 2 correspond to two different collective modes of motion, the spin-flip and scissors modes.

E2 Strength Functions

The electric quadrupole radiation strength function, $f_{E2}(E_\gamma)$, also has two options. The first one, the single particle option, utilizes a constant function

$$f_{E2}(E_\gamma) = \kappa_{E2}. \tag{4.15}$$

The second option, similar to the M1 strength function, permits two terms (labeled 1 and 2), corresponding to isoscalar and isovector collective quadrupole modes of motion, respectively:

$$f_{E2}(E_\gamma) = \frac{1}{5\pi^2\hbar^2c^2}\frac{1}{E_\gamma^3}\sum_{i=1}^{2}\sigma_{\gamma\,abs}(E_\gamma;\sigma_{0i}^{(E2)},E_{0i}^{(E2)},\Gamma_i^{(E2)}). \tag{4.16}$$

4.3 DICEBOX Simulation Procedure

Once the parameters for the level density, strength functions, the levels below E_{crit}, and the resonance have been specified, DICEBOX can begin simulation of a γ-ray cascade. A simulation consists of two basic steps:

1. Randomly generate a series of levels between E_{res} and E_{crit} that are representative of the specified level density.

2. Randomly generate a cascade starting at the resonance state and ending at the ground state that is representative both of the specified radiative strength functions and of the Porter-Thomas distribution.

DICEBOX first utilizes standard Monte Carlo techniques to generate a set of levels which (a) have excitation energies higher than E_{crit} but less than that of the resonance level and (b) are representative of both the specified level density and the requirement that such levels obey the Wigner spacing distribution [Wig57]. These generated levels are combined with the known levels below E_{crit} and the resonance level to yield a simulated level scheme that is consistent both with the known level parameters input to DICEBOX and with the desired level density. Each level in this level scheme is characterized by an energy E_a, a spin J_a, and a parity π_a, where a = 1,2...n. DICEBOX labels the resonance $a = 1$ and the ground state a = n. Each level is also assigned a random number generator seed α_a. This level scheme is called a *realization.* Note that infinitely many realizations are possible, only one of which corresponds to the true (unknown) level scheme.

Once a realization is established, the next step is to generate a cascade corresponding to that realization. DICEBOX starts with the resonance level and utilizes Eq. (4.1) and the generator seed for level 1 to generate γ-ray widths Γ_{1b} to each energy level b for which a transition is possible. DICEBOX calculates γ-ray branching ratios for each final state b and then uses a separate generator seed to determine which of the transitions will "occur" in this cascade. The final state of this particular transition is labeled B (note that there are many possible final states b, but only one actual state B in a given cascade simulation). What happens next depends on E_B. If B is the ground state, then the cascade is over. If $E_B < E_{crit}$, then the branching ratios out of state B are known, and the program randomly determines the next state C in the process using those experimental values. If $E_B > E_{crit}$, the program must randomly generate a set of branching ratios for B and determines the

next state C using these generated branching ratios. The procedure is repeated until the cascade reaches the ground state. Figure 4.3 [Bec98] illustrates this process schematically.

Because this is a Monte Carlo process, the procedure must be repeated many times to ensure that the average results correspond to processes which are more likely to occur. In its current form DICEBOX can create up to 999 different level realizations and up to 50,000 γ-ray cascades per realization.

4.4 DICEBOX — Comparison with Neutron Capture Experiments.

The user specifies how many realizations and how many cascades for each realization should be generated. After completing the γ-ray cascades for the prescribed number of realizations, DICEBOX writes the results to an output file. The output file contains a normalized population for all of the levels below E_{crit}. This population description is provided in two formats. In one format the population of the levels below E_{crit} includes contributions from both the levels above E_{crit} and those levels below E_{crit} that feed that level. The other output format lists the population of the levels below E_{crit} where the population does not include contributions from levels below E_{crit}. The user may also specify that DICEBOX list the average multiplicities for each realization for specific levels below E_{crit}.

Zanini used DICEBOX to simulate γ-ray cascades in the nuclides ^{108,110}Ag and ^{116}In to compare with his measurements. To choose between the possible model combinations and to minimize using unrealistic combinations, Zanini established some constraints. One constraint was the ratio of $f_{E1}/f_{M1} \approx 7$. This fixes the M1 strength function, which is less well understood than the E1 strength function. The maximum cross section parameter, σ_0, was also fixed at 0.8 mb. The total radiation width, Γ_γ, was set equal to the average experimental value of 140 meV. Ultimately this led to the testing of eight different model

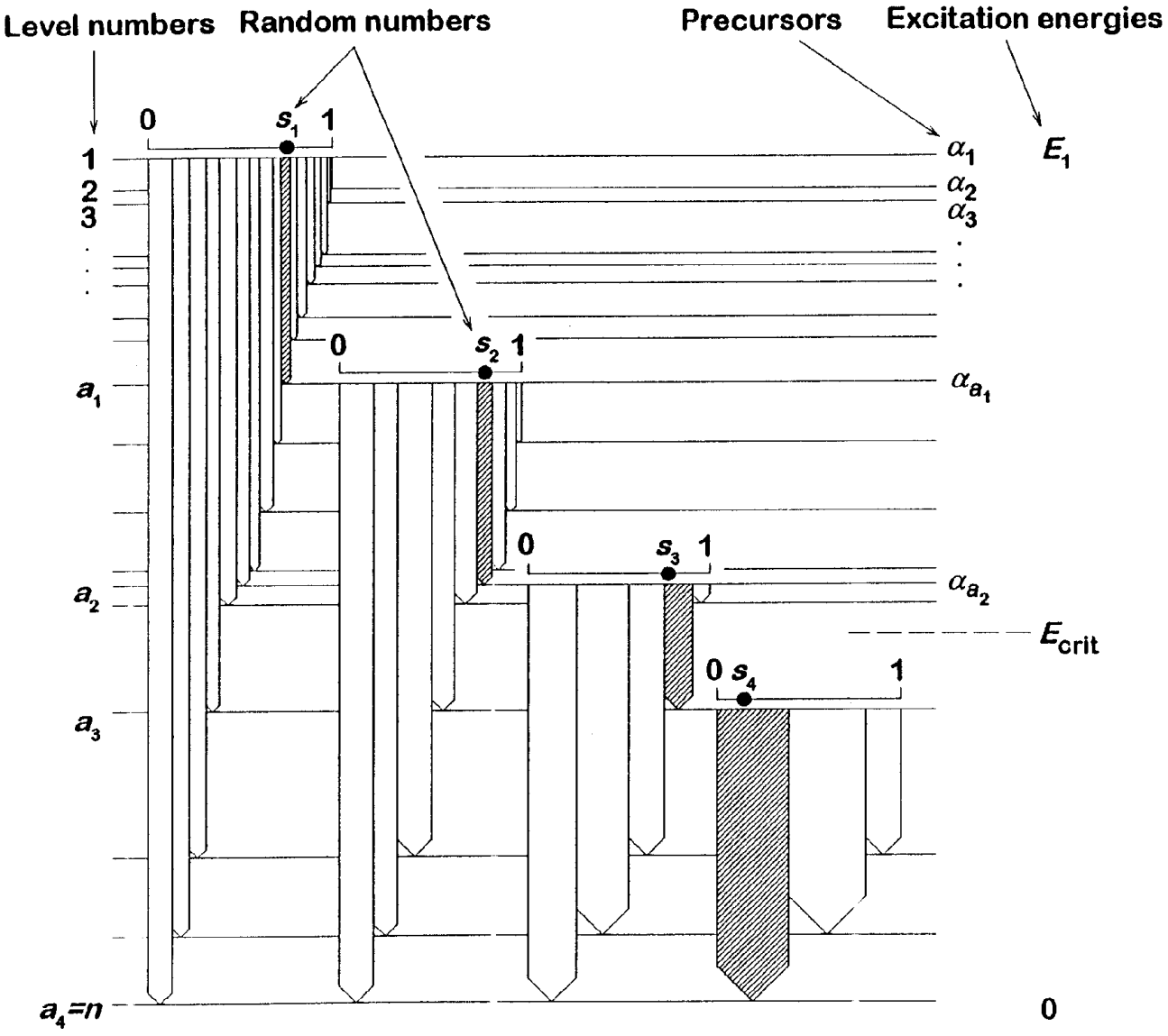

Figure 4.3: Schematic of DICEBOX simulation. This figure is reproduced from [Bec98].

Table 4.1: Models tested for ^{108,110}Ag.

Model	E1	M1	Level Density
a	Lorentzian	Lorentzian	CTF
b	KMF	Lorentzian	BSFG
c	KMF	SP	BSFG
d	KMF	f'_{M1}	BSFG
d'	KMF	f'_{M1}	BSFG
e	KMF	f''_{M1}	BSFG
e'	KMF	f''_{M1}	BSFG
f	KMF	f'''_{M1}	BSFG

combinations as listed in Table 4.1. Each model was tested for five different spin and parity combinations for the s- and p-wave resonances. The strength functions f'_{M1}, f''_{M1}, and f'''_{M1} refer to modifications of the M1 strength functions for enhancement by a factor K below a particular threshold energy E_{thr}, a dependence of the M1 strength function on the excitation energy, and an enhancement of the M1 strength function by adding a Lorentzian, respectively.

After comparing these model combinations with his experimental results, Zanini concluded that all of the models reproduced the low level population effect due to *spin.* However, the models differed on reproducing the low level population effect due to *parity.* Model a gave a parity effect opposite that of the experimental results. Model b showed no parity effect. An enhancement of the M1 strength function of 20% to 40% seemed to reproduce the parity dependence of the low level population. Model c was found to reproduce the experimental results most closely. Models d' and f also agreed with experiment. Zanini's success in reprducing his experimental results for ^{108,110}Ag with DICEBOX encouraged us to perform similar calculations for ^{49}V.

Chapter 5

Experimental Equipment and Procedure

The TUNL High Resolution Laboratory (HRL) can produce beams with very good energy resolution. This high resolution (200-300 eV) is accomplished by feedback systems that compensate for time dependent beam energy fluctuations. This chapter describes the experimental equipment and procedures utilized to obtain high-resolution data. Sections are devoted to the accelerator system, the magnet and analyzer control systems, the target chamber and detectors, the data acquisition system, and the targets themselves. Finally the procedures for locating resonances and measuring γ-ray spectra are outlined.

5.1 Accelerator and Homogenizer System

The accelerator is a belt-driven HVEC KN Van de Graaff accelerator modified to produce proton beams of energies up to 4.0 MeV. A schematic of the accelerator is shown in Figure 5.1. A detailed description of the accelerator and associated systems used to minimize beam energy fluctuations is given by Westerfeldt *et al.* [Wes88, Wes95]. Here only a brief overview of the system is presented.

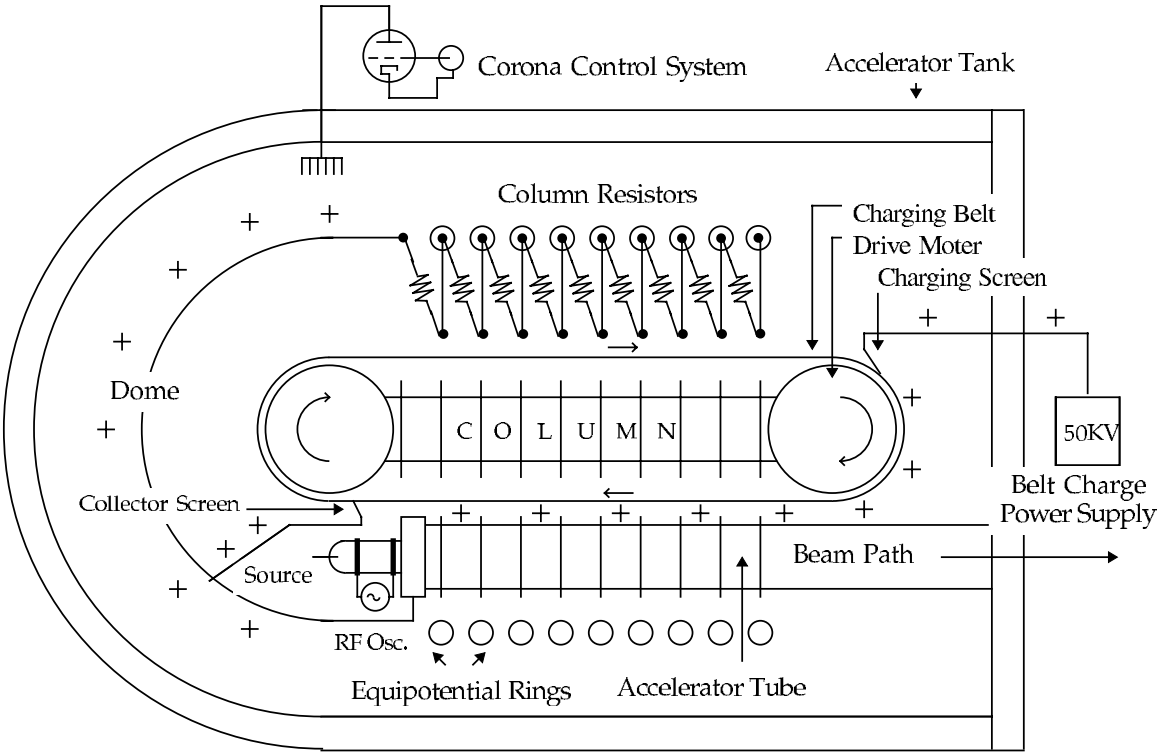

Figure 5.1: Schematic of the HRL single-ended Van de Graaff accelerator.

A diagram of the control and feedback systems is shown in Figure 5.2. The RF source produces a mixture of H_2^+ and H^+ ions. After extraction from the ion source, the ions are accelerated by a strong electric field. The accelerated ions are momentum-analyzed in the analyzing magnet: the H_2^+ ions are bent 17^o by the magnet and pass into the electrostatic analyzer, while the protons are bent 25^o and continue to the target chambers.

After passing through the analyzing magnet, the H_2^+ ion beam passes through horizontal slits (also called the "object" slits) and a slit difference signal is generated. This signal is fed back to the accelerator corona needles to reduce or increase current between the needles and the accelerator dome and thus adjust the beam energy appropriately. Because of the large time constant, due to the N_2-CO_2 buffer gas inside the accelerator, these feedback signals are rather slow. Thus the corona feedback system only provides corrections to energy fluctuations with frequencies $\leq$ 20 Hz.

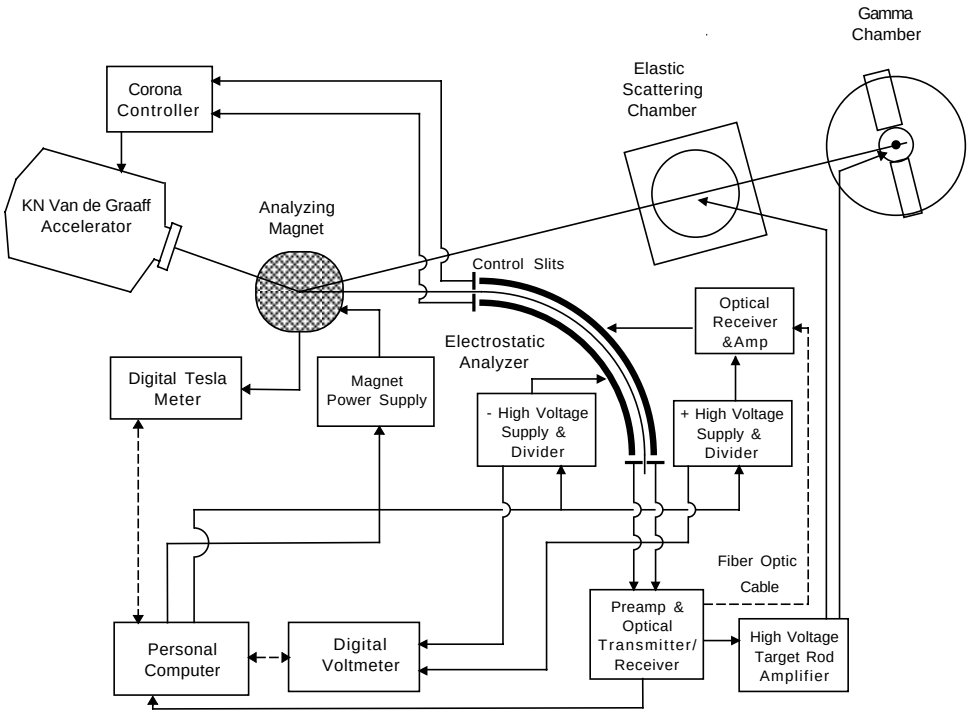

Figure 5.2: High resolution laboratory control loops. A current difference signal from the corona control slits is used to regulate the accelerator terminal potential, and a current difference signal from the image slits is used to regulate the magnetic field, the potential on the outer plate, and the target rod voltage.

A second signal also provides feedback via the corona needles. The AC capacitive pickup unit signal comes from a pair of plates mounted inside the accelerator tank that are alternately exposed to and shielded from the terminal voltage. This signal is DC coupled into the corona feedback system.

After passing through the corona slits, the H_2^+ beam enters the Electrostatic Analyzer (ESA), the key device in obtaining high beam energy resolution. The ESA consists of two parallel metal plates bent in a 90° arc of mean radius of curvature 1 meter; these plates are biased by a pair of high voltage power supplies to a voltage which is the desired beam energy in eV divided by 111.37. This factor is determined by the geometry of the plates and the mass of H_2^+.

At the end of the ESA is a set of "image" slits. When the beam has the proper energy

and the analyzing magnet is properly set, the beam will be centered as it passes through both the object and image slits. A slit difference signal is generated from the currents striking the two image slits; the magnitude of this signal is a measure of the deviation of the beam energy from the desired energy. A change in the slit difference signal corresponds to a change in the beam energy. The slit difference signal is used to generate three different feedback signals: one is sent to the outer plate of the analyzer to recenter the beam on the image slits, one is sent to the analyzing magnet to recenter the beam exiting the magnet, and the third – the homogenizer signal – is sent to the target rod to correct the beam energy. The use of these signals for the analyzer and the magnet is described in the next section.

5.2 Analyzing Magnet and Electrostatic Analyzer Controls

Both the analyzing magnet and electrostatic analyzer are actively controlled by a personal computer running National Instruments LabVIEW software. These two control systems are described in the following two subsections.

5.2.1 Analyzing Magnet Control System

The analyzing magnet field is used to steer the H_2^+ beam into the ESA. For good energy resolution, the magnetic field must be held relatively stable. The system for achieving this stability is shown in Figure 5.3. Two distinct modes of operation are utilized: "manual" mode in which the experimenter specifies the desired magnetic field directly and "slit" mode in which the field is adjusted to keep the analyzer beam centered on the image slits. In each case, the field is created by a current sent from a programmable power supply. The programming signal for this supply is the output of a 16-bit DAC which in turn has as its input a 16-bit output from the PC-DIO-24 interface of the PC. Control is via a PID process controller in LabVIEW. The major difference in the two modes is the input signal used for the PID process.

The manual mode is normally used for adjusting the system to a starting energy.

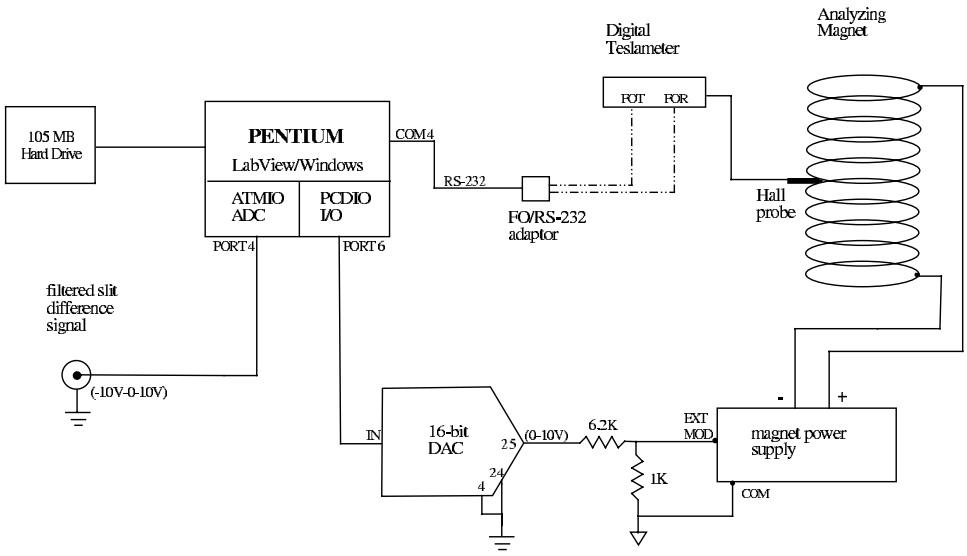

Figure 5.3: Analyzing magnet control loops.

The experimenter specifies the desired magnetic field. The PC reads the actual field via a serial interface to a digital Tesla meter and compares that reading to the desired setting. The PID controller adjusts the 16-bit output to maintain the desired field. The experimenter adjusts the field until the H_2^+ beam is passing through the electrostatic analyzer.

Once the H_2^+ beam is passing through the electrostatic analyzer, the experimenter switches the magnet control program to slit mode. In this mode of operation, the input to the PID controller is the slit difference signal generated from the currents on the image slits of the analyzer, and the controller adjusts the magnetic field such that the slit difference signal is close to zero. Not only does this mode maintain the magnetic field at the necessary value to keep the beam centered in the analyzer, it also allows the magnet to "track" changes in beam energy if they are not too large.

The proton beam is stepped to a new value E_p by setting the voltage on the ESA control plates to a value $E_p/111.37$ (see section 5.1). This change in voltage forces an imbalance of the beam on the ESA image slits. The LabVIEW program then changes the

magnetic field until the slit difference returns to zero, at which point the magnetic field corresponds to the new beam energy.

5.2.2 Electrostatic Analyzer (ESA) Control System

The ESA control system allows for precise control of the beam energy striking the target. Figure 5.4 shows a schematic of the control system for the electrostatic analyzer. The first step in the process is that the experimenter enters the desired energy to the MicroVax3200. This energy value is then sent via a serial line to the PC.

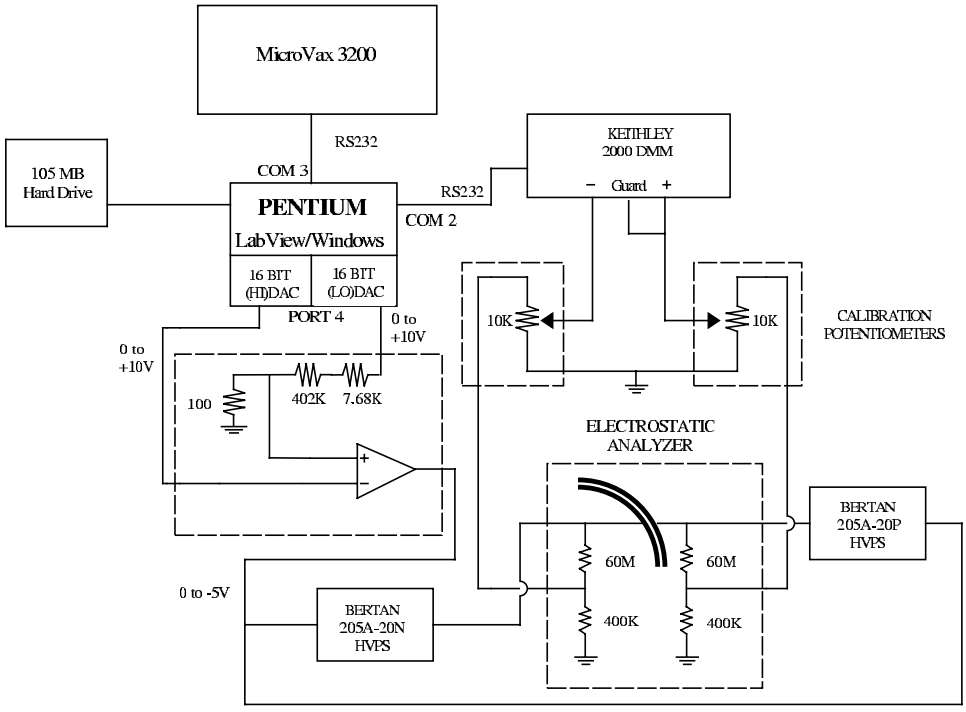

Figure 5.4: Electrostatatic analyzer control loops.

The LabVIEW program converts this energy to a 32-bit number, splits that into a pair of 16-bit numbers, and sends each of those numbers to a 16-bit Digital-to-Analog Converter (DAC) on the AT-MIO-16X board. Only the first 12 bits of the (HI)DAC are used due to the ± 4LSB resolution of the DACs. The low-order DAC signal is divided by

4096, and then the two DAC signals are summed to give 28-bit resolution. The summed signal is then converted to the 0 to -5 V range needed for the input signals for the two Bertan programmable power supplies. Applying the output of these power supplies to the analyzer plates sets the desired value for the beam energy. The voltage across the analyzer is measured by a 6–1/2 digit resolution, programmable Digital Multimeter (DMM) by utilizing the voltage signals from a pair of precision resistor stacks, one for each analyzer plate, that act as voltage dividers. The voltage division is such that there is direct correspondence of DMM readings and beam energy settings, (e.g., a DMM reading of 2.3 V corresponds to a beam energy of 2.3 MeV).

To ensure that the beam energy selected by the VAX corresponds to the measured beam energy (determined by the DMM signal), LabVIEW uses another PID controller. The PC reads the DMM every 400 ms and compares this value to the most recent value sent from the VAX. The PID controller adjusts the signal sent to the Bertan supplies to maintain the potential difference across the analyzer plates at the desired value. If the DMM reading corresponds to a beam energy more than 30 eV from the desired setting, data acquisition is inhibited until the actual potential difference returns closer to its desired value.

Extensive tests of the entire system in the past [Wes95] have measured beam energy resolution as low as 220 eV FWHM and typical energy drifts of 6 eV/hour.

5.3 Reaction Chamber and Detectors

The measurements described here were performed using a target chamber designed and installed by Drake [Dra94]. This chamber is intended to allow the experimenter to utilize both NaI(Tl) and Ge detectors for γ-ray detection and a silicon surface barrier detector for particle detection. The chamber is constructed with thin #304 stainless steel tubing of 0.065 inch thickness and an outer diameter of 3.5 inches. It is held at a baseline vacuum of approximately 6 μTorr with a small turbo pump attached to its bottom. In these measurements the target was aligned at 30° relative to the beam direction to allow each

detector a full view of the target.

Protons entering the target chamber either interact with the target or pass through it and are collected by the Faraday cup at the end of the chamber. The target rod floats at a 3000 V bias and fluctuates about that value in response to the homogenizer signal to correct for beam energy fluctuations measured in the analyzer. The Faraday cup has a suppressor voltage to minimize secondary electron emission.

The detectors used in these experiments were a combination of a single silicon surface barrier detector (SSB) for detection of charged particles, several NaI(Tl) detectors for detection of γ rays with higher efficiency but lower resolution, and a pair of high-purity germanium (HPGe) detectors for detection of γ rays with lower efficiency but higher resolution. One of the HPGe detectors is equipped with an anti-Compton shield composed of bismuth germanate (BGO). The combination of detectors used depended on the specific measurements being performed. Excitation functions of the ^{48}Ti(p,γ) reaction were measured in order to locate and identify resonances. γ-ray spectra were measured to determine the decay of particular resonances. Subsections 5.3.1 and 5.3.2 outline the detector arrangements for these two different experiments.

5.3.1 Excitation Functions

Excitation functions were measured using four NaI(Tl) detectors, one HPGe detector, and one SSB detector, as shown in Figure 5.5. Four NaI detectors were located at 55°, 55°, 125°, and 135° to detect γ rays from the (p,γ) and (p,$p_1\gamma$) reactions. These detectors subtended solid angles of about 0.800 sr. The detectors were 7.62 cm $\times$ 7.62 cm NaI(Tl) crystals crystals. Each of the detectors was shielded with lead, either as lead brick or as bagged lead shot, to reduce background from γ rays entering the crystals from the side or back. This shielding is only shown for two detectors in Figure 5.5. A silicon surface barrier (SSB) detector was also located in the chamber at 165° and subtended a solid angle of 2.21 msr. Space limitations allowed only one of the HPGe detectors (the unsuppressed detector)

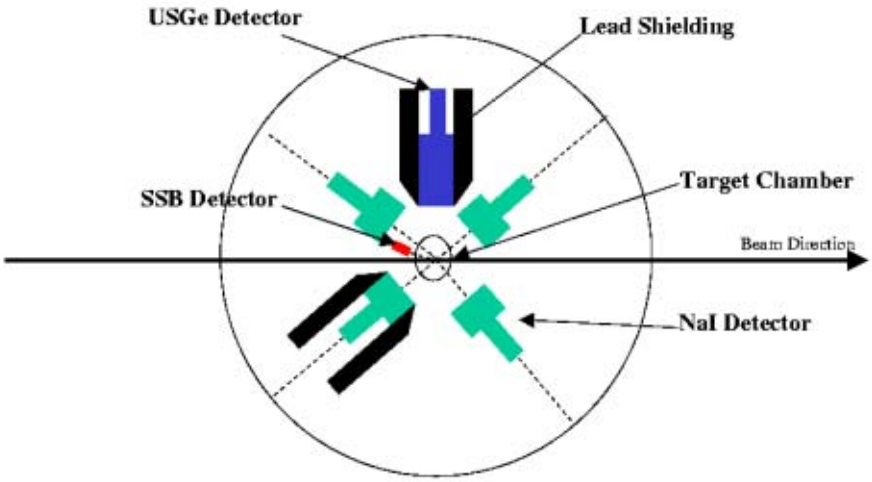

Figure 5.5: Detector arrangement for excitation function measurements.

to be used during excitation function measurements.

5.3.2 γ-ray Spectra

The γ-ray spectra measurements utilized both HPGe detectors along with the SSB detector and a single NaI(Tl) detector. The SSB and NaI(Tl) detectors were used to generate short excitation functions in order to locate the resonances of interest. The HPGe detectors are used to detect the γ rays from each resonance. A diagram showing an arrangement of the two HPGe detectors is shown in Figure 5.6. In our measurements, the BGO-suppressed detector was actually at 55° rather than the 125° illustrated. The unsuppressed HPGe detector was at 90°. A single NaI(Tl) detector, located at 135°, was also utilized in these measurements to aid in locating and identifying resonances.

The two 60% efficient HPGe detectors and the anti-coincidence BGO detector are the heart of the γ-ray detection system. The HPGe detectors have measured energy resolutions of approximately 2.0 keV at 1333 keV. This resolution is much better than the 100-keV resolution for the NaI detectors. One of the HPGe detectors is located at 90° to eliminate Doppler shifts of the γ ray energies; the other is at 55° to minimize angular distribution

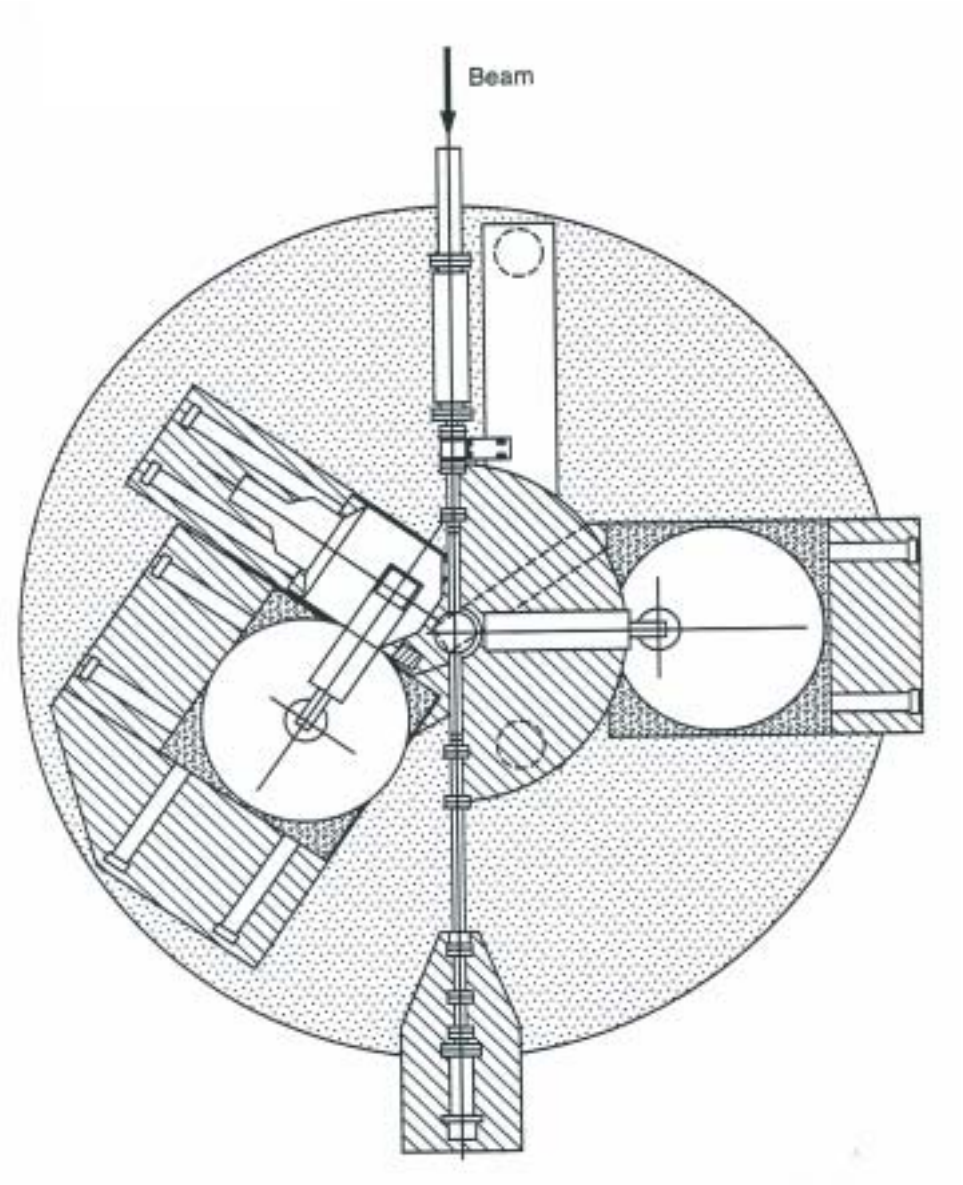

Figure 5.6: Positioning of HPGe detectors and BGO shield. In our measurements, the BGO-suppressed HPGe detector was located at 55° rather than the 125° shown in the illustration.

effects. Both of the Ge detectors are attached to liquid nitrogen dewars which maintain the detector temperatures at 77 K. The BGO detector, as illustrated in Figure 5.7, surrounds one of the HPGe detectors and is used to veto signals from γ rays that deposit only a fraction of their energy in the HPGe detector and are also detected in the BGO.

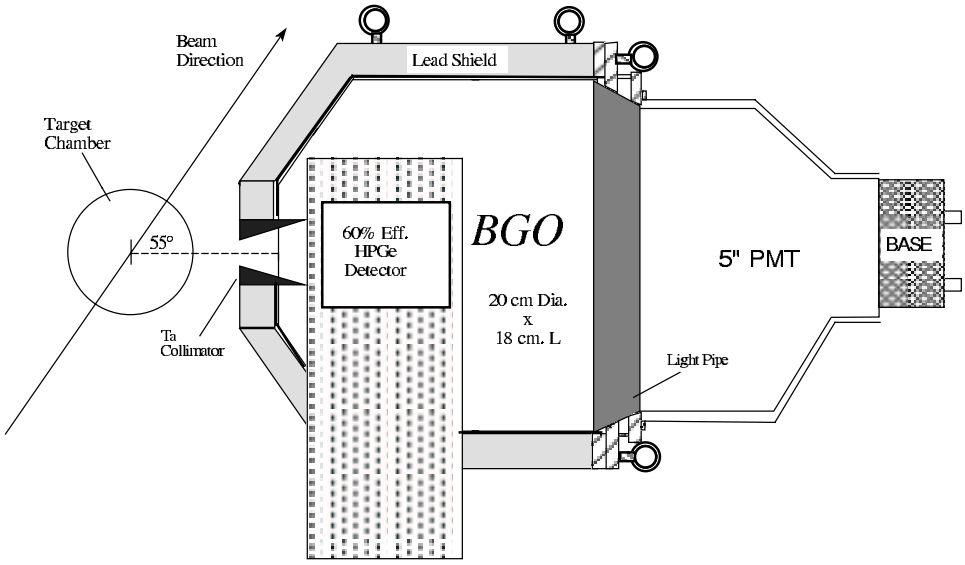

Figure 5.7: Schematic of the BGO detector used for Compton suppression of the HPGe detector.

This veto process reduces escape peaks and background from Compton scattering within the HPGe detector. The actual suppression of the Compton scattering and escape peak events occurs in the data acquisition hardware (see section 5.5) by producing a veto for data events that occur simultaneously in the BGO and the HPGe detectors. The $Bi_4Ge_3O_{12}$ material was chosen since it has the highest photon detection efficiency of any commercial scintillator [Kno89]. The BGO detector is shaped such that the majority of the detector volume is in the direction of the peak of Compton scattering. The 55° taper on the front edge of the BGO allows the detector to be positioned at angles in the range 55° to 125°.

5.4 Targets

The experiments described in this thesis used thin-film ^{48}Ti targets. They were produced though high current evaporation using the setup illustrated in Figure 5.8. The targets were prepared according to the following procedure. First 7.0 mg of high purity TiO_2 (99.81% ^{48}Ti) was measured and deposited in an open molybdenum boat coated with a layer of aluminum oxide. The boat was installed in a bell jar and connected to a pair of high-current electrodes. The bell jar was evacuated to about 4 μTorr and then flushed three times with research-grade hydrogen.

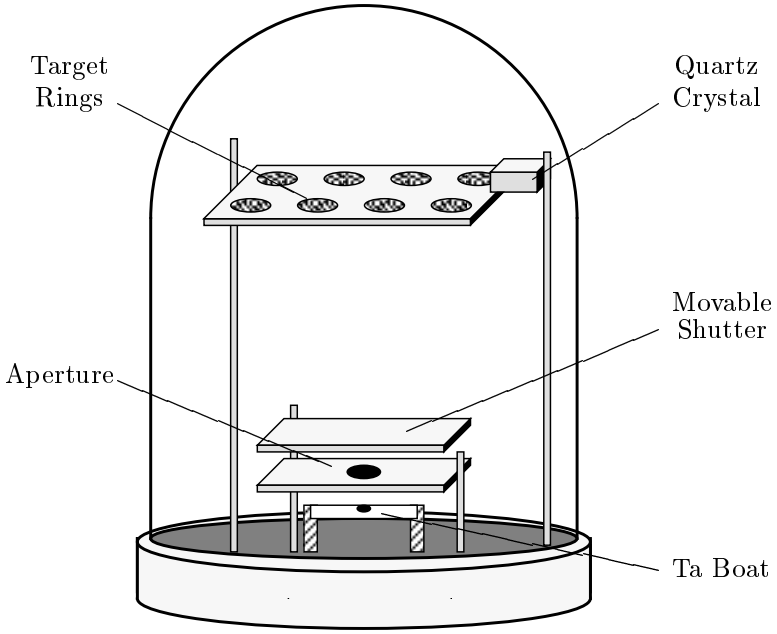

Figure 5.8: Thin film target fabrication system.

The jar was then filled with 5 inches Hg of research-grade hydrogen, and a current of about 160 A was sent through the boat for 10 minutes to ensure total reduction of the titanium. When the boat's contents were jet black in color (after turning off the current), indicating total reduction, the bell jar was let up to air, and the titanium was transferred to an open tantalum boat. The tantalum boat was installed in the bell jar. Target rings

with 5-μg/cm^2 carbon foils mounted on them were placed on a rack ≈22 cm above the boat; the side of the target rings on which the carbon foil was mounted faced downward. Clean microscope slides were placed on the target rack, covering the non-carbon foil side of the targets, to prevent ^{48}Ti from being deposited on that side. The system was evacuated to 2 μTorr; cold traps were also employed. A current of 170 A was passed through the tantalum boat causing the ^{48}Ti to evaporate onto the targets. The thickness was monitored by an acoustic quartz crystal Maxtek Thickness Monitor. Experience showed that for 7 mg of TiO_2, a current of 170 A applied for 2 minutes and 20 seconds produced a target of about 1.4 μg/cm^3 thickness. This thickness corresponded to a proton energy loss in the target of about 100 eV, much smaller than the 200-300 eV overall resolution of the system.

5.5 Data Acquisition

The HRL data acquisition system was used both to locate resonances by measuring excitation functions and to measure γ-ray spectra from the decay of those resonances. Section 5.5.1 describes the data acquisition configuration used to measure excitation functions. Section 5.5.2 describes the data acquisition configuration used to study capture spectra.

5.5.1 Excitation Functions

SSB and NaI(Tl) detectors were used to collect data for the excitation functions. The electronics used to generate the yield curves are shown in Figure 5.9.

The signal from the detector is sent to a preamplifier, where the signal is shaped, amplified, and then sent to a linear amplifier. The amplifier generates two signals, one unipolar and one bipolar, each of which has an amplitude proportional to the energy deposited in the detector. The amplifier delays the unipolar signal by 2 μs relative to the bipolar signal. To ensure that the unipolar and bipolar pulses will arrive at the Multiplexer/ADC simultaneously (after the timing signal is processed through the acquisition electronics), the unipolar pulse is then sent over a 900 ns delay line.

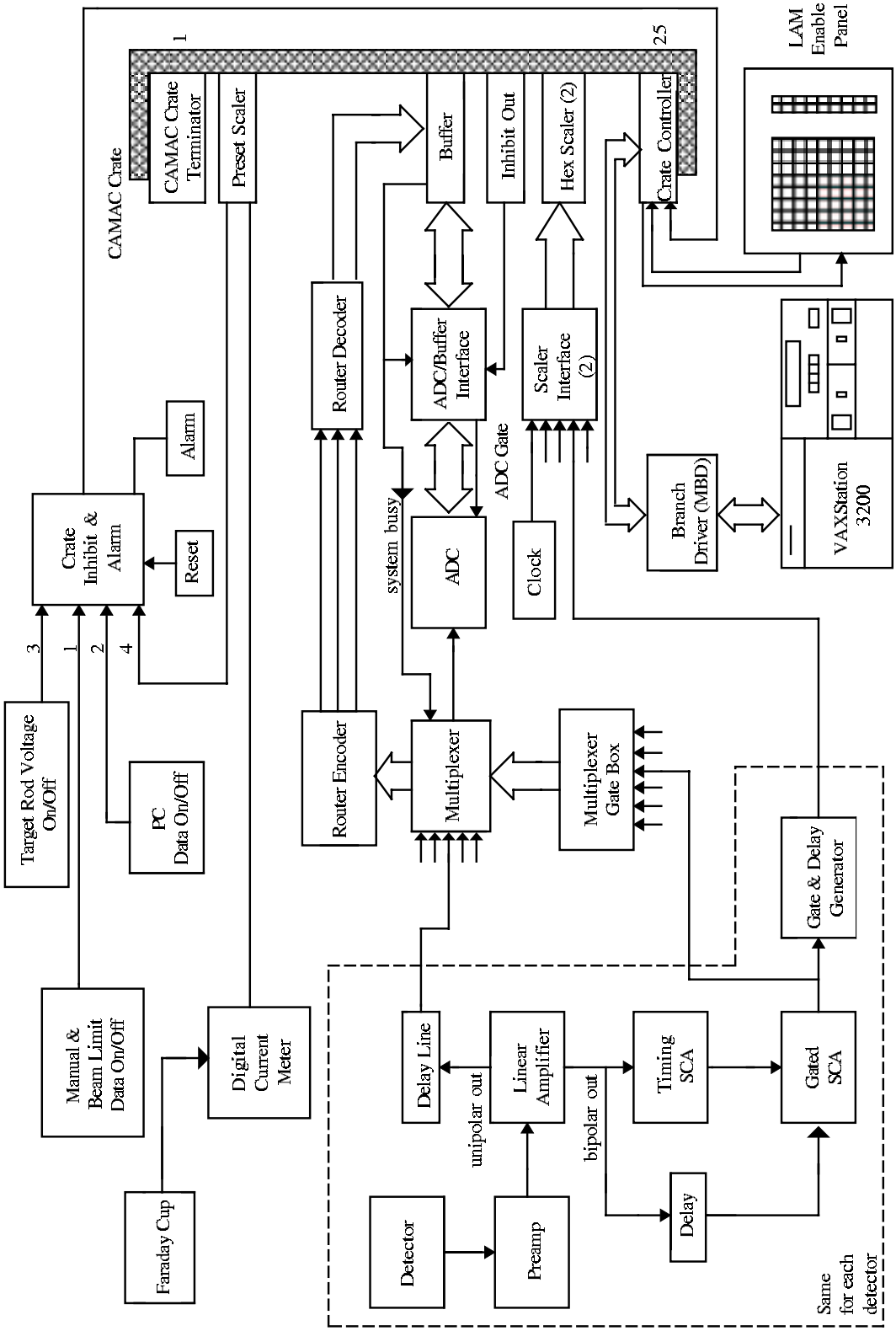

Figure 5.9: Electronics for silicon surface barrier and NaI(Tl) detectors.

The bipolar pulse is used to gate out the carbon pulses. Elimination of the carbon pulses reduces deadtime and prevents the electronics from being overloaded by the many carbon signals. (The carbon foil backings are typically five times thicker than the target.) To gate out the carbon counts, the bipolar signal is split after leaving the linear amplifier; one part enters a timing single channel analyzer, TSCA, and the other is delayed 2 μs and then sent to a gated Single Channel Analyzer, SCA. At the TSCA an energy window is set to bracket the carbon energy peak. This window is set only for the SSB detector, since the carbon peak only occurs in the charged particle spectrum. For the NaI detectors, the window width is set to zero. Following the TSCA, the signal enters the SCA in coincidence with the other delayed, bipolar signal. If there is a signal from the TSCA, meaning that the event has the same energy as elastic scattering from carbon, the delayed bipolar signal is vetoed (because the signal corresponded to an unwanted carbon event). The SCA further discriminates the signals: upper– and lower–level discriminators are set to remove low–amplitude background and high-amplitude pileup, respectively. Thus the SCA produces an output only for signals which lie between the minimum and maximum energy settings and do not correspond to a carbon signal.

The output of the SCA is sent to both a Gate and Delay generator and a Multiplexer Gate module. The Multiplexer Gate module determines which detector has fired, and codes that into a gate signal for the Multiplexer. The timing between the signals is such that the Multiplexer Gate signal arrives at the Multiplexer prior to the corresponding unipolar signal. The gate signal admits that unipolar signal into the Multiplexer and starts the process of digitization by a Northern ADC. A series of handshake connections result in the digitized signal being stored in a CAMAC buffer module as part of a word that also indicates in which detector the signal originated. The ADC output and its associated routing signal are then stored in one of two 256 word blocks within a CAMAC buffer module. When one block becomes full, the buffer signals the Microprogrammable Branch Driver (MBD) (the interface between the VAX computer and the acquisition electronics) to transfer the

buffer's contents to the VAX. Meanwhile, the other buffer collects the incoming events. The VAX then sorts the data into the appropriate data areas using the XSYS data acquisition software [Sod87]. XSYS allows the collected data for each of the spectra to be displayed via the DISP graphics function. For the SSB and NaI(TL) detectors the spectra are displayed in 512-channel spectra. The data from the unsuppressed HPGe detector is stored as an 8192-channel spectrum.

Hardware scalers are used to determine the deadtime and to control data collection intervals. The output of each gate and delay generator module is counted by a CAMAC scaler. Deadtimes for the various detectors are calculated by comparing this scaler value with the ADC events for that detector. Finally, a digital current integrator integrates the beam collected in the Faraday cup by producing pulses that correspond to the amount of charge collected. These outputs pulses are sent to a Borer 1008 scaler and decrement it from a preset value until zero is reached. When the preset scalar reaches zero, further data collection is inhibited. The system clears all buffers, writes the data to disk, adjust various experimental values (e.g., the beam energy), generates the next point on the excitation function, clears the data, and restarts data collection.

5.5.2 Capture Spectra

The electronics used in processing γ-ray data from the HPGe detectors is shown in Figure 5.10. Processing these γ-ray signals is more complicated than for the excitation functions because both a timing and an energy signal are generated from the HPGe detector preamplifiers.

The energy signal generated by each preamplifier can be affected by pileup rejection (PUR) or by ballistic deficit (BDC). Pileup occurs when two events occur close enough in time in the detector that their pulses are shaped into a single charge pulse; the amplifiers that we use detect pulse pileup and reject those signals so that no further processing occurs. Ballistic deficit occurs when an incomplete charge collection occurs within the shaping time

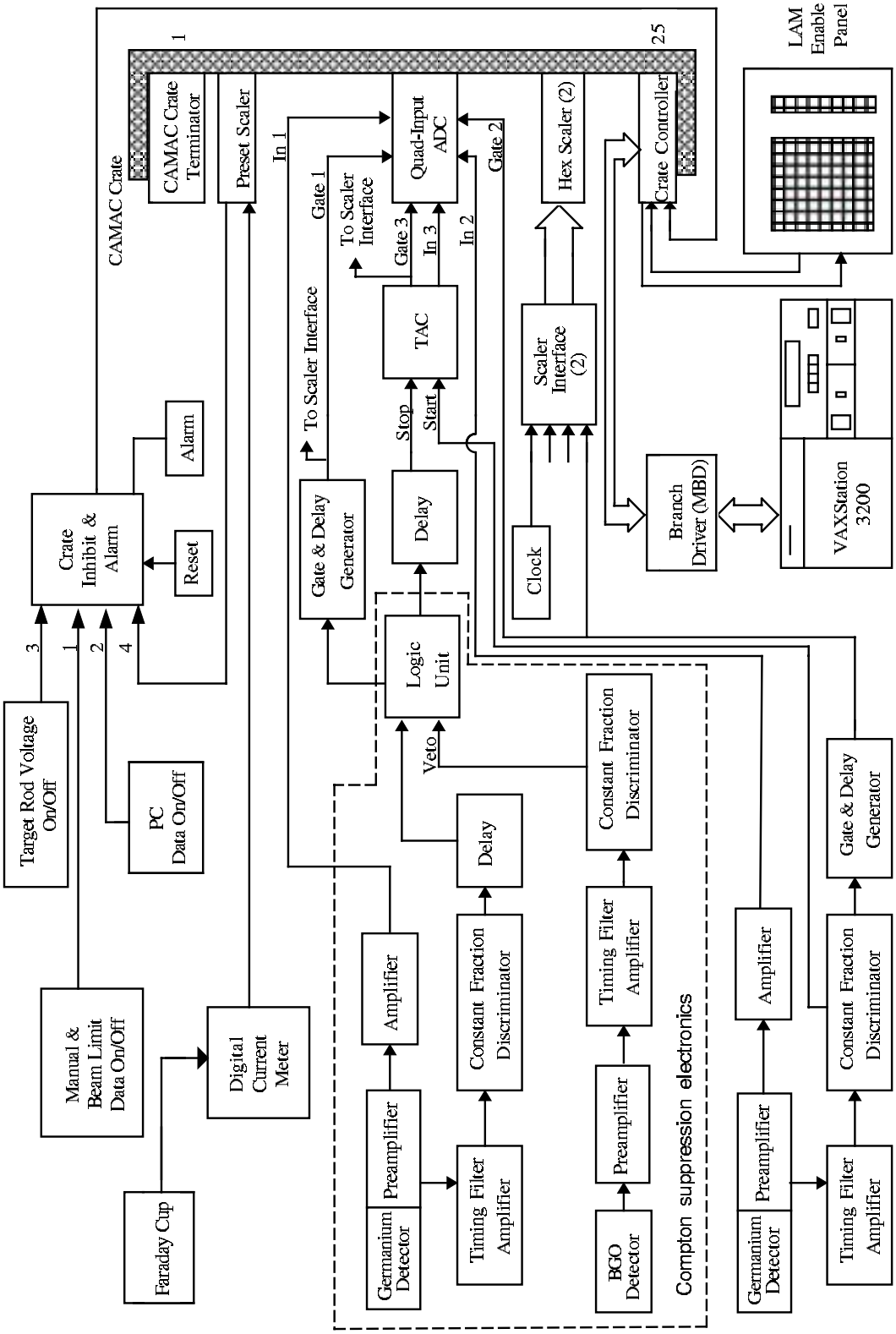

Figure 5.10: Electronics for the HPGe detectors.

of the amplifier; the resulting depressed amplitudes of these signals degrade the overall energy resolution for the detector. The energy signal from the HPGe preamplifier enters a spectroscopy amplifer where the pulse is shaped and integrated. The amplifiers we use automatically correct the signal for ballistic deficit and reject signals in which pileup is evident. The output of the amplifer is sent to a 4-channel ADC.

The timing signals from the BGO and the suppressed HPGe detector are used to reject signals arising from Compton scattering and pair production. First the timing signals from both detectors are sent to a Timing Filter Amplifier (TFA) which amplifies and shapes the signals. These signals are then sent to a Constant Fraction Descriminator (CFD) which produces a signal better suited for analyzing the relative timing between two signals. The CFD accomplishes this by producing a pulse a fixed time after the leading edge has attained a certain fraction of its total amplitude. The CFD's produce a 500-ns signal for the BGO and a 50-ns signal for the suppressed HPGe detector. Both signals are sent to a Logic Unit with the suppressed HPGe detector signal delayed by 127 ns. Any signal from the HPGe detector which is accompanied by a signal from the BGO detector is vetoed by this logic unit, since that signal correponds to a photon whose full energy was not deposited in the HPGe detector.

The non-coincident "good" CSGe signals are sent to a Gate and Delay (G&D) module which generates a gate for a CAMAC quad ADC to process the corresponding energy signal. The unsuppressed Germanium (USGe) signals are sent via a parallel data acquisition path, except that the CFD signals are sent directly to the G&D module. The outputs from the G&D modules are also sent to a CAMAC scaler where the counts are used in correcting for deadtime, as explained in section 5.5. The ADC digitizes the input and transfers its output to the MBD via the CAMAC crate controller. The MBD in turn transfers the digitized signal to the VAX, where it is stored in an 8192-channel spectrum.

5.6 Experimental Procedure

5.6.1 Excitation Functions

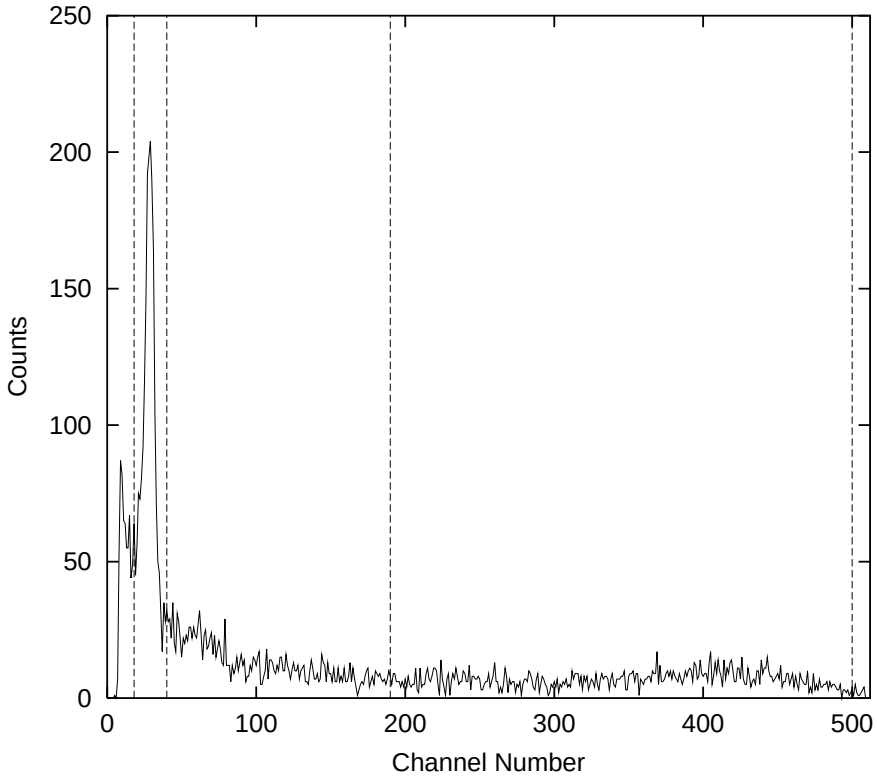

Figure 5.11: NaI spectrum at $E_p = 2.1930$ MeV. Dashed lines indicate gates set about the 0.9834-MeV peak and the $2.6 - 9.0$ MeV region.

An excitation function was measured to evaluate resonances for possible detailed study of the capture process with HPGe detectors.. The excitation function was measured over the energy range 1.97 - 2.80 MeV in 100-eV steps. This region has many well isolated $1/2^+$, $1/2^-$ and $3/2^-$ resonances.

For the NaI spectra one gate was set very wide in energy, with the lower limit set just above the background Pb line at 2.615 MeV and the higher limit was set at the limit of the spectrum, around $E_\gamma = 9.50$ MeV. The counts collected from this gate were used to

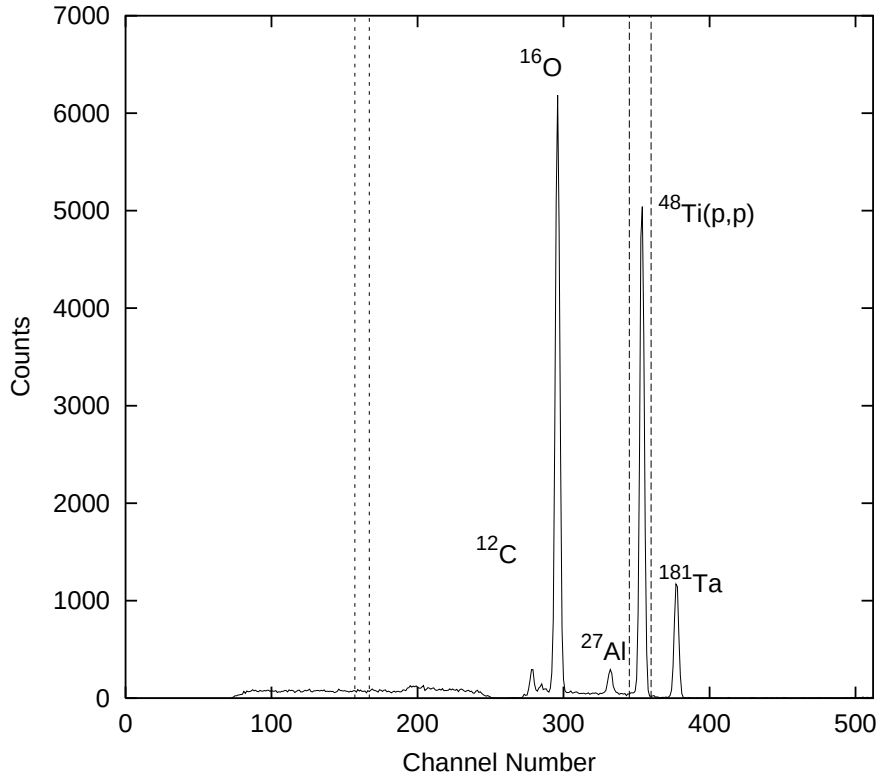

Figure 5.12: Particle spectrum at $E_p = 2.1930$ MeV. The dashed lines indicate the gates set about the ^{48}Ti eleastic and inelastic peaks.

generate yield curves for the (p,γ) reaction. The second gate was set around the $2^+ \rightarrow 0^+$ γ-ray in ^{48}Ti that follows inelastic scattering to the first excited state. The counts in this gate were used to generate a $(p,p_1\gamma)$ yield curve with the NaI detectors. An example for these gate settings is illustrated in Figure 5.11. Calibration of the NaI spectra was accomplished with a ^{60}Co source followed by an extended run to determine the background from ^{40}K and ^{208}Pb.

The SSB detector also had two gates set in its spectra (see Figure 5.12). The first gate bracketed the peak corresponding to elastic scattering from titanium; these counts were used to produce the elastic yield curve. The second SSB gate was set around the peak corresponding to inelastic scattering to the first excited state in ^{48}Ti. These counts were

used to produce the inelastic yield curve. Both gates were adjusted for kinematic energy shifts as the incident energy changed.

Typical excitation functions for the $p + {}^{48}$Ti elastic, inelastic and capture reactions are shown in Figure 5.13. Plots for the entire energy range studied are shown in Appendix E.

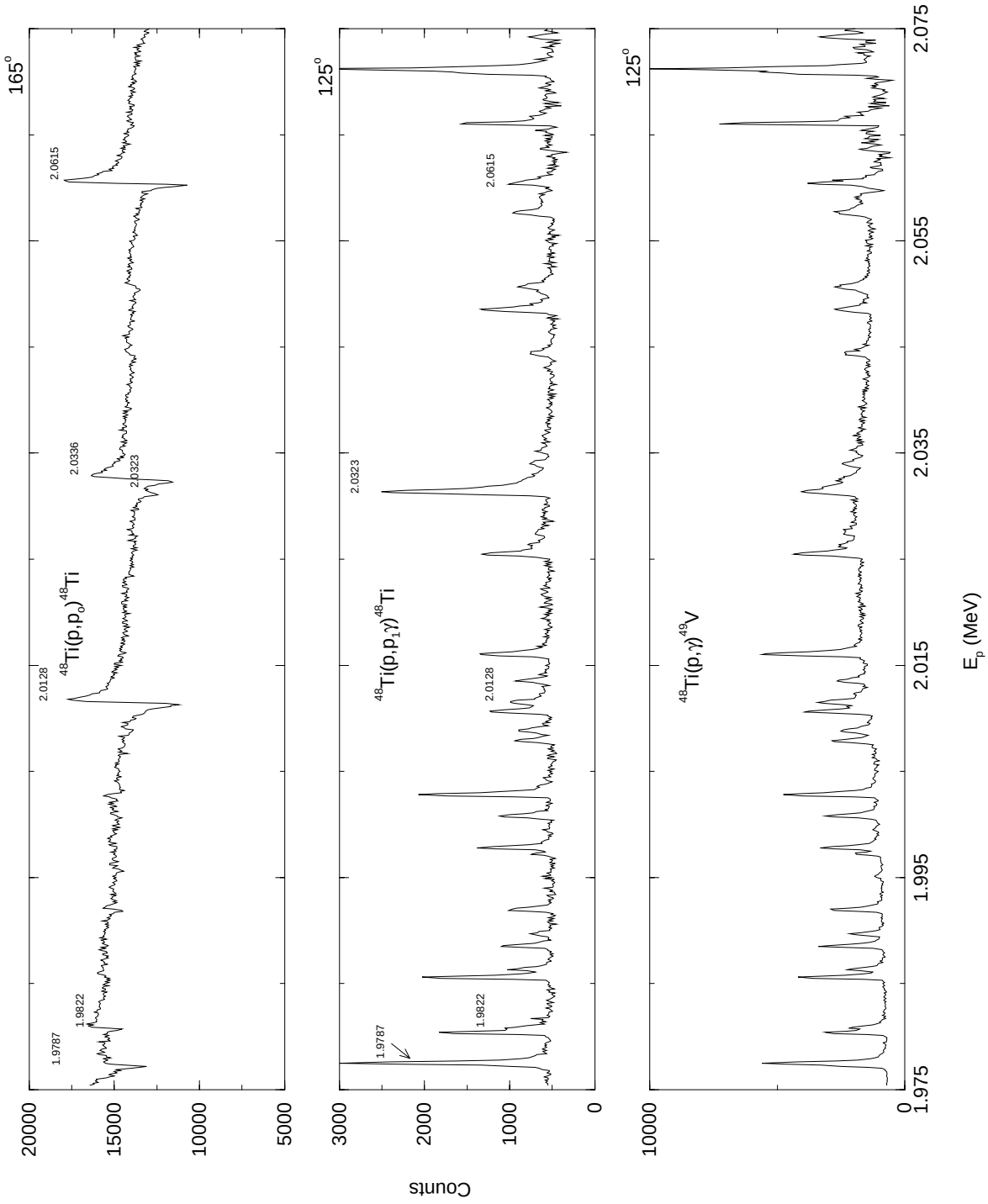

Figure 5.13: Elastic, inelastic, and capture yield curves for protons on ^{48}Ti in the energy region E_p = 1.975 to 2.075 MeV.

5.6.2 Capture γ-ray Spectra

There were three steps in acquiring γ-ray spectra from the resonances of interest: calibration of the spectra, identification of the resonance, and data collection. Prior to calibrating the spectra, a ^{60}Co source was used to gain match the two HPGe detectors and to ensure that the spectra would include ^{49}V transitions from 152 keV to 9.1 MeV. This ^{60}Co spectrum, used together with a 6 hour room background measurement, also provided a first–order energy calibration that was useful in locating the ^{152}Eu γ rays in the subsequent calibration.

To achieve an accurate energy calibration spanning the energies of interest, two calibration standards were used: one was a ^{152}Eu source and the other was the well-studied E_p = 991.86 keV resonance in the ^{27}Al(p,γ) reaction [End90]. The ^{152}Eu source provides several well known γ rays ranging in energy from 121 to 1408 keV [Fir96]. These are useful for calibrating the lower energy portion of the spectrum. The ^{27}Al(p,γ) reaction provides γ rays ranging in energy from 1522 keV to 10762 keV, useful for calibrating the higher energy portion of the spectrum.

The energy calibration was obtained with the unsupressed and Compton–suppressed detectors located at 90° to minimize Doppler shifts in the γ-ray energies. Sufficient statistics for the energy calibration were obtained in about 2.5 hours each for the ^{60}Co and ^{152}Eu sources and about 30,000 μC of integrated beam current (BCI) collected in the Faraday cup for the ^{27}Al resonance.

An efficiency calibration was also required since the HPGe detector efficiency is strongly energy dependent. Although the efficiency was not used during on-line data collection, it is crucial for the off-line analysis. The same geometric configuration used for the ^{49}V data (the USGe detector at 90°, CSGe detector at 55°, and the target rod at 30°) was chosen to ensure an accurate calibration. Again both a ^{152}Eu source and γ rays from the 992-keV resonance in ^{27}Al(p,γ) were used. For the Eu data the source was attached to a target ring on the target rod holder to mimic the configuration used for the Al and Ti

targets. Sufficient counts for the efficiency measurement were obtained in 2.5 hours for the ^{60}Co and ^{152}Eu sources and 100,000 μC BCI for the ^{27}Al resonance.

Two typical ^{49}V γ-ray spectra from the CSGe and USGe detectors are shown in Figures 5.14 and 5.15. The improved signal-to-noise ratio of the CSGe detector compared with the USGe detector (due to the Compton suppression) is readily apparent. A typical data run consisted of collecting data first on and then off resonance for 30,000 μC BCI, with a typical cummulative total charge collected on and off resonance of 240,000 μC. The short BCI runs were performed to minimze the time lost if a target broke during a run. The same target was used for each on-off 30,000 μC data run. After each pair of measurements (on-resonance and off-resonance), the resonance was relocated; this reduced the effect of any energy shifts and also ensured that the background had not increased significantly. If the beam was too unstable during a run, the data for that run were discarded.

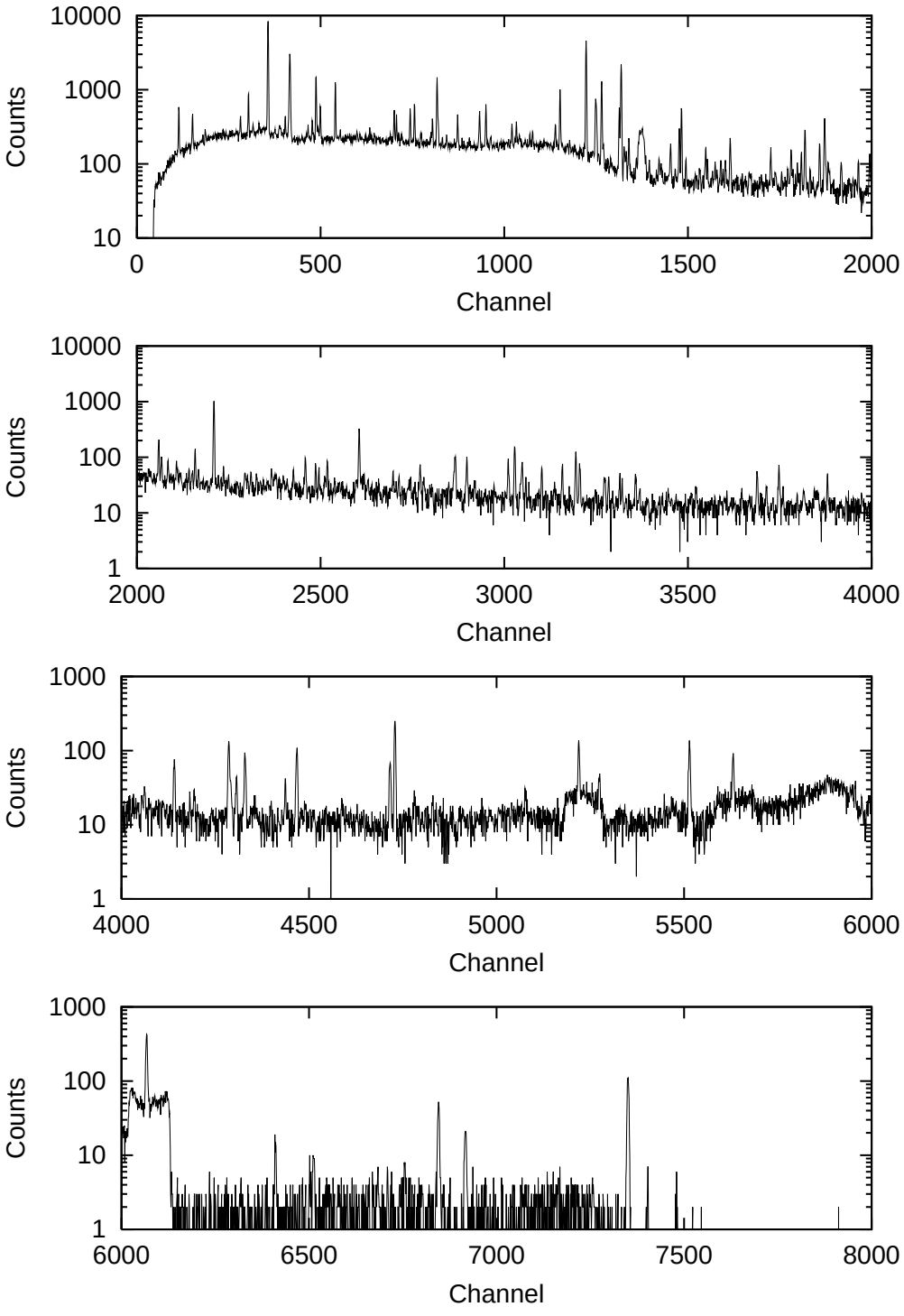

Figure 5.14: CSGe spectrum for the $E_p = 2.0615$ MeV resonance.

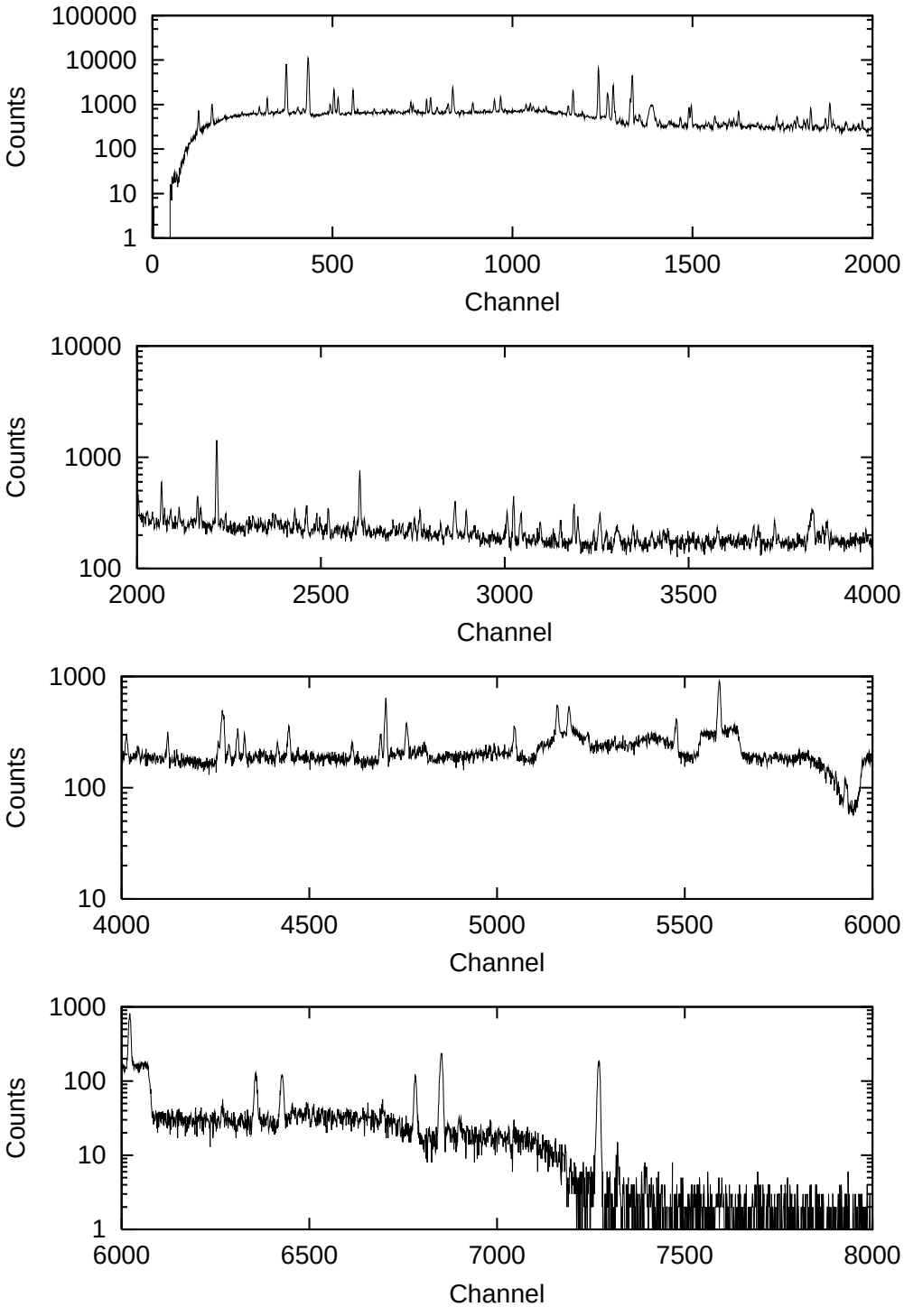

Figure 5.15: USGe spectrum for the $E_p = 2.0615$ MeV resonance.

Chapter 6

Preliminary Analysis of γ-Ray Spectra

This chapter discusses the analysis of the γ-ray spectra obtained for the 27 ^{49}V resonances. Section 6.1 describes the specialized software used to fit the peaks in the spectra. For a precise determination of the intensity of a specific transition, the centroid energy is required. Because the efficiency of germanium detectors is strongly energy dependent, one must accurately determine the γ-ray energy before making the efficiency correction. The energy and efficiency calibrations were performed off line using well known γ rays, from both a radioactive source and a nuclear reaction. Sections 6.2 and 6.3 discuss the software used and the procedures followed to calibrate the spectra for energy and efficiency, respectively.

6.1 Fitting Procedure

The γ-ray spectra obtained with the germanium detectors were analyzed using the software package GELIFT [Rad89]. GELIFT is a FORTRAN software package that uses least–squares fitting methods to fit the peaks in the γ-ray spectrum to a Gaussian shape. The fitting procedure allows two corrections to this Gaussian peak. The first correction is

a skewed Gaussian shape that accounts for missed charge collection in the detector due to impurities in the detector. The other correction adds a step function to account for the increased background at the lower energy side of the photopeaks. The fitting procedure also includes a background which is determined by a polynomial fit. The order of the highest polynomial in this fit is at most five. GELIFT can fit up to 15 peaks simultaneously and can store up to 20 peaks in its memory buffer before writing the fits to a data file. This data file, with the file extension STO, can be used by other GELIFT programs to perform energy calibration and efficiency corrections.

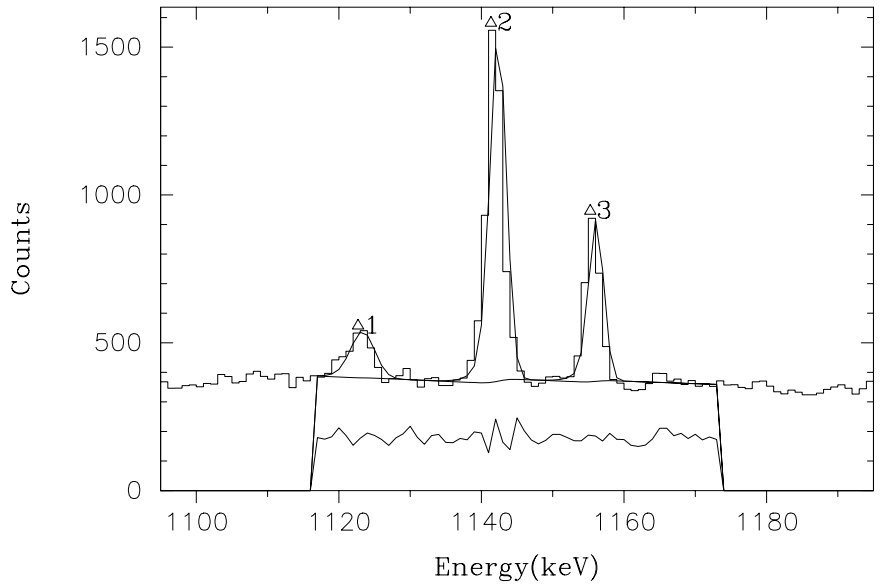

Figure 6.1: Peaks fitted with GELIFT for the 2.5004-MeV ^{49}V resonance. The jagged line midway between the fit and x-axis is the difference (with an offset zero) between the fit and data in counts.

An example of this fitting procedure is shown in Figure 6.1 for the γ-ray spectrum at the 2.5004-MeV resonance. The data are displayed as a histogram. The fitted peaks are represented by solid lines and denoted by triangles with numbers next to them. The background fit is the line running along the base of the fitted peaks. The lower, jagged, solid line lying between the background and the x–axis is the difference between the calculated fit and the data in counts per channel; it is offset from the x-axis for reasons of visibility.

6.2 Energy Calibration

The calibration was performed with well known γ rays from a ^{152}Eu radioactive source and from the ^{27}Al$(p,\gamma)^{28}$Si reaction. The specific peaks used for calibration are listed in Table 6.1 for the ^{152}Eu source and Table 6.2 for the ^{27}Al$(p,\gamma)^{28}$Si reaction. Typical spectra are shown in Figures 6.2 and 6.3. After these peaks were identified and fit as described in section 6.1, their areas, area uncertainties, centroids (in channel number) and centroid uncertainties were stored in a STO file. A source (SOU) file was also created that lists the known energies of the calibration γ rays, the errors in these energies, and the relative intensities and their errors at these energies.

Table 6.1: ^{152}Eu γ rays [a].

E_γ (keV)	ΔE_γ (keV)	I_γ (Relative)	ΔI_γ (Relative)
244.692	0.002	3590	60
295.939	0.008	211	5
344.276	0.004	12750	90
367.789	0.005	405	8
411.115	0.005	1070	10
488.661	0.039	195	2
688.678	0.006	400	8
778.903	0.006	6190	80
867.388	0.008	1990	40
964.131	0.009	6920	90
1212.950	0.012	670	8
1299.124	0.012	780	10
1408.011	0.014	10000	30

[a] From [Fir96].

After fitting the calibration γ rays, the program SOURCE creates a Source Intensity (SIN) file. The SIN file contains the peak channels of the fitted calibration γ rays and their uncertainties, the known energies of these γ rays (from the SOU file) and their known

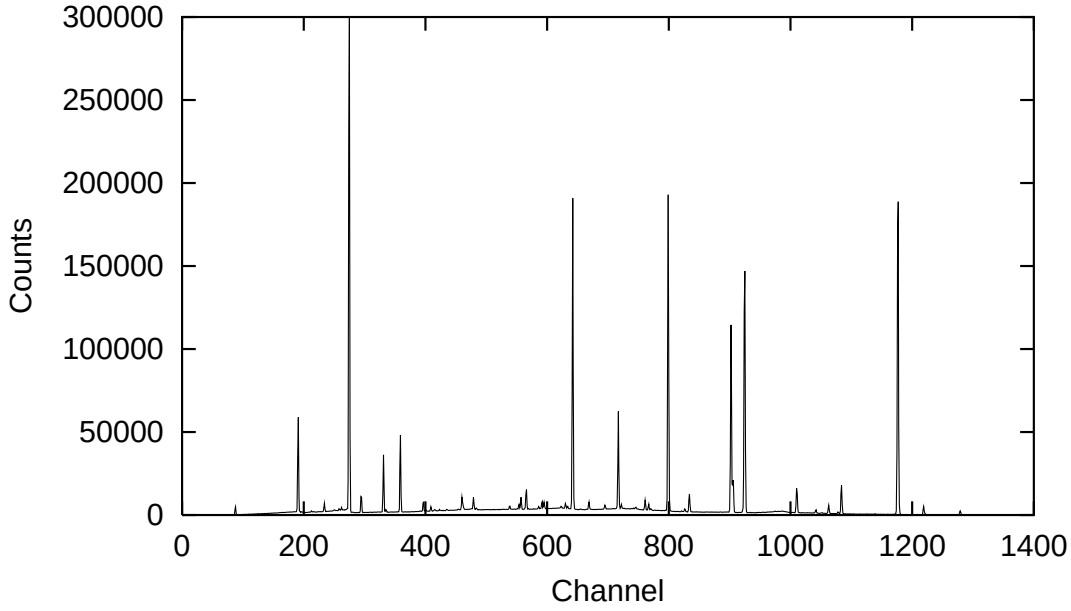

Figure 6.2: ^{152}Eu γ-ray spectrum used for the low-energy calibration of the CSGe detector.

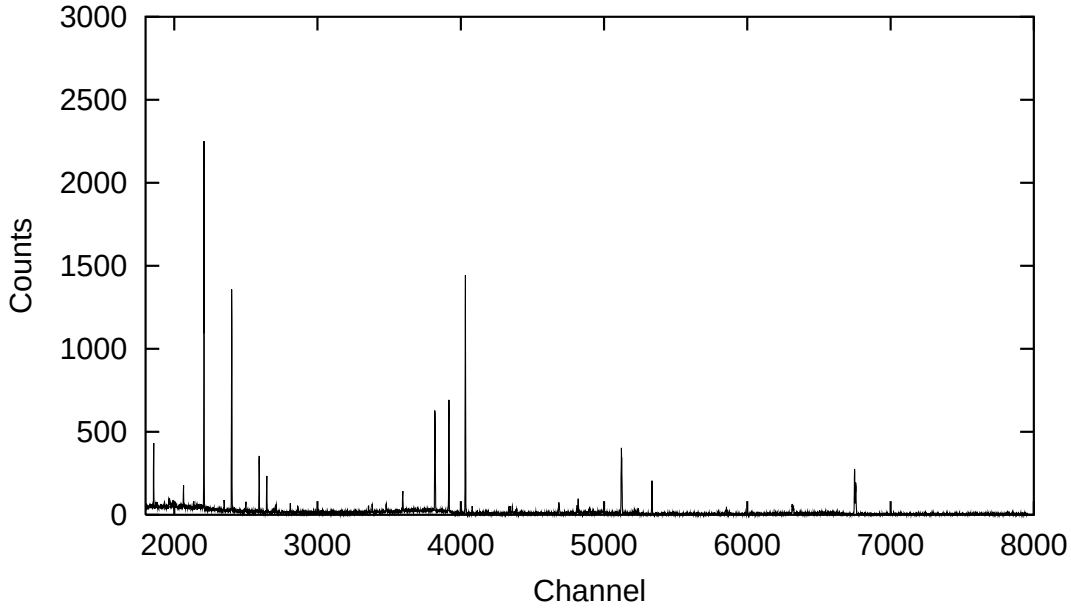

Figure 6.3: ^{28}Si γ-ray spectrum used for the high-energy calibration of the CSGe detector.

Table 6.2: ^{28}Si γ rays [a].

E_γ (keV)	ΔE_γ (keV)	I_γ (Relative)	ΔI_γ (Relative)
1522.81	0.02	2787	94
1658.34	0.02	610	16
1779.03	0.02	94766	4
1873.26	0.02	288	9
2838.83	0.03	5598	4
3061.82	0.03	1110	40
3124.14	0.03	790	30
4497.17	0.05	4563	26
4607.86	0.05	3960	120
4742.30	0.05	8500	300
4799.31	0.05	287	11
5662.52	0.06	700	20
6019.98	0.06	5634	94
6265.11	0.06	2150	70
6878.79	0.07	498	8
7923.45	0.08	4090	120
7933.45	0.08	3309	60

[a] From [End90].

Table 6.3: CSGe energy calibration parameters.

Coefficient	Low-Energy ($<$ 1523 keV)	High-Energy ($\geq$ 1523 keV)
c_0	0.1666×10^{2}	0.1715×10^{2}
c_1	0.1205×10^{1}	0.1194×10^{1}
c_2	$-.6368 \times 10^{-4}$	$-.1404 \times 10^{-4}$
c_3	0.9242×10^{-7}	0.3587×10^{-8}
c_4	$-.6756 \times 10^{-10}$	$-.4385 \times 10^{-12}$
c_5	0.1815×10^{-13}	0.2139×10^{-16}

relative intensities. (The intensities will be used for the efficiency calibrations.)

To calibrate, ENCAL fits the known energies to the peak channel obtained from the fit, using a least-squares procedure. An n^{th} order polynomial (n=1 to 5) is assumed:

$$E_\gamma(x) = \sum_{i=0}^{n} c_i x^i, \tag{6.1}$$

where the c_i are the fitting coefficients and x is the channel of the centroid of a peak in the spectrum. In practice $n = 5$ gave the most appropriate fit. Table 6.3 lists the polynomial coefficients for the energy calibration for the CSGe detector for the May 2003 data run. The best fit for the lower energy calibration using the ^{152}Eu source is shown in Figure 6.4. The upper portion of Figure 6.4 shows the fit (the line) and the known energies for ^{152}Eu calibration peaks (the points). The lower portion of the figure shows the energy difference between the fitted and known calibration peaks. Figure 6.5 shows the fit for the upper end of the energy spectrum.

The ^{152}Eu and ^{28}Si γ rays do not overlap in energy, and this leads to problems in ensuring that the energy calibration joins smoothly between the low-energy and high-energy regions. To ensure a smooth fit, the lowest γ ray in the high energy calibration (the 1553-keV ^{28}Si line) was included with the ^{152}Eu data. This γ ray thus becomes the highest energy γ ray of those used for the lower energy calibration. This procedure ensured that

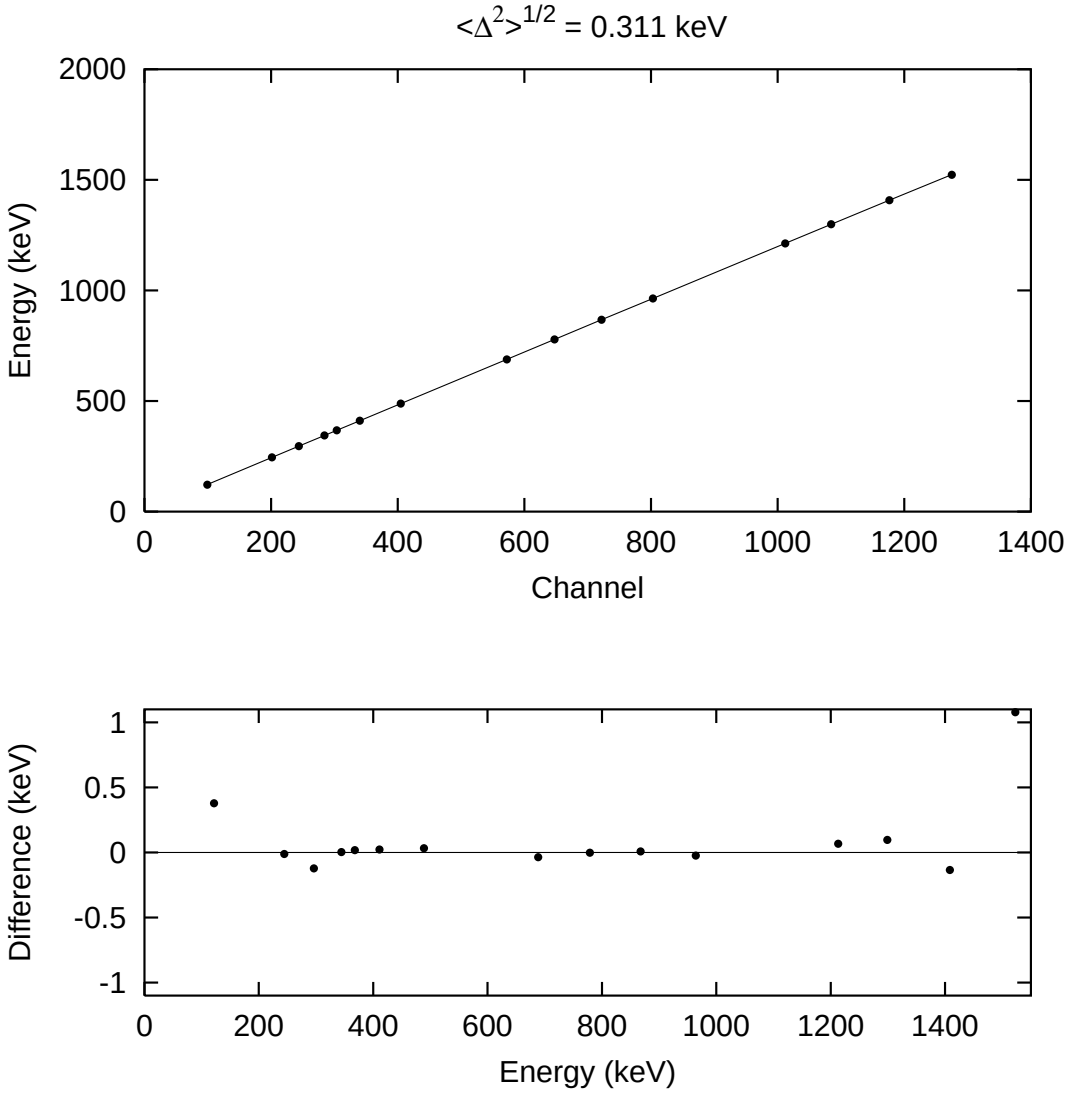

Figure 6.4: CSGe detector low-energy calibration using the ^{152}Eu γ rays. The data points and the 5^{th}-order polynomial fit are shown in the upper part of the figure. The difference between the data points and this fit are shown in the bottom part of the figure.

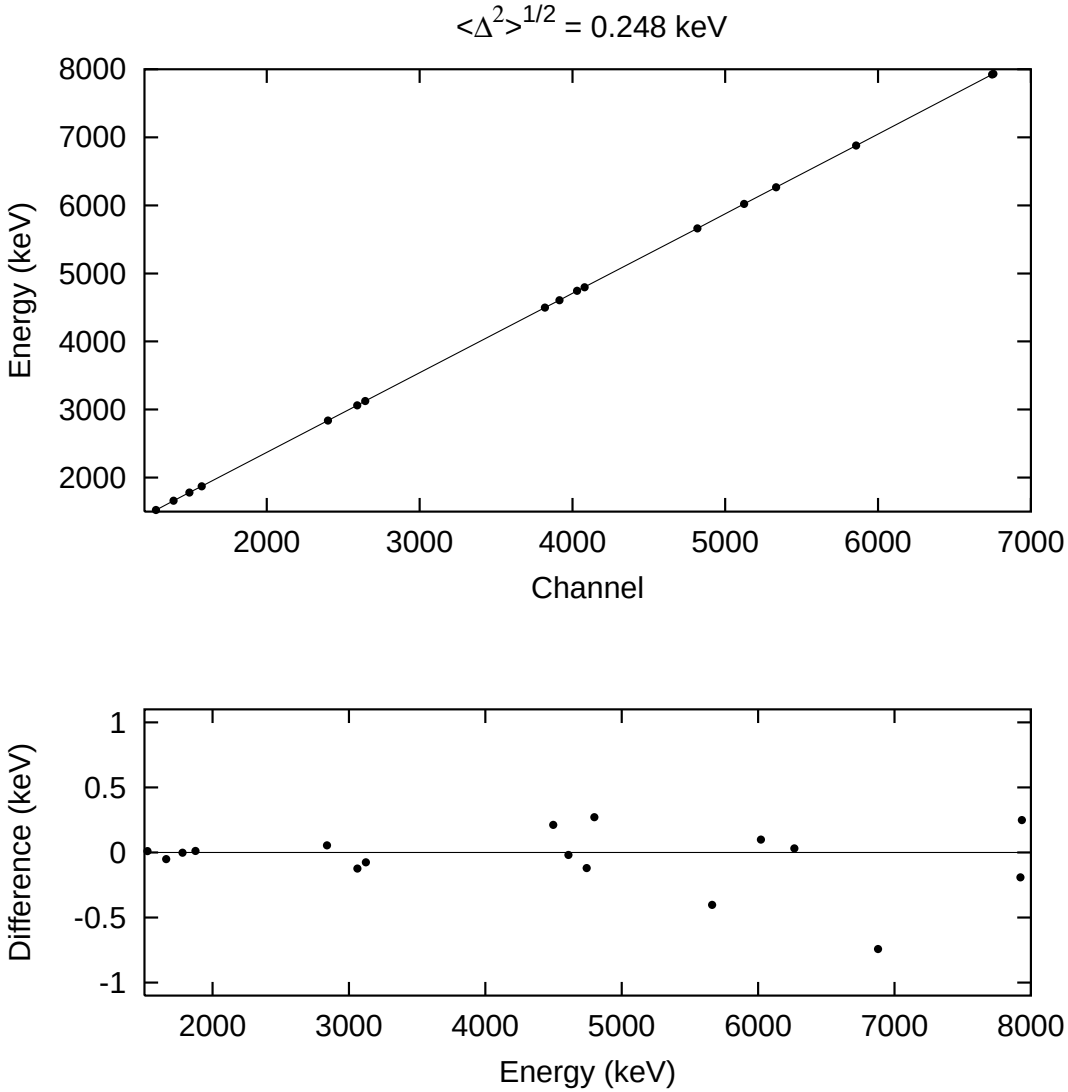

Figure 6.5: CSGe detector high-energy calibration using the ^{28}Si γ rays. The data points and the 5^{th}-order polynomial fit are shown in the upper part of the figure. The difference between the data points and this fit are shown in the bottom part of the figure.

the low and high energy calibrations joined smoothly at 1553 keV.

Once the appropriate fit is determined for the energy calibration, the coefficients of the n^{th}-order polynomial describing the fit are stored in a calibration (CAL) file for later use in calibrating experimental spectra. The CAL file will also be used by the program EFFIT in performing efficiency corrections.

6.3 Efficiency Calibration

The efficiency corrections are obtained by comparing the known intensities of a set of γ rays spanning the energy range of interest with the observed intensities for that same set of γ rays. EFFIT, another software program within GELIFT, determines the relative efficiency function by minimizing the rms deviation of the fitting function from the data. The low– and high–energy γ–ray intensities were first normalized by multiplying the ^{27}Al(p,γ)^{28}Si γ–ray intensities by a normalization factor. This normalization factor was determined iteratively by the user by multiplying the ^{27}Al(p,γ)^{28}Si γ–ray intensities by a number, running EFFIT, and comparing the fit with previous fits until the factor gave an efficiency fit with the smallest rms deviation. EFFIT uses the following function [Rad89] for the relative efficiency:

$$\epsilon = \exp\left[\left\{[A + Bu + Cu^2]^{-G} + [D + Ev + Fv^2]^{-G}\right\}^{\frac{-1}{G}}\right] , \tag{6.2}$$

where $u = \ln\left(\frac{E_\gamma}{100}\right)$, $v = \ln\left(\frac{E_\gamma}{1000}\right)$.

The coefficients determined from the efficiency fit are listed in Table 6.4. The fit for the Compton–suppressed detector is shown in Figure 6.6. The best fit parameters for the efficiency fit are saved to an efficiency (EFF) file.

Once the energy and efficiency calibrations are determined, the energy and efficiency corrections can be performed for any experimental spectrum with the GELIFT program ENERGY. This program reads in a STO file containing a number of fitted peaks. The appropriate ENCAL output (CAL) file is used, and the peak channels are converted to

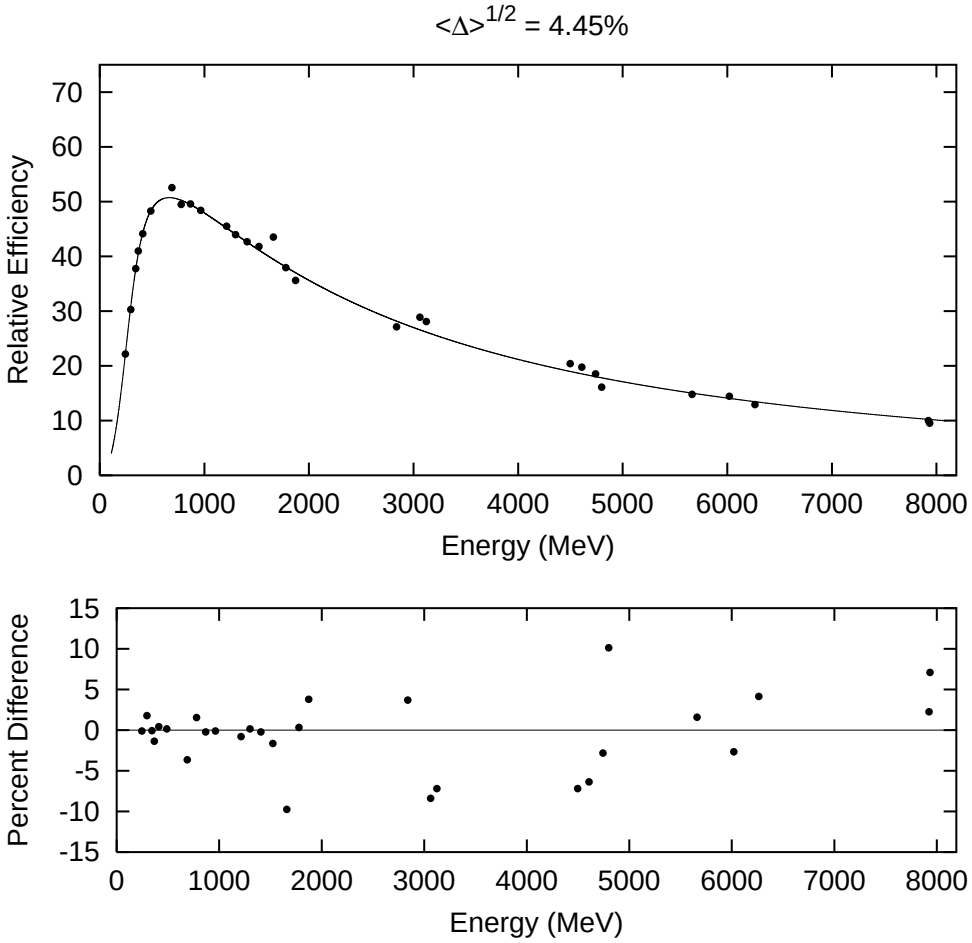

Figure 6.6: Data and fit for the CSGe detector efficiency calibration. The data points and the fit are shown in the upper part of the figure. The difference between the data points and the fit are shown in the bottom part of the figure.

Table 6.4: Efficiency calibration parameters.

Parameter	CSGe detector [a]	USGe detector [b]
A	1.1774	2.2932
B	2.1990	1.6619
C	0.000	0.000
D	3.8738	5.0659
E	-0.2750	-0.2501
F	-0.2287	-0.2750
G	9.64	11.85

[a] $\langle\Delta^2\rangle^{1/2} = 4.45\%$ as shown in Fig. 6.6.

[b] $\langle\Delta^2\rangle^{1/2} = 4.67\%$.

[c] This variable was set to 0.000 for the fit.

energies. The peak areas are then corrected for the energy dependence of the efficiency by dividing the peak area by the relative efficiency at the centroid energy. The results of these operations are written to an ENG file. For this experiment, a special code was written to read ENG files for each resonance and to form the ratios of the γ-ray intensities in order to test the low level population method. The ENG files were also used to determine experimental level populations to compare with predicted level populations for the 12 lowest ^{49}V energy levels.

Chapter 7

Results

In this chapter the results for the relative populations of 10 low-lying levels are presented for the 27 ^{49}V resonances studied. The next chapter will focus on the comparison of these measured relative populations with predictions by current models.

7.1 Relative Population of Low-lying Levels in ^{49}V

The γ-ray decay of 27 ^{49}V resonances was measured in the present experiment. Table 7.1 lists the energies and other parameters for the resonances studied in this experiment [Pro71, Wel78].

Table 7.2 lists the energies, spins and parities of the low-lying levels that were studied. Appendix A lists the γ-ray intensities for the decay from each resonance. Appendix B lists the relative populations for these low-lying levels for each resonance studied. A plot of the relative populations for each resonance is also included in Appendix B. The population of a given level was determined by summing the intensities of all of the observed γ rays emitted from that level and dividing this sum by the sum of branching ratios of the observed γ rays.

In this experiment the relative populations of the 12 lowest excited states in ^{49}V were initially considered. However, results were not obtained for two of these levels, the

Table 7.1: ^{49}V resonances studied.

$E_{Resonance}$ (MeV)	J^π	Γ_p (eV)	γ_p^2 (keV)	$\Gamma_{p\prime}$ (eV)	$\gamma_{p'}^2$ (keV)
2.0615	$\frac{1}{2}^+$	70	1.20		
2.1163	$(\frac{1}{2}^-)$	5	0.17		
2.1936	$\frac{3}{2}^-$	7	0.19	0.15	0.561
2.2045	$\frac{1}{2}^+$	25	0.28		
2.2108	$(\frac{1}{2}^-)$	10	0.26		
2.2121	$(\frac{1}{2}^-)$	20	0.51		
2.2308	$\frac{1}{2}^-$	25	0.61	0.22	0.505
2.2638	$\frac{1}{2}^-$	90	2.00	0.12	0.221
2.2885	$\frac{1}{2}^+$	40	0.36		
2.3182	$\frac{1}{2}^+$	100	0.85		
2.4660	$\frac{1}{2}^-$	225	2.96		
2.5004	$\frac{3}{2}^-$	15	0.18	0.18	0.086
2.5207	$\frac{1}{2}^+$	10	0.05		
2.5344	$\frac{3}{2}^-$	5	0.06	6.85	2.652
2.5419	$\frac{1}{2}^+$	10	0.05		
2.5575	$\frac{1}{2}^+$	15	0.07		
2.6081	$\frac{3}{2}^-$	5	0.05	5.00	1.318
2.6107	$\frac{3}{2}^-$	70	0.66	9.46	2.462
2.6180	$\frac{1}{2}^+$	300	1.32		
2.6371	$\frac{1}{2}^-$	25	0.22	9.00	1.892
2.6525	$\frac{1}{2}^-$	75	0.65		
2.6915	$\frac{1}{2}^-$	290	2.32		
2.6964	$\frac{3}{2}^-$	50	0.40	2.59	0.447
2.7007	$\frac{3}{2}^-$	15	0.12	4.60	0.778
2.7102	$\frac{1}{2}^+$	875	3.26		
2.7131	$\frac{1}{2}^+$	1900	7.04		
2.7153	$\frac{3}{2}^-$	30	0.23	9.69	1.534

Table 7.2: ^{49}V levels studied.

E_x (keV)	J^π	E_x (keV)	J^π
90.64	$\frac{5}{2}^-$	1514.5	$\frac{5}{2}^-$
152.93	$\frac{3}{2}^-$	1602.7	$\frac{7}{2}^+$
748.3	$\frac{3}{2}^+$	1643.2	$(\frac{3}{2}, \frac{5}{2})^-$
1021.6	$\frac{11}{2}^-$	1646.4	$\frac{1}{2}^+$
1140.5	$\frac{5}{2}^+$	1661.4	$\frac{3}{2}^-$
1155.3	$\frac{9}{2}^-$	1994.7	$\frac{3}{2}^{(+)}$

90.64-keV level and the 1643.2-keV level. The low energy 90.64-keV γ ray was not observed during this experiment. The population of the 1643.2-keV level can be determined by measuring the intensities of the two γ rays emitted from this level. The branching ratios for the two γ rays (1490.24 keV and 1553 keV) are 97.7% and 2.3%, respectively. This latter γ ray was not observed, consistent with the very small branching ratio. In the capture spectrum there is a γ ray with energy 1493.6 keV emitted from the 1646.43-keV, $\frac{1}{2}^+$ level and terminating at the 152.93-keV, $\frac{3}{2}^-$ level. The high purity germanium detectors used in this experiment had resolutions of $\sim$2.0 keV. Due to the detector resolution the 1490.24- and 1493.6-keV γ rays could not be resolved. Therefore the 1490.24- and 1493.6-keV γ rays were not considered. As a result the population of the 1643.2-keV level is not determined. For the 1646.43-keV level the other branches were used along with a correction for the contribution from the 1493.6-keV γ ray to determine the relative population.

There was also a resolution problem with the 1512- and 1514.4-keV γ rays. Due to difficulties in resolving these two γ rays, their intensities were not determined in these measurements.

The 984-keV γ ray could not be resolved from the 987-keV γ ray which originates from inelastic scattering to the first excited state in ^{48}Ti. The intensity of the γ ray from inelastic scattering completely dominates the capture γ ray. Therefore there is no new

experimental information concerning the 984-keV γ ray.

Two of the low-lying levels emit an 854-keV γ ray. These are the 1602.7- and 1994.7-keV levels; the branching ratios of the 854-keV γ rays are 8.36 % and 29.0 %, respectively. Because there was no way to separate the observed intensity to determine individual intensities for these two transitions, the intensity of the 854-keV γ ray was not used to determine the population of either level.

To summarize, of the 12 low-lying levels initially slated for study, results could not be obtained for two of these levels. The relative populations for the remaining 10 low-lying levels were determined by summing the intensity of the efficiency-corrected γ rays that are observed from that level. This sum was then divided by the sum of the branching ratios of these observed γ rays.

The root-mean-square deviation of the efficiency curve is 4.45%. It is quite difficult to determine how the efficiencies at different energies are correlated; they are certainly not independent. The uncertainties quoted for the γ–ray intensities do not include any uncertainty in relative efficiency. The uncertainties in relative populations are therefore underestimates of the true uncertainties.

The averaged relative populations are presented in both graphical and tabular form in Tables 7.3 to 7.8 and Figures 7.1 to 7.6. The relative populations have been calculated using two different averaging methods; in each case the average relative populations are determined separately for $1/2^+$, $1/2^-$, and $3/2^-$ resonances. The first is a simple unweighted average; the uncertainty is taken to be the sample standard deviation. This approach emphasizes the variation in the relative populations from resonance to resonance. The second averaging technique is a weighted average using standard error propagation techniques.

7.2 Data Tables and Graphs

Table 7.3: Unweighted average relative population of low-lying levels in ^{49}V for decay from $\frac{1}{2}^+$ resonances.

E_{Level} (keV)	Population	E_{Level} (keV)	Population
152.9	0.30 ± 0.08	1514.5	0.05 ± 0.02
748.3	0.20 ± 0.07	1602.7	0.05 ± 0.04
1021.6	0.003 ± 0.006	1646.4	0.07 ± 0.07
1140.5	0.09 ± 0.03	1661.4	0.15 ± 0.09
1155.3	0.02 ± 0.02	1994.7	0.07 ± 0.03

Table 7.4: Weighted average relative population of low-lying levels in ^{49}V for decay from $\frac{1}{2}^+$ resonances.

E_{Level} (keV)	Population	E_{Level} (keV)	Population
152.9	0.285 ± 0.003	1514.5	0.036 ± 0.001
748.3	0.200 ± 0.001	1602.7	0.033 ± 0.001
1021.6	0.0065 ± 0.0003	1646.4	0.026 ± 0.001
1140.5	0.0943 ± 0.0009	1661.4	0.0987 ± 0.0009
1155.3	0.0168 ± 0.0003	1994.7	0.054 ± 0.001

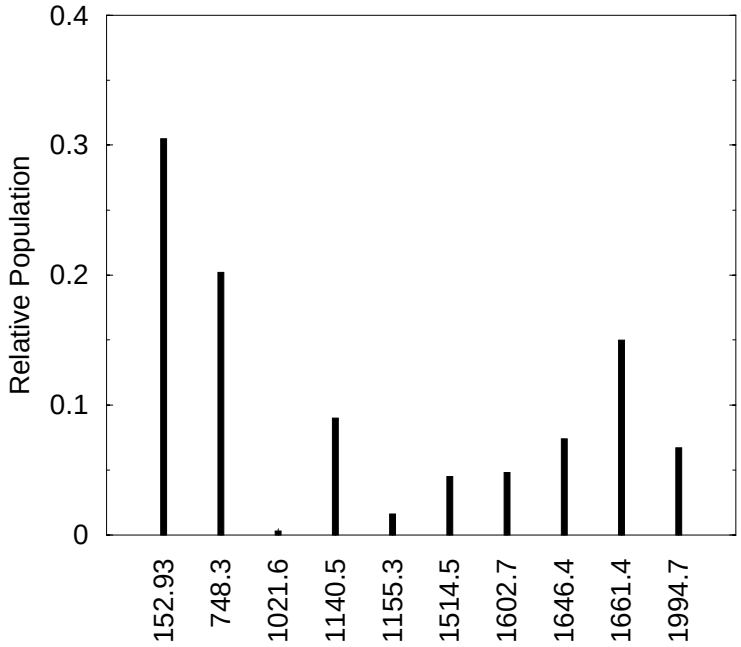

Figure 7.1: Unweighted average relative population of low-lying levels in ^{49}V for decay of $\frac{1}{2}^+$ resonances.

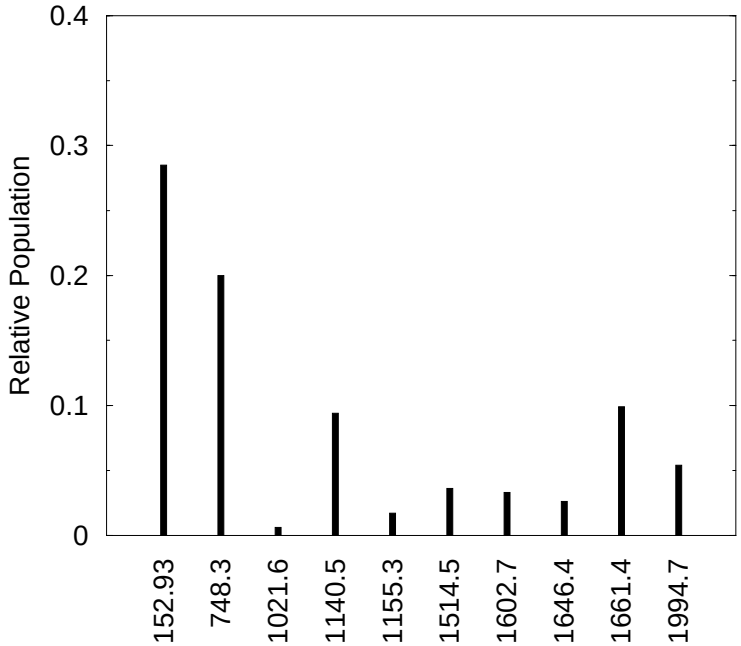

Figure 7.2: Weighted average relative population of low-lying levels in ^{49}V for decay from $\frac{1}{2}^+$ resonances.

Table 7.5: Unweighted average relative population of low-lying levels in ^{49}V for decay from $\frac{1}{2}^-$ resonances.

E_{Level} (keV)	Population	E_{Level} (keV)	Population
152.9	0.3 ± 0.1	1514.5	0.05 ± 0.03
748.3	0.2 ± 0.1	1602.7	0.02 ± 0.02
1021.6	0.005 ± 0.007	1646.4	0.13 ± 0.09
1140.5	0.07 ± 0.03	1661.4	0.10 ± 0.04
1155.3	0.01 ± 0.01	1994.7	0.05 ± 0.02

Table 7.6: Weighted average relative population for low-lying levels in ^{49} for decay from $\frac{1}{2}^-$ resonances.

E_{Level} (keV)	Population	E_{Level} (keV)	Population
152.9	0.314 ± 0.004	1514.5	0.036 ± 0.001
748.3	0.163 ± 0.002	1602.7	0.019 ± 0.001
1021.6	0.0090 ± 0.0005	1646.4	0.051 ± 0.002
1140.5	0.070 ± 0.001	1661.4	0.094 ± 0.001
1155.3	0.0154 ± 0.0007	1994.7	0.043 ± 0.001

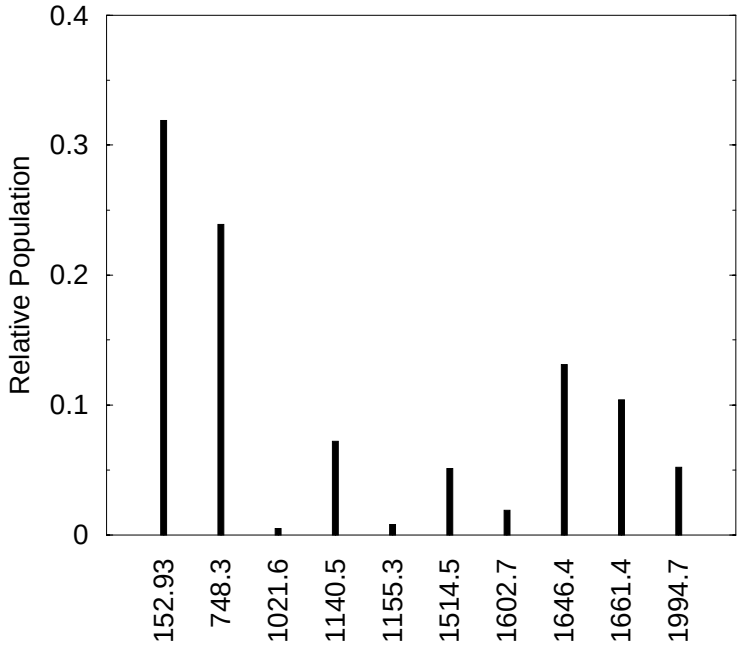

Figure 7.3: Unweighted average relative population of low-lying levels in ^{49}V for decay from $\frac{1}{2}^-$ resonances.

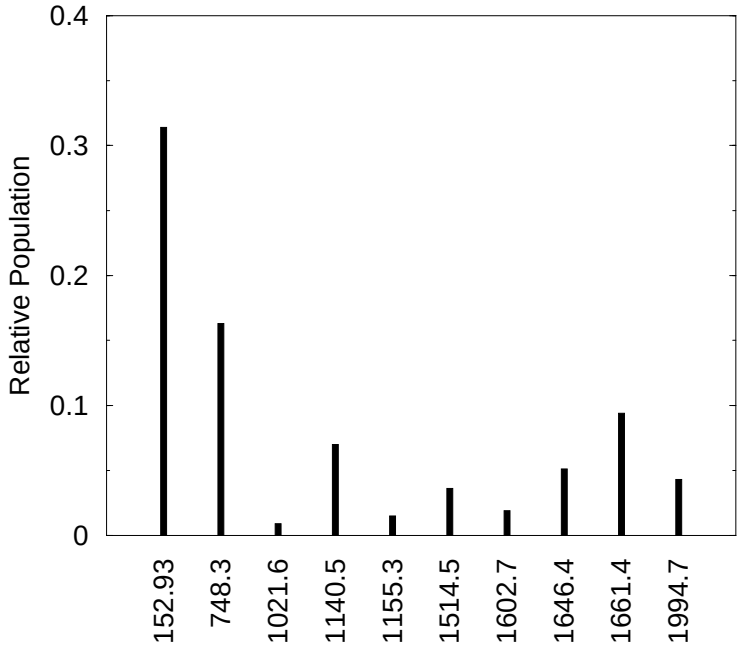

Figure 7.4: Weighted average relative population of low-lying levels in ^{49}V for decay from $\frac{1}{2}^-$ resonances.

Table 7.7: Unweighted average population of low-lying levels in ^{49}V for decay from $\frac{3}{2}^-$ resonances.

E_{Level} (keV)	Population	E_{Level} (keV)	Population
152.9	0.3 ± 0.2	1514.5	0.07 ± 0.04
748.3	0.17 ± 0.05	1602.7	0.03 ± 0.03
1021.6	0.03 ± 0.04	1646.4	0.07 ± 0.05
1140.5	0.12 ± 0.04	1661.4	0.10 ± 0.04
1155.3	0.04 ± 0.03	1994.7	0.07 ± 0.03

Table 7.8: Weighted average population of low-lying levels in ^{49}V for decay from $\frac{3}{2}^-$ resonances.

E_{Level} (keV)	Population	E_{Level} (keV)	Population
152.9	0.307 ± 0.003	1514.5	0.044 ± 0.001
748.3	0.142 ± 0.001	1643.2	0.020 ± 0.001
1021.6	0.0012 ± 0.0001	1646.4	0.037 ± 0.002
1140.5	0.106 ± 0.001	1661.4	0.0753 ± 0.0009
1155.3	0.0090 ± 0.0002	1994.7	0.048 ± 0.002

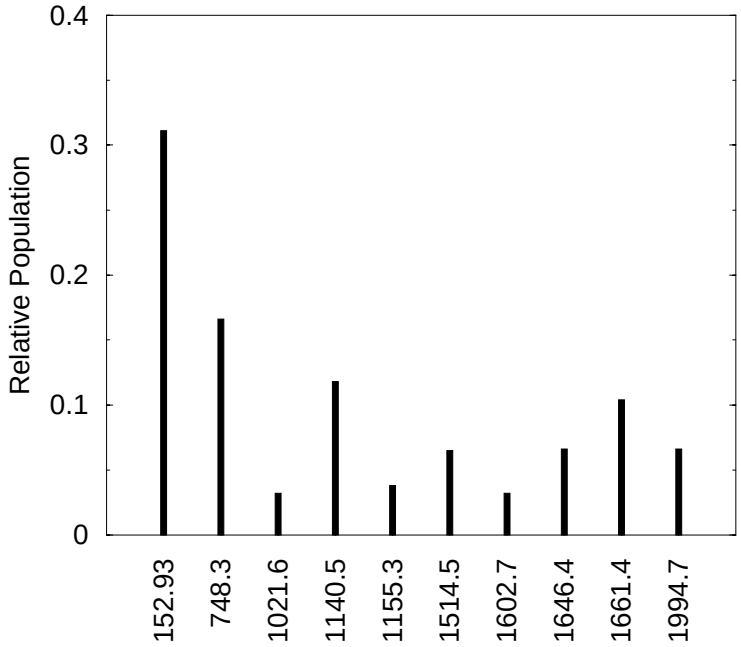

Figure 7.5: Unweighted average relative population of low-lying levels in ^{49}V for decay from $\frac{3}{2}^-$ resonances.

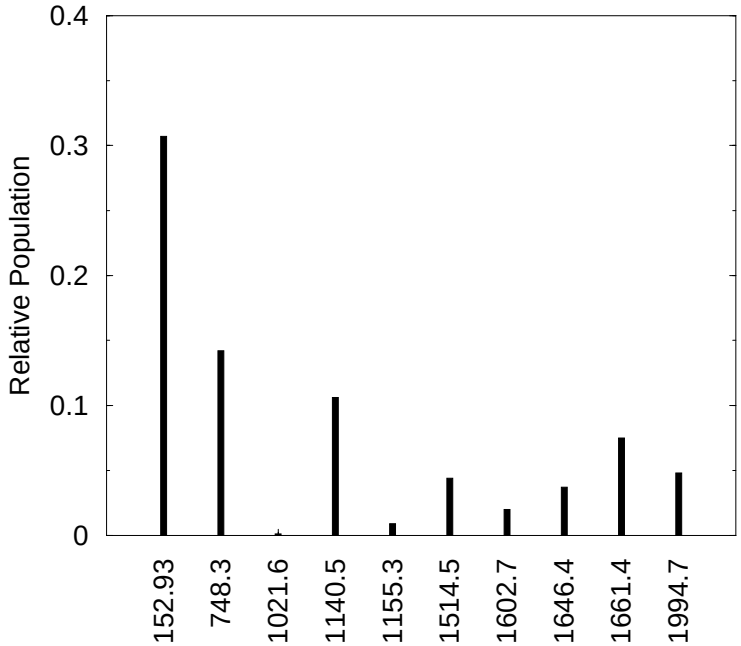

Figure 7.6: Weighted average relative population of low-lying levels in ^{49}V for decay from $\frac{3}{2}^-$ resonances.

Chapter 8

Analysis

The first part of this chapter is devoted to comparison of the experimental relative populations of the low-lying levels in ^{49}V with predictions using the DICEBOX simulation program and standard strength function and level-density models. In the second part the low level population method for determining resonance spins is considered; again, the experimental results are compared with predictions of DICEBOX simulations.

8.1 Comparison of Relative Population of Low-lying Levels with DICEBOX Predictions

Table 8.1 lists the values used for the level density in simulations of the population of low-lying ^{49}V states [Krt02]. Since the level densities in this mass region are considered much better established than the radiative strength functions, the level density parameters were fixed for all but one of the simulations. For the first series of simulations, standard giant resonance (GR) parameters were assumed for the E1, M1, and E2 radiative strength functions. These parameters were $E^{E1} = 17.86$ MeV, $\sigma^{E1} = 58.8$ mb and $\Gamma^{E1} = 4.42$ MeV for the E1 strength function; $E^{M1} = 11.20$ MeV, $\sigma^{M1} = 3.00$ mb and $\Gamma^{M1} = 3.00$ MeV for the M1 strength function; and $E^{E2} = 17.22$ MeV, $\sigma^{E2} = 1.20$ mb and $\Gamma^{E2} = 5.52$

MeV for the E2 strength function [Krt02]. Here this simulation is called the GR model.

Table 8.1: Level density parameters for DICEBOX simulations.

Model	E_o (MeV)	E_1 (MeV)	T (MeV)	a (MeV^{-1})	$\triangle$ (MeV)
a [a]	-2.72	-1.22	1.50	5.10	0.808
b [b]	-2.72	-1.22	3.00	5.10	0.808

[a] Used for GR and SP models. [Krt02]

[b] Used for temperature change in E1 GDR strength function.

In Figures 8.1, 8.2 and 8.3 and tables 8.2, 8.3, and 8.4, the DICEBOX predictions of the relative populations for the GR model are compared with the experimental values. The comparison is shown separately for the three different ^{49}V resonance spins. As noted earlier the experimental average relative populations were determined with two methods. One major difference between the results for the weighted and unweighted average populations is that the unweighted averages have much larger uncertainties. The relative population of low-lying levels varies considerably from resonance to resonance. In Appendix C the results of DICEBOX simulations for the 27 individual resonances are presented. For these calculations the GR model parameters were employed.

The figures and tables reveal qualitative agreement between DICEBOX predictions and experiment; levels that are weakly or strongly populated experimentally are also predicted to be weakly or strongly populated. The most striking disagreement visually is for the 152.93-keV level, but closer inspection also reveals a systematic disagreement for the weakly populated higher spin states. For the higher spin states, the DICEBOX calculations usually are much smaller than the experimental values. As discussed in the second part of this chapter, this result has important implications for the LLP method.

Table 8.2: Comparison of experimental relative populations with DICEBOX predictions (GR model) for $\frac{1}{2}^+$ resonances.

E_{Level} (keV)	Unweighted Average	Weighted Average	DICEBOX Average
152.9	0.31 ± 0.08	0.285 ± 0.003	0.52 ± 0.03
748.3	0.20 ± 0.07	0.200 ± 0.001	0.22 ± 0.03
1021.6	0.003 ± 0.006	0.0060 ± 0.0003	< 0.0001
1140.5	0.09 ± 0.03	0.0940 ± 0.0009	0.041 ± 0.007
1155.3	0.02 ± 0.02	0.0170 ± 0.0003	< 0.0001
1514.5	0.05 ± 0.02	0.036 ± 0.001	0.0110 ± 0.0014
1602.7	0.05 ± 0.04	0.033 ± 0.001	0.0010 ± 0.0004
1646.4	0.07 ± 0.07	0.026 ± 0.001	0.07 ± 0.02
1661.4	0.15 ± 0.09	0.0990 ± 0.0009	0.07 ± 0.02
1994.7	0.07 ± 0.03	0.054 ± 0.001	0.06 ± 0.02

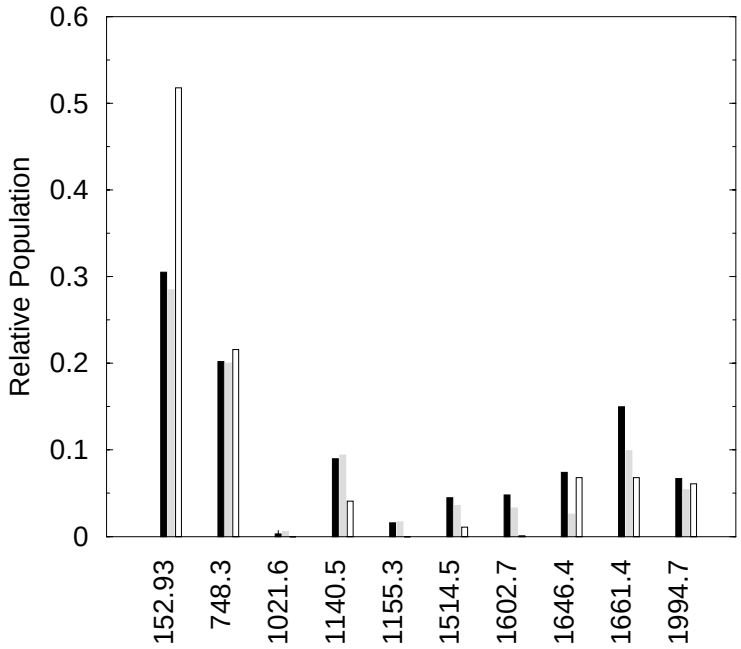

Figure 8.1: Relative population of low-lying levels by $\frac{1}{2}^+$ resonances: experimental unweighted (black), experimental weighted (gray) and DICEBOX GR model (white).

Table 8.3: Comparison of experimental relative populations with DICEBOX predictions (GR model) for $\frac{1}{2}^-$ resonances.

E_{Level} (keV)	Unweighted Average	Weighted Average	DICEBOX Average
152.9	0.3 ± 0.1	0.314 ± 0.004	0.54 ± 0.04
748.3	0.2 ± 0.1	0.163 ± 0.002	0.18 ± 0.03
1021.6	0.005 ± 0.007	0.0090 ± 0.0005	< 0.0001
1140.5	0.07 ± 0.03	0.070 ± 0.001	0.035 ± 0.006
1155.3	0.01 ± 0.01	0.0150 ± 0.0007	< 0.0001
1514.5	0.05 ± 0.03	0.036 ± 0.001	0.015 ± 0.003
1602.7	0.02 ± 0.02	0.019 ± 0.001	0.0010 ± 0.0003
1646.4	0.13 ± 0.09	0.051 ± 0.002	0.08 ± 0.03
1661.4	0.10 ± 0.04	0.094 ± 0.001	0.07 ± 0.02
1994.7	0.05 ± 0.02	0.043 ± 0.001	0.06 ± 0.02

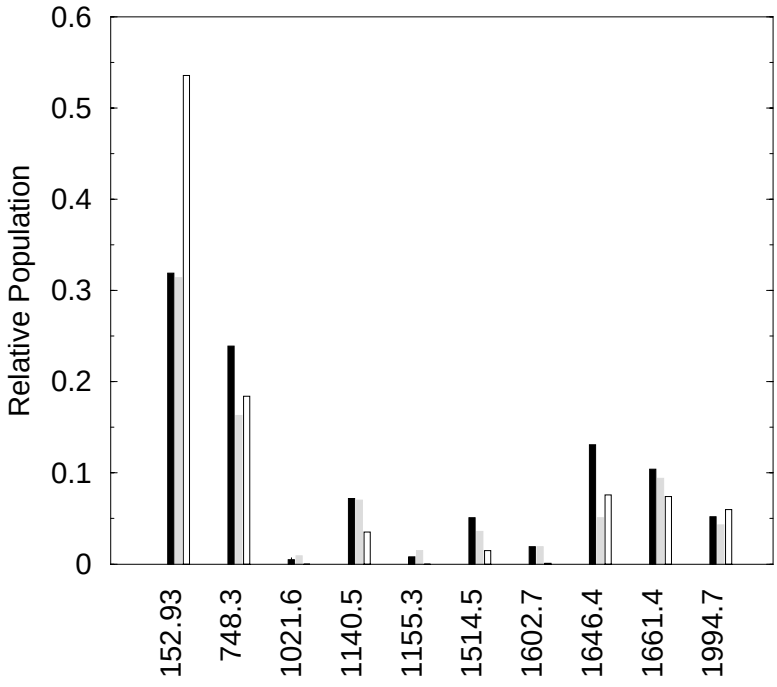

Figure 8.2: Relative population of low-lying levels by $\frac{1}{2}^-$ resonances: experimental unweighted (black), experimental weighted (gray) and DICEBOX GR model (white).

Table 8.4: Comparison of experimental relative populations with DICEBOX predictions (GR model) for $\frac{3}{2}^-$ resonances.

E_{Level} (keV)	Unweighted Average	Weighted Average	DICEBOX Average
152.9	0.3 ± 0.2	0.307 ± 0.003	0.51 ± 0.05
748.3	0.17 ± 0.05	0.142 ± 0.001	0.18 ± 0.03
1021.6	0.03 ± 0.04	0.0010 ± 0.0001	< 0.0001
1140.5	0.12 ± 0.04	0.106 ± 0.001	0.09 ± 0.02
1155.3	0.04 ± 0.03	0.0090 ± 0.0002	0.0030 ± 0.0004
1514.5	0.07 ± 0.04	0.044 ± 0.001	0.06 ± 0.02
1602.7	0.03 ± 0.03	0.020 ± 0.001	0.0060 ± 0.0008
1646.4	0.07 ± 0.05	0.037 ± 0.002	0.05 ± 0.02
1661.4	0.10 ± 0.04	0.0750 ± 0.0009	0.06 ± 0.02
1994.7	0.07 ± 0.03	0.048 ± 0.002	0.05 ± 0.01

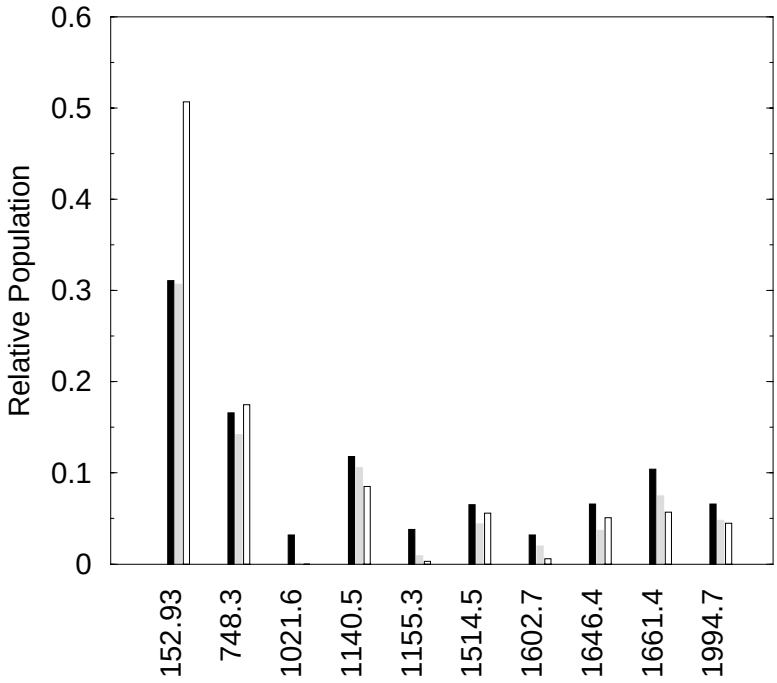

Figure 8.3: Relative population of low-lying levels by $\frac{3}{2}^-$ resonances: experimental unweighted (black), experimental weighted (gray) and DICEBOX GR model (white).

A similar series of calculations was performed with the same GDR parameters for the E1 radiative strength function. However, for the M1 and E2 radiative strength functions the single particle parameters $\kappa_{M1} = 6.0 \times 10^{-9}$ (MeV^{-3}) [Gun95] and $\kappa_{E2} = 1.76 \times 10^{-11}$ (MeV^{-5}) [Zan98] were used for the M1 and E2 single particle models, respectively. This series of simulations is labeled the Single Particle (SP) model.

The results for the DICEBOX calculations using the single particle model for the M1 and E2 radiative strength functions are presented in Figures 8.4, 8.5 and 8.6 and Tables 8.5, 8.6 and 8.7. There are only relatively minor changes in the predictions for the relative populations with these two rather different simulations. The qualitative results appear to be rather insensitive to even major changes in the M1 and E2 strength functions. To test this dependence further, simulations were repeated with values of the SP strengths of both the M1 and E2 strength functions first halved and then doubled. The relative populations of the low-lying levels were very little changed.

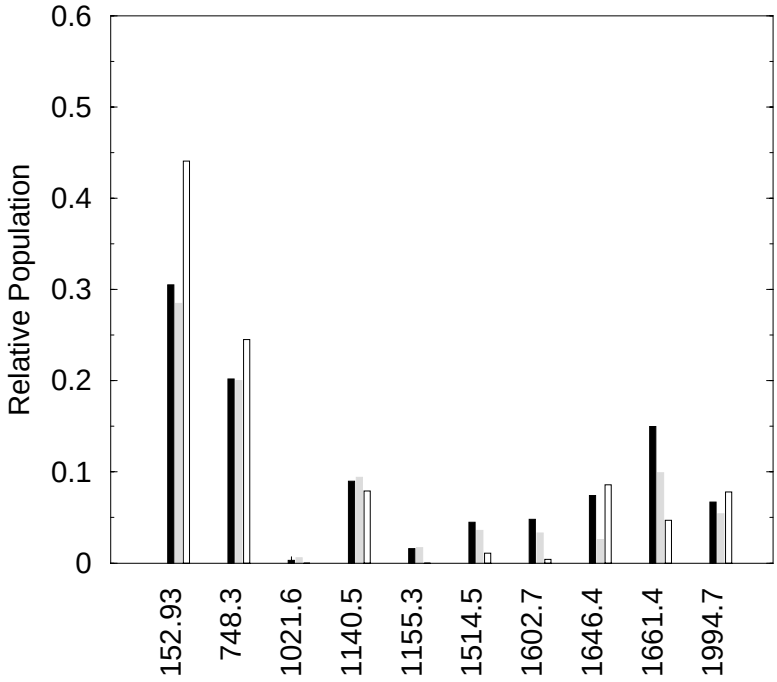

Figure 8.4: Relative population of low-lying levels by $\frac{1}{2}^+$ resonances: experimental unweighted (black), experimental weighted (gray) and DICEBOX SP model (white).

Table 8.5: Comparison of experimental relative populations with DICEBOX predictions (SP model) for $\frac{1}{2}^+$ resonances.

E_{Level} (keV)	Unweighted Average	Weighted Average	DICEBOX Average
152.9	0.31 ± 0.08	0.285 ± 0.003	0.44 ± 0.02
748.3	0.20 ± 0.07	0.200 ± 0.001	0.25 ± 0.02
1021.6	0.003 ± 0.006	0.0060 ± 0.0003	< 0.0001
1140.5	0.09 ± 0.03	0.0940 ± 0.0009	0.079 ± 0.003
1155.3	0.02 ± 0.02	0.0170 ± 0.0003	< 0.0001
1514.5	0.05 ± 0.02	0.036 ± 0.001	0.0110 ± 0.0009
1602.7	0.05 ± 0.04	0.033 ± 0.001	0.0030 ± 0.0004
1646.4	0.07 ± 0.07	0.026 ± 0.001	0.09 ± 0.02
1661.4	0.15 ± 0.09	0.0990 ± 0.0009	0.05 ± 0.01
1994.7	0.07 ± 0.03	0.054 ± 0.001	0.08 ± 0.01

Table 8.6: Comparison of experimental relative populations with DICEBOX predictions (SP model) for $\frac{1}{2}^-$ resonances.

E_{Level} (keV)	Unweighted Average	Weighted Average	DICEBOX Average
152.9	0.3 ± 0.1	0.314 ± 0.004	0.56 ± 0.03
748.3	0.2 ± 0.1	0.163 ± 0.002	0.16 ± 0.02
1021.6	0.005 ± 0.007	0.0090 ± 0.0005	< 0.0001
1140.5	0.07 ± 0.03	0.070 ± 0.001	0.034 ± 0.005
1155.3	0.01 ± 0.01	0.0150 ± 0.0007	< 0.0001
1514.5	0.05 ± 0.03	0.036 ± 0.001	0.033 ± 0.005
1602.7	0.02 ± 0.02	0.019 ± 0.001	0.0010 ± 0.0003
1646.4	0.13 ± 0.09	0.051 ± 0.002	0.05 ± 0.02
1661.4	0.10 ± 0.04	0.094 ± 0.001	0.10 ± 0.02
1994.7	0.05 ± 0.02	0.043 ± 0.001	0.04 ± 0.01

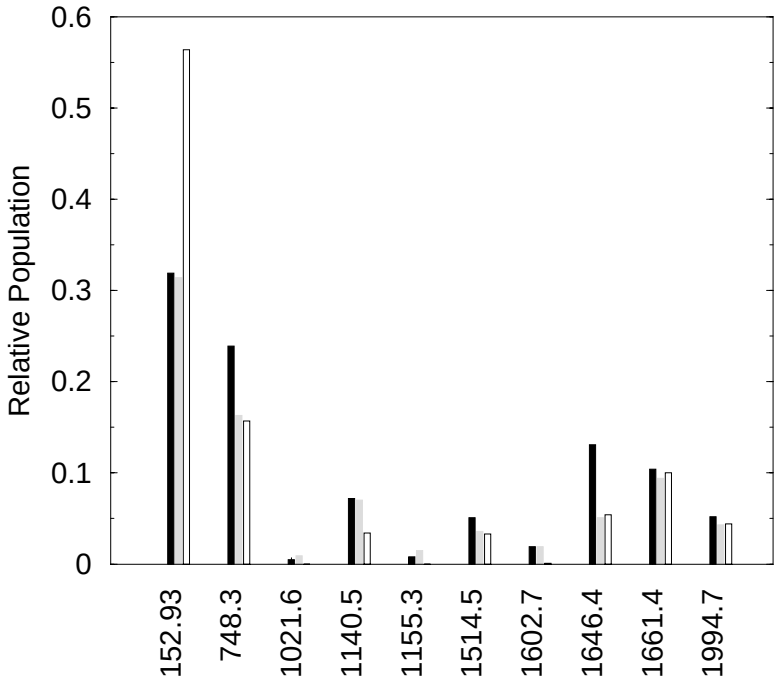

Figure 8.5: Relative population of low-lying levels by $\frac{1}{2}^-$ resonances: experimental unweighted (black), experimental weighted (gray) and DICEBOX SP model (white).

Table 8.7: Comparison of experimental relative populations with DICEBOX predictions (SP model) for $\frac{3}{2}^-$ resonances.

E_{Level} (keV)	Unweighted Average	Weighted Average	DICEBOX Average
152.9	0.3 ± 0.2	0.307 ± 0.003	0.52 ± 0.03
748.3	0.17 ± 0.05	0.142 ± 0.001	0.15 ± 0.02
1021.6	0.03 ± 0.04	0.0010 ± 0.0001	0.001 ± 0.001
1140.5	0.12 ± 0.04	0.106 ± 0.001	0.08 ± 0.01
1155.3	0.04 ± 0.03	0.0090 ± 0.0002	0.0060 ± 0.0009
1514.5	0.07 ± 0.04	0.044 ± 0.001	0.07 ± 0.01
1602.7	0.03 ± 0.03	0.020 ± 0.001	0.010 ± 0.001
1646.4	0.07 ± 0.05	0.037 ± 0.002	0.04 ± 0.01
1661.4	0.10 ± 0.04	0.0750 ± 0.0009	0.08 ± 0.02
1994.7	0.07 ± 0.03	0.048 ± 0.002	0.036 ± 0.009

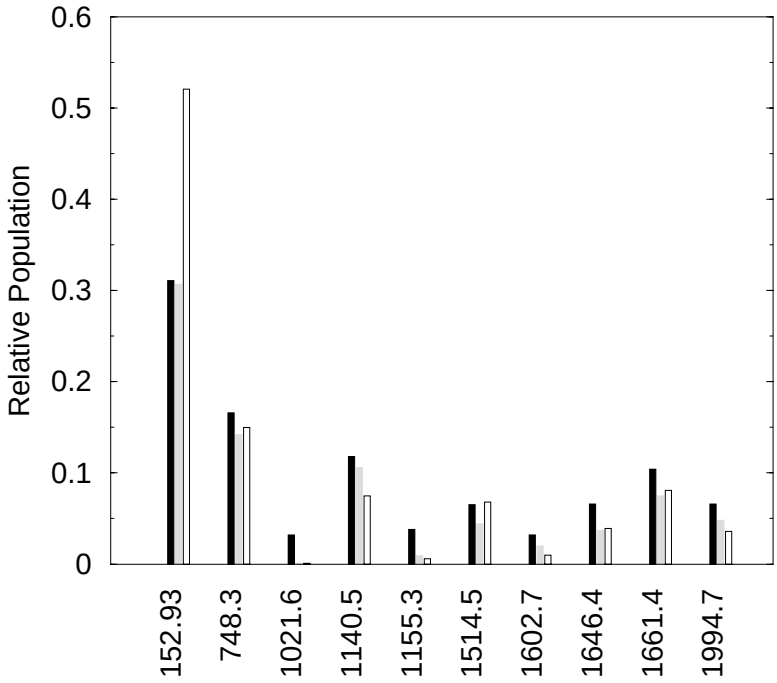

Figure 8.6: Relative population of low-lying levels by $\frac{3}{2}^-$ resonances: experimental unweighted (black), experimental weighted (gray) and DICEBOX SP model (white).

The qualitative insensitivity of the DICEBOX predictions for the relative population of the low-lying levels to variations of the M1 and E2 parameters is consistent with the dominance of the E1 strength function in the radiative decay of ^{49}V. Previous studies of the E1 radiative strength function lend confidence to most of the model parameters. The primary uncertainty involves the lower energy region [Kop90]. The key parameter governing the behavior in the low energy region is the temperature. To test the temperature dependence all parameters of the GR simulation were fixed, except that the temperature was doubled. This is called the GR model with temperature change. There was no large qualitative changes in the model predictions for these very different temperatures. This is illustrated in Figures 8.7, 8.8 and 8.9 and Tables 8.8, 8.9 and 8.10.

To summarize the DICEBOX predictions provide only a qualitative description of the experimental results. The simulations appear rather insensitive even to major changes in the radiative strength functions. The most obvious reason for the disagreement is the neglect of nuclear structure effects. However, modelling the radiative decay of nuclear resonances in this mass regions on a purely statistical basis does provide at least a qualitative prediction for the relative population of the low-lying states by compound nuclear resonances.

Table 8.8: Comparison of experimental relative populations with DICEBOX predictions (GR model with temperature change) for $\frac{1}{2}^+$ resonances.

E_{Level} (keV)	Unweighted Average	Weighted Average	DICEBOX Average
152.9	0.31 ± 0.08	0.285 ± 0.003	0.51 ± 0.05
748.3	0.20 ± 0.07	0.200 ± 0.001	0.22 ± 0.05
1021.6	0.003 ± 0.006	0.0060 ± 0.0003	< 0.0001
1140.5	0.09 ± 0.03	0.0940 ± 0.0009	0.030 ± 0.009
1155.3	0.02 ± 0.02	0.0170 ± 0.0003	< 0.0001
1514.5	0.05 ± 0.02	0.036 ± 0.001	0.0010 ± 0.0002
1602.7	0.05 ± 0.04	0.033 ± 0.001	< 0.0001
1646.4	0.07 ± 0.07	0.026 ± 0.001	0.08 ± 0.03
1661.4	0.15 ± 0.09	0.0990 ± 0.0009	0.08 ± 0.03
1994.7	0.07 ± 0.03	0.054 ± 0.001	0.06 ± 0.03

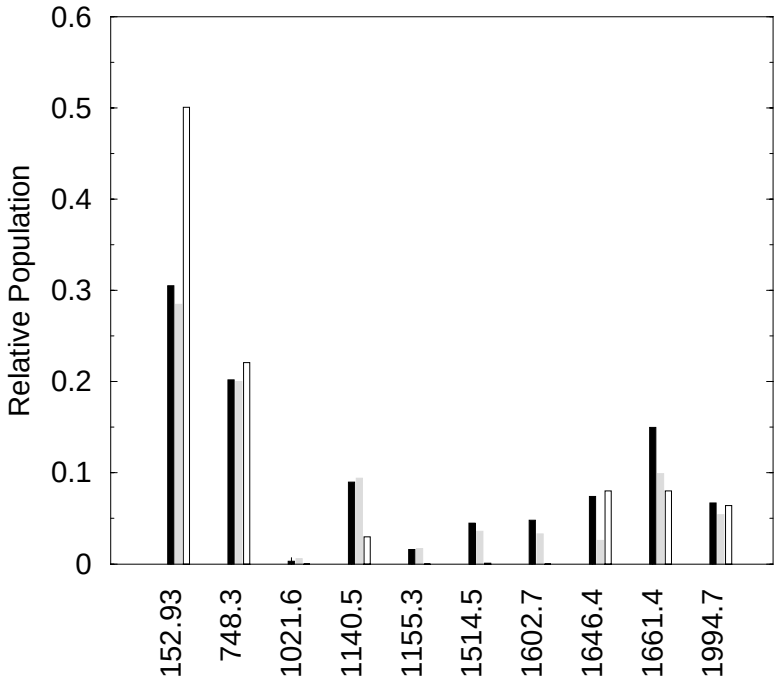

Figure 8.7: Relative population of low-lying levels by $\frac{1}{2}^+$ resonances: experimental unweighted (black), experimental weighted (gray) and DICEBOX GR model with temperature change (white).

Table 8.9: Comparison of experimental relative populations with DICEBOX predictions (GR model with temperature change) for $\frac{1}{2}^-$ resonances.

E_{Level} (keV)	Unweighted Average	Weighted Average	DICEBOX Average
152.9	0.3 ± 0.1	0.314 ± 0.004	0.56 ± 0.05
748.3	0.2 ± 0.1	0.163 ± 0.002	0.18 ± 0.04
1021.6	0.005 ± 0.007	0.0090 ± 0.0005	< 0.0001
1140.5	0.07 ± 0.03	0.070 ± 0.001	0.019 ± 0.007
1155.3	0.01 ± 0.01	0.0150 ± 0.0007	< 0.0001
1514.5	0.05 ± 0.03	0.036 ± 0.001	0.008 ± 0.004
1602.7	0.02 ± 0.02	0.019 ± 0.001	< 0.0001
1646.4	0.13 ± 0.09	0.051 ± 0.002	0.07 ± 0.03
1661.4	0.10 ± 0.04	0.094 ± 0.001	0.07 ± 0.03
1994.7	0.05 ± 0.02	0.043 ± 0.001	0.06 ± 0.02

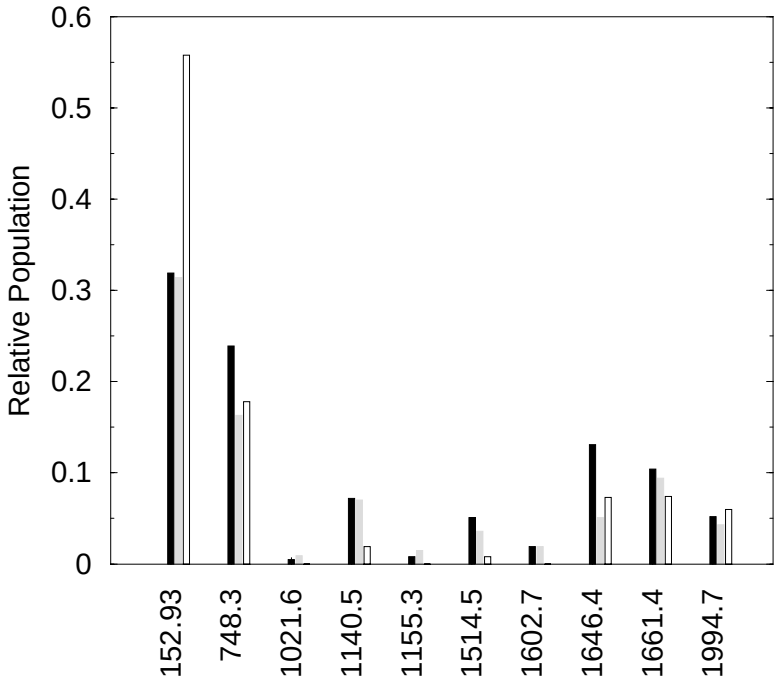

Figure 8.8: Relative population of low-lying levels by $\frac{1}{2}^-$ resonances: experimental unweighted (black), experimental weighted (gray) and DICEBOX GR model with temperature change model (white).

Table 8.10: Comparison of experimental relative populations with DICEBOX predictions (GR model with temperature change) for $\frac{3}{2}^-$ resonances.

E_{Level} (keV)	Unweighted Average	Weighted Average	DICEBOX Average
152.9	0.3 ± 0.2	0.307 ± 0.003	0.50 ± 0.07
748.3	0.17 ± 0.05	0.142 ± 0.001	0.16 ± 0.04
1021.6	0.03 ± 0.04	0.0010 ± 0.0001	< 0.0001
1140.5	0.12 ± 0.04	0.106 ± 0.001	0.10 ± 0.04
1155.3	0.04 ± 0.03	0.0090 ± 0.0002	0.0010 ± 0.0004
1514.5	0.07 ± 0.04	0.044 ± 0.001	0.05 ± 0.02
1602.7	0.03 ± 0.03	0.020 ± 0.001	< 0.0001
1646.4	0.07 ± 0.05	0.037 ± 0.002	0.06 ± 0.03
1661.4	0.10 ± 0.04	0.0750 ± 0.0009	0.06 ± 0.02
1994.7	0.07 ± 0.03	0.048 ± 0.002	0.04 ± 0.02

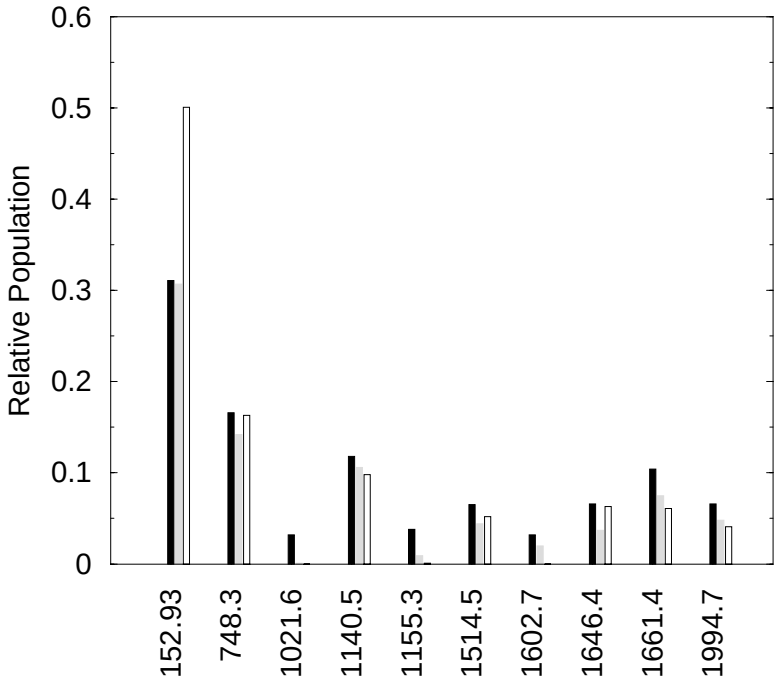

Figure 8.9: Relative population of low-lying levels by $\frac{3}{2}^-$ resonances: experimental unweighted (black), experimental weighted (gray) and DICEBOX GR model with temperature change (white).

8.2 Evaluation of Low Level Population Method

As discussed earlier the essence of the low level population method is that the low-lying states are populated differently by resonance states of different spins. This difference is expected to be enhanced by comparison of transitions from low-lying states with rather different spins. For example in Figure 8.10 the DICEBOX predictions for the relative population of the 152.9-keV, $3/2^-$ state and the 1994.7-keV, $3/2^+$ states are used to calculate the ratio of the intensities of the 152.9-keV transition to ground and the 1841-keV transition from the 1994.7-keV state to the 152.9-keV state. As expected there is very little difference in the predicted ratio for decay from $1/2^-$ and $3/2^-$ states. This is observed experimentally, as shown in Figure 8.11. A number of other comparisons that lead to similar results are shown in Appendix D.

Based on these simple arguments one expects a larger difference in the relative population of low-lying states with quite different spins. For example Figure 8.12 shows the predicted ratio for two transitions from the $1/2^+$ 1646.4-keV state and the $5/2^+$ 1140.5-keV state. The intensity of the 898.1-keV transition from the $1/2^+$ state to the $3/2^+$ state at 748.27 keV is compared with the intensity of the 1049.8-keV transition from the $5/2^+$ state to the $5/2^-$ state at 90.64 keV. The predicted ratios are shown in Figure 8.12. As expected the predicted ratio of these transitions is much larger for the decay from $1/2^-$ resonances than for $3/2^-$ resonances: the relative population of the $5/2^+$ state is much weaker from the lower spin resonance. This behavior is consistent for a variety of spin combinations. In fact it was earlier similar calculations that encouraged us to seriously consider this approach. However, the very large uncertainty in the population of the higher spin states ($5/2^+$ in this case) led to a large uncertainty in the predicted ratio for decay from the $1/2^-$ states. The experimental results shown in Figure 8.13 do not show this clear distinction between the resonance spins.

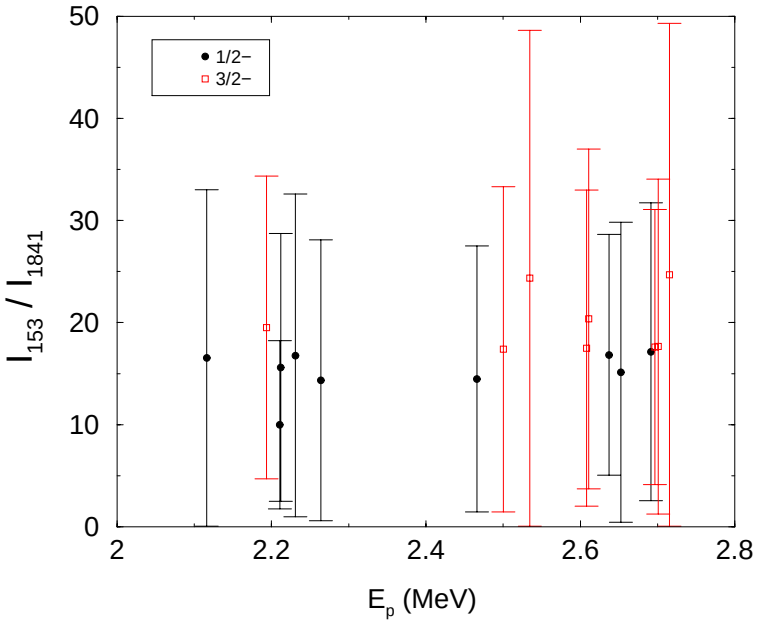

Figure 8.10: DICEBOX predictions for the ratio of the intensity of the 153–keV transition ($3/2^- \rightarrow 7/2^-$) to the intensity of the 1841–keV transition ($3/2^+ \rightarrow 3/2^-$).

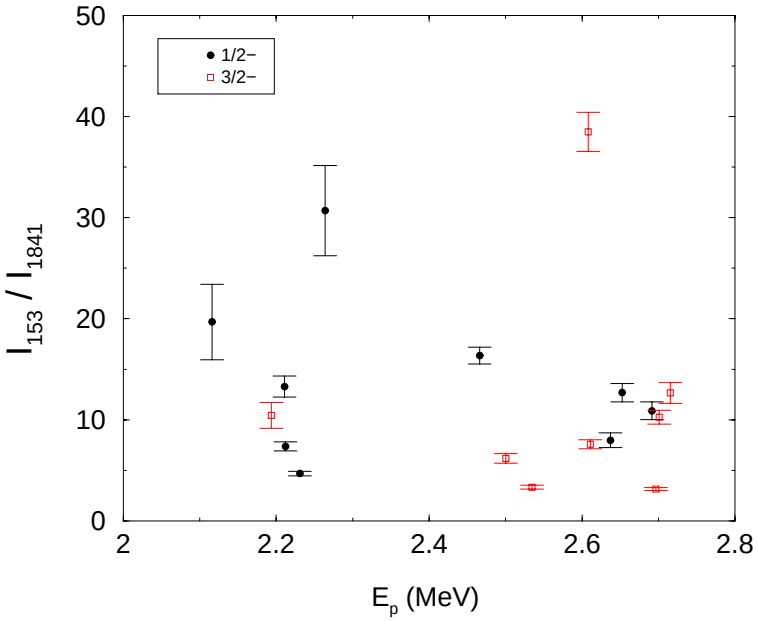

Figure 8.11: Experimental ratios of the intensity of the 153–keV transition ($3/2^- \rightarrow 7/2^-$) to the intensity of the 1841–keV transition ($3/2^+ \rightarrow 3/2^-$).

Similar results were obtained for all of the transitions studied. The DICEBOX predictions suggested that the low level population method might work in this nuclide, but experimentally the results were inconclusive at best. Typical results for a number of cases are shown in Appendix D. Experimentally the relative population of the low-lying states with higher spin is consistently larger than the DICEBOX predictions. This has the effect of minimizing the anticipated large differences in the ratios of radiative transitions from low-lying states with different spin. Thus the conclusion is that the simple model embodied in the DICEBOX simulation code works only qualitatively in ^{49}V. This is to be compared with the quantitative success of this approach in heavier nuclei such as silver.

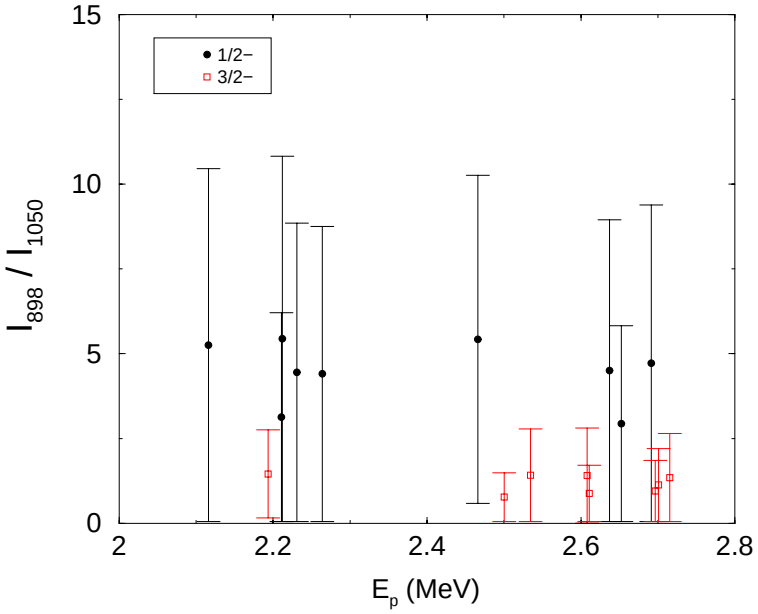

Figure 8.12: DICEBOX predictions for the ratio of the intensity of the 898–keV transition ($1/2^+ \rightarrow 3/2^+$) to the intensity of the 1050–keV transition ($5/2^+ \rightarrow 5/2^-$).

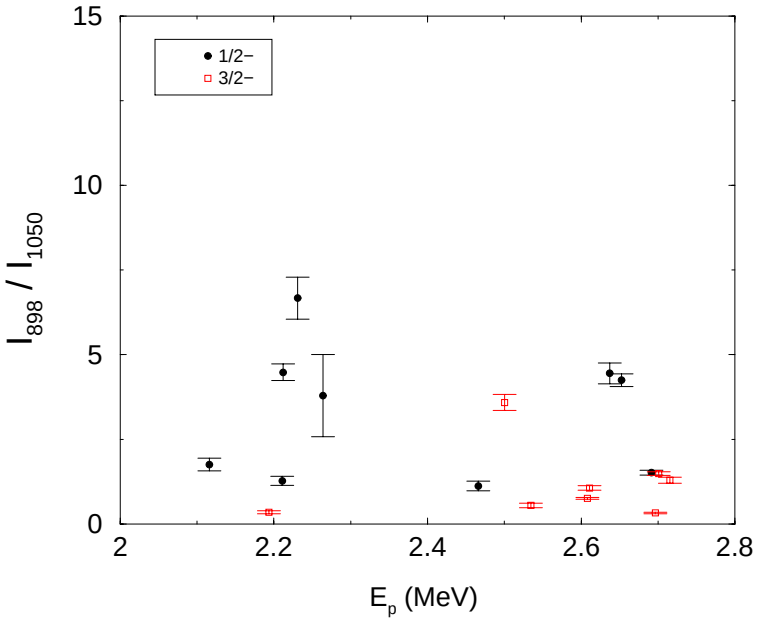

Figure 8.13: Experimental ratios of the intensity of the 898–keV transition ($1/2^+ \rightarrow 3/2^+$) to the intensity of the 1050–keV transition ($5/2^+ \rightarrow 5/2^-$).

Chapter 9

Summary and Conclusions

The primary goal of this experiment was to obtain detailed γ-ray spectra from a large number of compound nuclear (CN) resonances with known quantum numbers, and to compare this data set with statistical model predictions. The target nucleus ^{48}Ti was selected because our group had earlier determined the quantum numbers for a large number of resonances. The resonances selected for study were all s-wave ($1/2^+$) and p-wave ($1/2^-$ or $3/2^-$) states. Although a large number of resonances with higher spins were also available for study, their resonance parameters were more questionable.

Excitation curves for the elastic, inelastic and capture reactions were measured, and 27 resonances were selected for more extensive study. The primary elements in the selection process were (1) that the resonance have one of the three spin-parity combinations previously chosen, (2) that the spin-parity assignment be firm, and (3) that the resonance be relatively well isolated. This last requirement was very difficult to satisfy due to the high level density of CN resonances. Therefore when the capture spectrum was measured on the resonance in question, a corresponding off-resonance capture measurement was also performed. Usually data was obtained for the same integrated beam curent for the on- and off-resonance spectra; in favorable cases where the background was low, the off–resonance measurement was shorter than the on–resonance measurement.

Our focus was on the relative populations for the first 12 low-lying levels in ^{49}V. The intensities of all of the γ rays measured were combined with the previously measured branching ratios for the decay of these low-lying states to determine the relative populations of these states. Due to resolution issues, the decay from two of these states could not be determined; these states were excluded from further consideration. The relative populations of the remaining 10 levels were then normalized to one. These relative populations were compared with model calculations.

The program DICEBOX was used to perform the statistical model calculations. Since the level density parameters were considered relatively better determined, the focus was varying the model parameters for the radiative strength functions. Calculations were first performed with the standard current giant resonance models for the E1, M1, and E2 strength functions. Then single particle models were used for the M1 and E2 strength functions. The results were little changed. A final series of calculations was performed with a very large temperature to examine the effect of the temperature dependence of the E1 strength function. Again the effect on the relative population was minimal. Thus the conclusion is that the relative population of the low-lying levels is rather insensitive to changes in the radiative strength functions.

The comparison between the DICEBOX simulations and the experimental data yields very approximate agreement: states that are predicted to be strongly (weakly) populated are in every case observed to be strongly (weakly) populated experimentally. However, the experimental relative population of the weakly populated states is systematically larger that the model predictions. Whether the agreement between model and experiment can be improved by adjustment of the model parameters is an open question.

The low level population method worked very well in heavier nuclei in general and in particular for silver. DICEBOX simulations suggested that this method might be applicable in ^{49}V; for a number of ratios of γ-ray intensities a separation was indicated between the ^{49}V $3/2^-$ and $1/2^-$ values. However, in practice the method does not seem to work in the

present experimental data. At best the results are inconclusive. Since the goal was to find a definitive spin assignment (as was obtained by Zanini [Zan98]), the LLP method does not seem to apply in this nucleus.

The conclusion is that the extreme statistical model (as formulated in the DICEBOX simulations with standard radiative strength function models and standard level density formulations) works at best qualitatively in ^{49}V. The observed results are consistent with the view that both statistical and nuclear structure effects are required to provide a detailed description of radiative decay in this mass region.

Bibliography

[Axe62] P. Axel, "Electric Dipole Ground-State Transition Width Strength Function and 7-MeV Photon Interactions", Physical Review **126**, 671 (1962).

[Bec98] F. Becvar, "Simulation of γ Cascades in Complex Nuclei with Emphasis on Assessment of Uncertainties of Cascade-related Quantities", Nuclear Instruments and Methods in Physics Research **A417**, 434 (1998).

[Bet36] H. Bethe, "An Attempt to Calculate the Number of Energy Levels of a Heavy Nucleus", Physical Review **50**, 332 (1936).

[Bet37] H. Bethe, "Nuclear Physics B. Nuclear Dynamics, Theoretical", Reviews of Modern Physics **9**, 69 (1937).

[Bie60] L. C. Biedenharn, "Angular Correlations in Nuclear Spectroscopy", in *Nuclear Spectroscopy, Part B*, edited by F. Ajzenberg-Selove, pages 732–810, Academic Press, New York, 1960.

[Bla52] J. M. Blatt and L. C. Biedenharn, "The Angular Distribution of Scattering and Reaction Cross Sections", Reviews of Modern Physics **24**, 258 (1952).

[Bla92] J. M. Blatt and V. F. Weisskopf, *Theoretical Nuclear Physics*, Dover, New York, 1992.

[Boh36] N. Bohr, "Neutron Capture and Nuclear Constitution", Nature **137**, 344 (1936).

[Boh75] A. Bohr and B. R. Mottelson, *Nuclear Structure, Volume II*, W. A. Benjamin, Inc, Reading, Massachusetts, 1975.

[Bri55] D. M. Brink, Ph.D. thesis, Oxford University, 1955.

[Dov72] C. B. Dover and R. H. Lemmer, "Damping of Nuclear Dipole States", Annals of Physics **70**, 458 (1972).

[Dra60] J. E. Draper and T. E. Springer, "Multiplicity of Resonance Neutron Capture Gamma Rays", Nuclear Physics **16**, 27 (1960).

[Dra94] J. M. Drake, *Resonance Tests of Detailed Balance and Design of Compton Suppression Spectrometer*, Ph.D. thesis, North Carolina State University, 1994.

[End90] P. M. Endt, C. Alderliesten, F. Zijderhand, A. A. Wolters, and A. G. M. van Hees, "Spectroscopic Information on ^{24}Mg and ^{28}Si from Proton Capture", Nuclear Physics **A510**, 209 (1990).

[Fer34] E. Fermi, "Artificial Radioactivity Produced by Neutron Bombardment", Ricerca Scientifica **5**, 282 (1934).

[Fer65] A. J. Ferguson, *Angular Correlation Methods in Gamma-Ray Spectroscopy*, North-Holland, Amsterdam, 1965.

[Fir96] R. B. Firestone, V. S. Shirley, C. M. Baglin, S. Y. F. Chu, and J. Zipkin, *Table of Isotopes*, volume I & II, John Wiley & Sons, Inc., New York, 1996.

[Gil65] A. Gilbert and A. G. W. Cameron, "A Composite Nuclear-Level Density Formula with Shell Corrections", Canadian Journal of Physics **43**, 1446 (1965).

[Gun95] F. Gunsing, F. Corvi, H. Postma, and F. Bečvář, "The Simulation of Gamma Spectra of ^{113}Cd(n,γ) for Neutron Resonance Spin Assignment", Nuclear Instruments and Methods in Physics Research A **365**, 410 (1995).

[Gun97] F. Gunsing et al., "Spins of Resonances in Reactions of Neutrons with ^{238}U and ^{113}Cd", Physical Review C **56**, 1266 (1997).

[Hab99] M. K. Habior, "Statistical Decay of the Giant Dipole Resonance Excited by Complete Fusion Reactions and Other Sources of High-Energy γ-Rays in Heavy-Ion Collisions at 4-11 MeV/u", Acta Physica Polonica B **30**, 1353 (1999).

[Haf35] L. R. Hafsted and M. A. Tuve, "Carbon Radioactivity and Other Resonance Transmutations by Protons", Physical Review **48**, 306 (1935).

[Hub54] R. Huby, "Phase of Matrix Elements in Nuclear Reactions and Radioactive Decay", Proceedings of the Physical Society **67A**, 1103 (1954).

[Hui60] J. R. Huizenga and R. Vandenbosch, "Interpretation of Isomeric Cross-Section Ratios for (n,γ) and (γ,n) Reactions", Physical Review **120**, 1305 (1960).

[Hui72] J. R. Huizenga and L. G. Moretto, "Nuclear Level Densities", Annual Review of Nuclear Science **22**, 427 (1972).

[Ign75] A. V. Ignatyuk, G. N. Smirenkin, and A. S. Tishin, "Phenomenological Description of the Energy Dependence of Level Density Parameter", Soviet Journal of Physics **23**, 255 (1975).

[Kad83] S. G. Kadmenskii, V. P. Markushev, and V. I. Furman, "Radiative Widths of Neutron Resonances. Giant Dipole Resonances", Soviet Journal of Nuclear Physics **37**, 165 (1983).

[Kat78] S. K. Kataria, V. S. Ramamurthy, and S. S. Kapoor, "Semiempirical Nuclear Level Density Formula with Shell Effects", Physical Review C **18**, 549 (1978).

[Kno89] G. F. Knoll, *Radiation Detection and Measurement*, John Wiley & Sons, New York, 1989.

[Kop90] J. Kopecky and M. Uhl, "Test of Gamma-ray Strength Functions in Nuclear Reaction Model Calculations", Physical Review C **41**, 1941 (1990).

[Kra88] K. Krane, *Introductory Nuclear Physics*, John Wiley and Sons, New York, second edition, 1988.

[Krt02] M. Krticka, 2002, Personal Communication.

[Lan58] A. M. Lane and R. G. Thomas, "R-Matrix Theory of Nuclear Reactions", Reviews of Modern Physics **30**, 257 (1958).

[Lan93] G. H. Lang, C. W. Johnson, S. E. Koonin, and W. E. Ormand, "Monte Carlo Evaluation of Path Integrals for the Nuclear Shell Model", Physical Review C **48**, 1518 (1993).

[Low99] L. Y. Lowie, "Parity Violation in Neutron Resonances in ^{107,109}Ag", Physical Review C **59**, 1119 (1999).

[Mue50] C. O. Muehlhause, "Neutron Capture Gamma-Ray Multiplicity", Physical Review **79**, 277 (1950).

[Nak97] H. Nakada and Y. Alhassid, "Total and Parity-Projected Level Densities of Iron-Region Nuclei in the Auxilliary Fields Monte Carlo Shell Model", Physical Review Letters **79**, 2939 (1997).

[Nak98] H. Nakada and Y. Alhassid, "Microscopic Nuclear Level Densities from Fe to Ge by the Shell Model Monte Carlo Method", Physics Letters B **436**, 231 (1998).

[New56] T. D. Newton, "Shell Effects on the Spacing of Nuclear Levels", Canadian Journal of Physics **34**, 804 (1956).

[Nud03] 2003, National Nuclear Data Center, www.nndc.bnl.gov.

[Poe70] W. P. Poenitz and J. R. Tatarczuk, "Spin Determination of Resonances in ^{165}Ho From Low-Level Occupation Probability Ratios", Nuclear Physics **A151**, 569 (1970).

[Pro71] N. H. Prochnow, *A High Resolution Study of Proton Resonances in ^{47}V, ^{49}V, and ^{51}V*, Ph.D. thesis, Duke University, 1971.

[Rad89] D. Radford, *GELIFT Reference Manual*, Chalk River Nuclear Laboratories, Chalk River, Ontario KOJ 1PO, Canada, 1989.

[Ros67] H. J. Rose and D. M. Brink, "Angular Distributions of Gamma Rays in Terms of Phase-defined Reduced Matrix Elements", Reviews of Modern Physics **39**, 306 (1967).

[Sha54] W. T. Sharpe, *Table of Coefficients for Angular Distribution Analysis Technical Report CRT-556*, Atomic Energy of Canada Limited, 1954.

[Sod87] J. P. Soderstrum, M. A. Boyd, C. R. Gould, and N. R. Roberson, *XSYS Reference Manual*, Triangle Universities Nuclear Laboratory, Durham, NC, sixth edition, 1987.

[Vav96] G. A. Vavrina, *Resonance Spectroscopy of the $^{29}Si(p,\gamma)$ Reaction*, Ph.D. thesis, North Carolina State University, 1996.

[Vog59] E. Vogt, "Resonance Reactions, Theoretical", in *Nuclear Reactions, Volume 1*, edited by P. M. Endt and M. DeMeur, pages 215–258, North-Holland Publishing Company, Amsterdam, 1959.

[Wei51] V. F. Weisskopf, "Transition Probabilities in Nuclei", Physical Review **83**, 1073 (1951).

[Wel78] W. K. Wells, *High Resolution Proton Inelastic Scattering on ^{56}Fe and ^{48}Ti*, Ph.D. thesis, Duke University, 1978.

[Wes88] C. R. Westerfeldt, R. O. Nelson, E. G. Bilpuch, and G. E. Mitchell, "A Microcomputer-based System for Measuring Excitation Functions with Good Energy Resolution", Nuclear Instruments and Methods in Physics Research **A270**, 467 (1988).

[Wes95] C. R. Westerfeldt, J. F. Shriner, and G. A. Vavrina, *The TUNL High Resolution Laboratory System and Operating Procedures*, Triangle Universities Nuclear Laboratory, Durham NC third edition, 1995.

[Wet70] K. J. Wetzel and G. E. Thomas, "Method for Determining Spins of Neutron Resonances", Physical Review C **1**, 1501 (1970).

[Wig47] E. P. Wigner and L. Eisenbud, "Higher Angular Momenta and Long Range Interaction in Resonance Reactions", Physical Review **72**, 29 (1947).

[Wig57] E. P. Wigner, "Results and Theory of Resonance Absorption", in *Conference on Neutron Physics by Time–of–Flight*, page 59, Oak Ridge National Laboratory, Gatlinburg, TN, 1957.

[Zan98] L. Zanini, *Neutron Capture Gamma-Ray Spectroscopy with* ^{107}*Ag,* ^{109}*Ag and* ^{115}*In for Parity Violation and Nuclear Structure Studies*, Ph.D. thesis, Delft University of Technology, 1998.

Appendix A

γ-ray Intensities

This appendix contains listings of the γ–ray intensities for each of the 27 ^{49}V resonances studied. These intensities were used to calculate the relative populations of the low-lying levels. These intensities were also used to determine the ratios of the populations of low-lying states in order to test the LLP method. Table A.1 lists the γ rays emitted by the twelve ^{49}V levels studied. This table also lists the initial and final state energies, and the spin and parity of the initial and final states [Nud03].

Table A.2 lists the γ-ray intensities. The γ-ray intensity value "n/o" arises from different causes. The 62.3-keV γ ray was not detected; it fell below the hardware descriminator setting. The 987.61-keV γ ray could not be resolved from the dominant 984-keV γ ray originating from inelastic scattering to the first excited state of ^{48}Ti. The HPGe detector resolution was about 1.5 keV per channel. The 1490.24-keV γ ray could not be resolved from the 1493.6-keV γ ray. The 1512-keV γ ray could not be resolved from the 1514-keV γ ray. Consequently, both the 1512– and 1514–keV γ rays were not used to determine the populations for the levels that emit them. For all other γ-ray intensities listed as "n/o", the γ rays were either literally not observed or the background was higher than the measured γ-ray intensity.

Table A.1: Properties of low-lying initial and final states for γ-ray transitions.

E_γ (keV)	E_i (keV)	J_i^π	E_f (keV)	J_f^π	Fractional Branching Ratio
62.3	152.93	$\frac{3}{2}^-$	90.64	$\frac{5}{2}^-$	0.413
90.6	90.64	$\frac{5}{2}^-$	0.00	$\frac{7}{2}^-$	1.000
133.8	1155.32	$\frac{9}{2}^-$	1021.63	$\frac{11}{2}^-$	0.029
152.9	152.93	$\frac{3}{2}^-$	0.00	$\frac{7}{2}^-$	0.587
392.7	1140.53	$\frac{5}{2}^+$	748.27	$\frac{3}{2}^+$	0.056
447.4	1602.68	$\frac{7}{2}^+$	1155.32	$\frac{9}{2}^-$	0.00892
462.2	1602.68	$\frac{7}{2}^+$	1140.53	$\frac{5}{2}^+$	0.075
595.3	748.27	$\frac{3}{2}^+$	152.93	$\frac{3}{2}^-$	0.540
657.6	748.27	$\frac{3}{2}^+$	90.64	$\frac{5}{2}^-$	0.460
766.0	1514.54	$\frac{5}{2}^-$	748.27	$\frac{3}{2}^+$	0.172
854.5	1602.68	$\frac{7}{2}^+$	748.27	$\frac{3}{2}^+$	0.08361
854.5	1994.70	$\frac{3}{2}^+$	1140.53	$\frac{5}{2}^+$	0.2901
898.1	1646.43	$\frac{1}{2}^+$	748.27	$\frac{3}{2}^+$	0.465
912.3	1661.40	$\frac{3}{2}^-$	748.27	$\frac{3}{2}^+$	0.050
987.6	1140.53	$\frac{5}{2}^+$	152.93	$\frac{3}{2}^-$	0.168
1021.6	1021.62	$\frac{11}{2}^-$	0.00	$\frac{7}{2}^-$	1.000
1049.8	1140.53	$\frac{5}{2}^+$	90.64	$\frac{5}{2}^-$	0.239
1064.6	1155.32	$\frac{9}{2}^-$	90.64	$\frac{5}{2}^-$	0.224
1140.7	1140.53	$\frac{5}{2}^+$	0.00	$\frac{7}{2}^-$	0.536
1155.3	1155.32	$\frac{9}{2}^-$	0.00	$\frac{7}{2}^-$	0.747
1246.8	1994.70	$\frac{3}{2}^+$	748.27	$\frac{3}{2}^+$	0.157
1361.6	1514.54	$\frac{5}{2}^-$	152.93	$\frac{3}{2}^-$	0.464
1423.6	1514.54	$\frac{5}{2}^-$	90.64	$\frac{5}{2}^-$	0.094
1490.2	1643.19	$\frac{3}{2}^-$	152.93	$\frac{3}{2}^-$	0.977
1493.6	1646.43	$\frac{1}{2}^+$	152.93	$\frac{3}{2}^-$	0.535
1508.4	1661.40	$\frac{3}{2}^-$	152.93	$\frac{3}{2}^-$	0.340
1512.0	1602.68	$\frac{7}{2}^+$	90.64	$\frac{5}{2}^-$	0.557
1514.4	1514.54	$\frac{5}{2}^-$	0.00	$\frac{7}{2}^-$	0.269
1553.0	1643.19	$\frac{3}{2}^-$	90.64	$\frac{5}{2}^-$	0.023
1570.8	1661.40	$\frac{3}{2}^-$	90.64	$\frac{5}{2}^-$	0.520
1602.6	1602.68	$\frac{7}{2}^+$	0.00	$\frac{7}{2}^-$	0.275
1661.4	1661.40	$\frac{3}{2}^-$	0.00	$\frac{7}{2}^-$	0.090
1841.0	1994.70	$\frac{3}{2}^+$	152.93	$\frac{3}{2}^-$	0.341
1903.4	1994.70	$\frac{3}{2}^+$	90.64	$\frac{5}{2}^-$	0.212

Table A.2: γ-decay intensities for ^{49}V resonances

E_p, J^π (MeV) / E_γ (keV)	2.0615, $\frac{1}{2}^+$ Intensity	2.1163, $\frac{1}{2}^-$ Intensity	2.1936, $\frac{3}{2}^-$ Intensity	2.2045, $\frac{1}{2}^+$ Intensity
62.3	n/o	n/o	n/o	n/o
90.6	n/o	n/o	n/o	n/o
133.8	n/o	n/o	n/o	n/o
152.9	12246 ± 695	13439 ± 1063	13456 ± 851	48384 ± 1267
392.7	394 ± 79	1465 ± 150	1101 ± 103	2062 ± 167
447.4	n/o	n/o	n/o	n/o
462.2	n/o	300 ± 139	353 ± 129	647 ± 146
595.3	6234 ± 201	11825 ± 311	6953 ± 239	15307 ± 351
657.6	4676 ± 184	9654 ± 275	5918 ± 227	13644 ± 321
766.0	n/o	n/o	n/o	n/o
854.5	922 ± 85	704 ± 97	1692 ± 162	9864 ± 270
898.1	1814 ± 106	3036 ± 158	998 ± 117	1765 ± 152
912.3	331 ± 170	n/o	263 ± 163	n/o
987.6	n/o	n/o	n/o	n/o
1021.6	n/o	386 ± 67	2330 ± 108	n/o
1049.8	1366 ± 117	1734 ± 162	2893 ± 153	6296 ± 219
1064.6	176 ± 62	34 ± 98	1408 ± 109	n/o
1140.7	2434 ± 143	2937 ± 170	5355 ± 180	11315 ± 284
1155.3	91 ± 89	586 ± 94	4857 ± 167	573 ± 109
1246.8	345 ± 69	2665 ± 141	680 ± 88	1358 ± 133
1361.6	920 ± 123	1892 ± 150	3798 ± 169	3180 ± 159
1423.6	545 ± 758	534 ± 71	826 ± 111	899 ± 135
1490.2	n/o	n/o	n/o	n/o
1493.6	n/o	n/o	n/o	n/o
1508.4	7533 ± 259	2657 ± 198	3348 ± 161	7720 ± 241
1512.0	n/o	n/o	n/o	n/o
1514.4	n/o	n/o	n/o	n/o
1553.0	n/o	n/o	n/o	n/o
1570.8	14506 ± 298	4056 ± 185	3483 ± 157	10177 ± 266
1602.6	1007 ± 75	486 ± 65	670 ± 95	882 ± 135
1661.4	140 ± 91	185 ± 107	28 ± 104	416 ± 185
1841.0	881 ± 84	683 ± 118	1289 ± 135	8731 ± 260
1903.4	418 ± 63	388 ± 90	751 ± 104	5899 ± 216

Table A.2 *(continued)*

E_p, J^π (MeV) / E_γ (keV)	2.2108, $\frac{1}{2}^-$ Intensity	2.2121, $\frac{1}{2}^-$ Intensity	2.2308, $\frac{1}{2}^-$ Intensity	2.2638, $\frac{1}{2}^-$ Intensity
62.3	n/o	n/o	n/o	n/o
90.6	n/o	n/o	n/o	n/o
133.8	n/o	n/o	n/o	n/o
152.9	22701 ± 929	27293 ± 978	30147 ± 998	28057 ± 1278
392.7	1057 ± 313	830 ± 138	1799 ± 174	149 ± 385
462.2	n/o	n/o	215 ± 154	336 ± 268
595.3	9065 ± 265	27798 ± 474	22204 ± 411	34435 ± 584
657.6	8278 ± 244	23312 ± 416	18119 ± 364	29264 ± 512
766.0	n/o	252 ± 135	n/o	n/o
854.5	2156 ± 141	4127 ± 136	7203 ± 176	1327 ± 152
898.1	2122 ± 110	12413 ± 265	25541 ± 433	1739 ± 150
912.3	n/o	208 ± 163	39 ± 145	n/o
987.6	n/o	n/o	n/o	n/o
1021.6	n/o	n/o	n/o	n/o
1049.8	1669 ± 153	2770 ± 138	3828 ± 349	459 ± 142
1064.6	n/o	n/o	n/o	n/o
1140.7	2772 ± 174	4821 ± 204	7300 ± 246	937 ± 189
1155.3	n/o	n/o	n/o	n/o
1246.8	n/o	685 ± 92	984 ± 115	396 ± 90
1361.6	2902 ± 158	1019 ± 137	2865 ± 165	n/o
1423.6	656 ± 78	n/o	571 ± 104	n/o
1490.2	n/o	n/o	n/o	n/o
1493.6	n/o	n/o	n/o	n/o
1508.4	3355 ± 175	5030 ± 194	5558 ± 177	1230 ± 170
1512.0	n/o	n/o	n/o	n/o
1514.4	n/o	n/o	n/o	n/o
1553.0	n/o	n/o	n/o	n/o
1570.8	6690 ± 202	8569 ± 228	11415 ± 254	3197 ± 203
1602.6	n/o	n/o	n/o	n/o
1661.4	61 ± 112	n/o	41 ± 114	n/o
1841.0	1709 ± 114	3710 ± 184	6445 ± 219	914 ± 126
1903.4	1392 ± 91	2162 ± 141	3947 ± 174	1141 ± 99

Table A.2 *(continued)*

E_p, J^π (MeV) / E_γ (keV)	2.2885, $\frac{1}{2}^+$ Intensity	2.3182, $\frac{1}{2}^+$ Intensity	2.4660, $\frac{1}{2}^-$ Intensity	2.5004, $\frac{3}{2}^-$ Intensity
62.3	n/o	n/o	n/o	n/o
90.6	n/o	n/o	n/o	n/o
133.8	n/o	n/o	n/o	n/o
152.9	43556 ± 1223	28105 ± 1289	53835 ± 1438	24038 ± 1218
392.7	966 ± 159	1554 ± 180	960 ± 180	1359 ± 320
447.4	n/o	n/o	n/o	n/o
462.2	n/o	n/o	n/o	n/o
595.3	25182 ± 453	15272 ± 408	6114 ± 415	20479 ± 517
657.6	21072 ± 390	13313 ± 353	5203 ± 248	17967 ± 429
766.0	n/o	1009 ± 237	n/o	n/o
854.5	5037 ± 164	2352 ± 177	2927 ± 140	4710 ± 206
898.1	5202 ± 179	15969 ± 353	2329 ± 185	10633 ± 264
912.3	1720 ± 122	n/o	3178 ± 169	406 ± 182
987.6	n/o	n/o	n/o	n/o
1021.6	n/o	n/o	1396 ± 175	8439 ± 249
1049.8	3422 ± 173	2561 ± 247	2079 ± 215	2963 ± 182
1064.6	440 ± 108	n/o	47 ± 138	1134 ± 105
1140.7	5574 ± 222	4807 ± 282	3089 ± 241	5481 ± 266
1155.3	357 ± 116	n/o	2059 ± 135	2270 ± 180
1246.8	1197 ± 117	1971 ± 160	n/o	528 ± 161
1361.6	1417 ± 154	1158 ± 301	7644 ± 289	1563 ± 218
1490.2	n/o	n/o	n/o	n/o
1493.6	n/o	n/o	n/o	n/o
1508.4	5171 ± 258	10677 ± 320	8267 ± 236	4605 ± 314
1512.0	n/o	n/o	n/o	n/o
1514.4	n/o	n/o	n/o	n/o
1553.0	n/o	n/o	n/o	n/o
1570.8	7296 ± 205	21511 ± 436	15301 ± 325	7187 ± 289
1602.6	1537 ± 145	578 ± 102	194 ± 152	593 ± 140
1661.4	n/o	n/o	71 ± 185	979 ± 118
1841.0	4289 ± 195	2208 ± 192	3293 ± 143	3896 ± 231
1903.4	2555 ± 155	1649 ± 151	1755 ± 119	2247 ± 171

Table A.2 *(continued)*

E_p, J^π (MeV) / E_γ (keV)	2.5207, $\frac{1}{2}^+$ Intensity	2.5344, $\frac{3}{2}^-$ Intensity	2.5419, $\frac{1}{2}^+$ Intensity	2.5575, $\frac{1}{2}^+$ Intensity
62.3	n/o	n/o	n/o	n/o
90.6	n/o	n/o	n/o	n/o
133.8	n/o	n/o	n/o	n/o
152.9	56345 ± 1667	19072 ± 903	47109 ± 1479	46742 ± 1480
392.7	5409 ± 340	1498 ± 247	3122 ± 353	4142 ± 226
447.4	n/o	n/o	n/o	900 ± 146
462.2	n/o	961 ± 287	897 ± 325	5208 ± 183
595.3	42470 ± 754	6217 ± 602	22088 ± 587	44007 ± 685
657.6	37358 ± 613	13208 ± 358	20972 ± 468	36081 ± 591
766.0	n/o	n/o	n/o	n/o
854.5	8607 ± 249	6969 ± 323	5529 ± 202	12056 ± 322
898.1	13414 ± 377	1708 ± 170	20166 ± 389	3807 ± 211
912.3	174 ± 270	n/o	n/o	394 ± 223
987.6	n/o	n/o	n/o	n/o
1021.6	118 ± 183	13706 ± 340	4551 ± 172	3841 ± 193
1049.8	10592 ± 284	3136 ± 241	5287 ± 235	11356 ± 259
1064.6	1036 ± 177	2557 ± 122	1482 ± 141	5608 ± 182
1140.7	17743 ± 414	8402 ± 291	8568 ± 310	19615 ± 373
1155.3	3945 ± 215	6545 ± 291	3899 ± 219	16463 ± 334
1246.8	6431 ± 255	745 ± 108	2141 ± 194	2416 ± 143
1361.6	12957 ± 351	4132 ± 283	4667 ± 319	11348 ± 306
1423.6	2948 ± 252	1291 ± 159	1357 ± 204	2726 ± 193
1490.2	n/o	n/o	n/o	n/o
1493.6	n/o	n/o	n/o	n/o
1508.4	14918 ± 382	8282 ± 347	7942 ± 389	32867 ± 639
1512.0	n/o	n/o	n/o	n/o
1514.4	n/o	n/o	n/o	n/o
1553.0	n/o	n/o	n/o	n/o
1570.8	22360 ± 422	10001 ± 275	8761 ± 289	28985 ± 484
1602.6	2704 ± 206	1183 ± 269	2083 ± 178	12031 ± 333
1661.4	827 ± 183	614 ± 157	708 ± 185	1395 ± 153
1841.0	6797 ± 261	5722 ± 222	2853 ± 254	6073 ± 244
1903.4	4695 ± 197	3428 ± 152	2430 ± 160	4203 ± 207

Table A.2 *(continued)*

E_p, J^π (MeV) / E_γ (keV)	2.6081, $\frac{3}{2}^-$ Intensity	2.6107, $\frac{3}{2}^-$ Intensity	2.6180, $\frac{1}{2}^+$ Intensity	2.6371, $\frac{1}{2}^-$ Intensity
62.3	n/o	n/o	n/o	n/o
90.6	n/o	n/o	n/o	n/o
133.8	n/o	n/o	n/o	n/o
152.9	597543 ± 17159	38049 ± 1379	56972 ± 1714	20250 ± 1068
392.7	16771 ± 711	3029 ± 314	7143 ± 303	1450 ± 296
447.4	n/o	n/o	n/o	n/o
462.2	1889 ± 530	n/o	2760 ± 228	n/o
595.3	72630 ± 1461	26209 ± 628	88181 ± 1170	14113 ± 744
657.6	57837 ± 1196	24148 ± 520	73598 ± 1010	13573 ± 606
766.0	n/o	n/o	n/o	n/o
854.5	16209 ± 562	8581 ± 556	26009 ± 475	4871 ± 698
898.1	20370 ± 579	7000 ± 324	4200 ± 167	15049 ± 432
912.3	4344 ± 456	n/o	384 ± 247	694 ± 472
987.6	n/o	n/o	n/o	n/o
1021.6	982 ± 120	1306 ± 143	2462 ± 197	2477 ± 278
1049.8	27112 ± 642	6596 ± 255	17052 ± 323	3384 ± 214
1064.6	1242 ± 124	1285 ± 137	2493 ± 126	n/o
1140.7	49890 ± 1059	11466 ± 334	28684 ± 522	5119 ± 281
1155.3	5925 ± 315	2440 ± 234	7404 ± 190	1627 ± 397
1246.8	17805 ± 578	2016 ± 140	7305 ± 238	577 ± 148
1361.6	20112 ± 592	5577 ± 245	11372 ± 323	5037 ± 308
1423.6	4870 ± 440	1284 ± 161	2544 ± 193	1400 ± 175
1490.2	n/o	n/o	n/o	n/o
1493.6	n/o	n/o	n/o	n/o
1508.4	14181 ± 356	12101 ± 348	18241 ± 518	4919 ± 369
1512.0	n/o	n/o	n/o	n/o
1514.4	n/o	n/o	n/o	n/o
1553.0	n/o	n/o	n/o	n/o
1570.8	44617 ± 971	20286 ± 400	10685 ± 314	7953 ± 232
1602.6	5215 ± 447	1607 ± 160	7123 ± 255	922 ± 122
1661.4	533 ± 170	n/o	n/o	n/o
1841.0	15518 ± 637	5026 ± 226	20083 ± 438	2540 ± 189
1903.4	9675 ± 456	2743 ± 155	13042 ± 322	1313 ± 124

Table A.2 *(continued)*

E_p, J^π (MeV) / E_γ (keV)	2.6525, $\frac{1}{2}^-$ Intensity	2.6915, $\frac{1}{2}^-$ Intensity	2.6964, $\frac{3}{2}^-$ Intensity	2.7007, $\frac{3}{2}^-$ Intensity
62.3	n/o	n/o	n/o	n/o
90.6	n/o	n/o	n/o	n/o
133.8	n/o	n/o	n/o	n/o
152.9	36385 ± 1572	37167 ± 1332	36379 ± 1307	35401 ± 1107
392.7	2488 ± 260	4006 ± 366	4209 ± 396	3410 ± 333
447.4	n/o	n/o	n/o	n/o
462.2	n/o	n/o	n/o	3704 ± 300
595.3	24444 ± 742	31787 ± 827	17328 ± 900	27008 ± 748
657.6	25626 ± 555	28327 ± 604	16424 ± 516	27024 ± 513
766.0	n/o	n/o	n/o	n/o
854.5	3897 ± 239	5646 ± 504	13047 ± 399	4765 ± 239
898.1	28366 ± 501	12518 ± 425	3630 ± 239	14720 ± 412
912.3	n/o	n/o	n/o	n/o
987.6	n/o	n/o	n/o	n/o
1021.6	n/o	3365 ± 254	1581 ± 177	20256 ± 416
1049.8	6681 ± 271	8259 ± 256	11175 ± 324	9888 ± 226
1064.6	n/o	2024 ± 127	1544 ± 133	6310 ± 182
1140.7	8875 ± 395	13398 ± 344	20445 ± 422	17546 ± 384
1155.3	431 ± 305	6376 ± 291	3910 ± 245	16646 ± 418
1246.8	873 ± 150	3334 ± 163	3164 ± 173	1857 ± 160
1361.6	5637 ± 345	7367 ± 286	6063 ± 364	8445 ± 318
1423.6	1728 ± 220	1579 ± 161	1506 ± 168	1704 ± 169
1490.2	n/o	n/o	n/o	n/o
1493.6	n/o	n/o	n/o	n/o
1508.4	13499 ± 407	9968 ± 350	8439 ± 276	18338 ± 487
1512.0	n/o	n/o	n/o	n/o
1514.4	n/o	n/o	n/o	n/o
1553.0	n/o	n/o	n/o	n/o
1570.8	24085 ± 484	13294 ± 336	13070 ± 290	13607 ± 297
1602.6	984 ± 155	2267 ± 154	1480 ± 128	6633 ± 201
1661.4	373 ± 124	921 ± 155	n/o	634 ± 132
1841.0	2869 ± 166	3413 ± 244	11581 ± 318	3451 ± 204
1903.4	1657 ± 132	2536 ± 142	7409 ± 226	1657 ± 140

Table A.2 *(continued)*

E_p, J^π (MeV) / E_γ (keV)	2.7102, $\frac{1}{2}^+$ Intensity	2.7131, $\frac{1}{2}^+$ Intensity	2.7153, $\frac{3}{2}^-$ Intensity
62.3	n/o	n/o	n/o
90.6	n/o	n/o	n/o
133.8	n/o	n/o	n/o
152.9	62704 ± 1717	22339 ± 1866	37322 ± 1531
392.7	2442 ± 397	785 ± 615	3924 ± 361
447.4	n/o	n/o	n/o
462.2	n/o	1840 ± 218	n/o
595.3	32775 ± 891	3693 ± 704	17480 ± 757
657.6	34350 ± 639	13092 ± 413	16956 ± 606
766.0	n/o	n/o	n/o
854.5	8087 ± 330	3435 ± 777	6830 ± 693
898.1	13769 ± 426	6 ± 413	10342 ± 528
912.3	n/o	n/o	147 ± 449
987.6	n/o	n/o	n/o
1021.6	n/o	n/o	502 ± 290
1049.8	6366 ± 281	2618 ± 377	8016 ± 359
1064.6	n/o	930 ± 263	1259 ± 145
1140.7	7651 ± 379	4919 ± 452	11625 ± 431
1155.3	n/o	3479 ± 363	1823 ± 282
1246.8	1815 ± 176	2034 ± 182	3697 ± 201
1361.6	2835 ± 316	4982 ± 386	12339 ± 399
1423.6	n/o	1945 ± 246	3404 ± 302
1490.2	n/o	n/o	n/o
1493.6	n/o	n/o	n/o
1508.4	5997 ± 333	15800 ± 486	7456 ± 386
1512.0	n/o	n/o	n/o
1514.4	n/o	n/o	n/o
1553.0	n/o	n/o	n/o
1570.8	13277 ± 409	23301 ± 642	12222 ± 403
1602.6	n/o	4358 ± 236	698 ± 214
1661.4	n/o	n/o	n/o
1841.0	7652 ± 269	2596 ± 283	2950 ± 206
1903.4	4990 ± 182	1728 ± 216	1911 ± 138

Appendix B

Experimental Relative Populations

This appendix presents the experimental relative population of low-lying states for each of the 27 ^{49}V resonances studied. This information is presented as tables of the relative populations in tables B.1 to B.6. Figures B.1 to B.9 present this information in graphical form. Appendix A contains the intensity for the 33 γ rays used to determine the relative populations. Some of the relative population values were < 0.0001 and are designated as such.

Table B.1: Relative population of low-lying levels by the 2.0615, 2.2045, 2.5207, 2.5419 and 2.5575 MeV $\frac{1}{2}^+$ resonances.

E_{Level} (keV)	2.0615 MeV	2.2045 MeV	2.5207 MeV	2.5419 MeV	2.5575 MeV
152.9	0.29 ± 0.01	0.427 ± 0.009	0.272 ± 0.008	0.33 ± 0.01	0.202 ± 0.006
748.3	0.151 ± 0.005	0.150 ± 0.003	0.227 ± 0.004	0.176 ± 0.005	0.203 ± 0.003
1021.6	< 0.0001	< 0.0001	0.0003 ± 0.0005	0.0186 ± 0.0008	0.0097 ± 0.0005
1140.5	0.070 ± 0.004	0.123 ± 0.003	0.115 ± 0.003	0.083 ± 0.003	0.107 ± 0.002
1155.3	0.004 ± 0.002	0.0040 ± 0.0008	0.0146 ± 0.0008	0.023 ± 0.001	0.058 ± 0.001
1514.5	0.04 ± 0.02	0.038 ± 0.003	0.081 ± 0.005	0.044 ± 0.004	0.064 ± 0.004
1602.7	0.051 ± 0.005	0.023 ± 0.003	0.028 ± 0.003	0.035 ± 0.005	0.128 ± 0.007
1646.4	0.054 ± 0.006	0.020 ± 0.003	0.082 ± 0.008	0.18 ± 0.01	0.021 ± 0.002
1661.4	0.31 ± 0.01	0.100 ± 0.003	0.109 ± 0.002	0.075 ± 0.003	0.162 ± 0.003
1994.7	0.032 ± 0.003	0.117 ± 0.008	0.072 ± 0.005	0.043 ± 0.004	0.045 ± 0.003

Table B.2: Relative population of low-lying levels by the 2.2885, 2.3182, 2.6180, 2.7102 and 2.7131 MeV $\frac{1}{2}^+$ resonances.

E_{Level} (keV)	2.2885 MeV	2.3182 MeV	2.6180 MeV	2.7102 MeV	2.7131 MeV
152.9	0.412 ± 0.009	0.28 ± 0.01	0.200 ± 0.006	0.39 ± 0.01	0.25 ± 0.02
748.3	0.257 ± 0.005	0.166 ± 0.005	0.333 ± 0.005	0.247 ± 0.006	0.109 ± 0.006
1021.6	< 0.0001	< 0.0001	0.0051 ± 0.0004	< 0.0001	< 0.0001
1140.5	0.067 ± 0.002	0.062 ± 0.003	0.131 ± 0.003	0.073 ± 0.003	0.065 ± 0.007
1155.3	0.0046 ± 0.0009	< 0.0001	0.0210 ± 0.0006	< 0.0001	0.030 ± 0.003
1514.5	0.017 ± 0.002	0.020 ± 0.004	0.051 ± 0.003	0.022 ± 0.003	0.081 ± 0.007
1602.7	0.031 ± 0.003	0.012 ± 0.002	0.058 ± 0.004	< 0.0001	0.115 ± 0.008
1646.4	0.062 ± 0.006	0.20 ± 0.02	0.019 ± 0.002	0.11 ± 0.01	< 0.0001
1661.4	0.087 ± 0.003	0.217 ± 0.007	0.066 ± 0.002	0.082 ± 0.003	0.30 ± 0.01
1994.7	0.063 ± 0.005	0.048 ± 0.004	0.117 ± 0.008	0.075 ± 0.006	0.058 ± 0.006

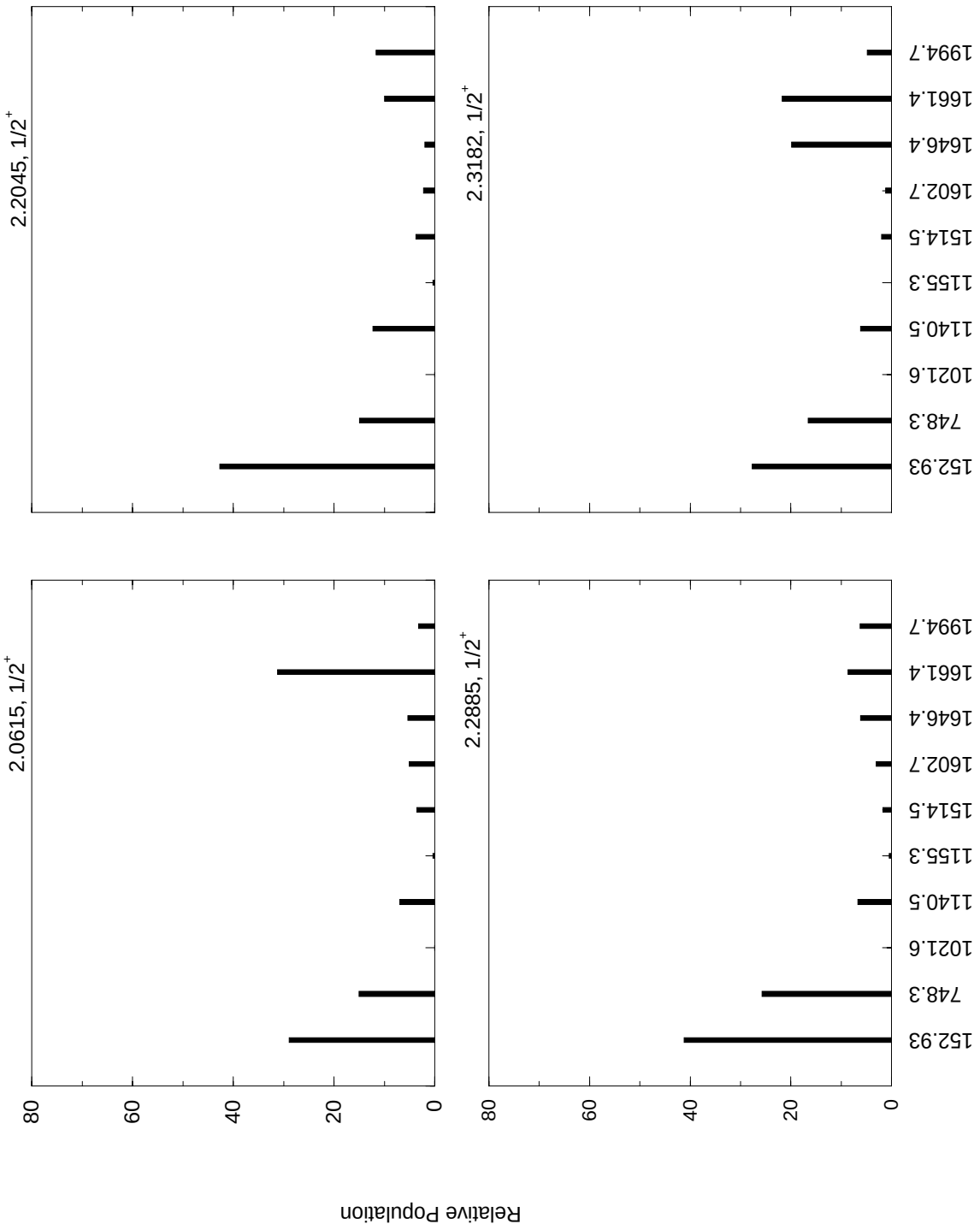

Figure B.1: Relative population of low-lying levels by the 2.0615, 2.2045, 2.2885 and 2.3182 MeV $\frac{1}{2}^+$ resonances.

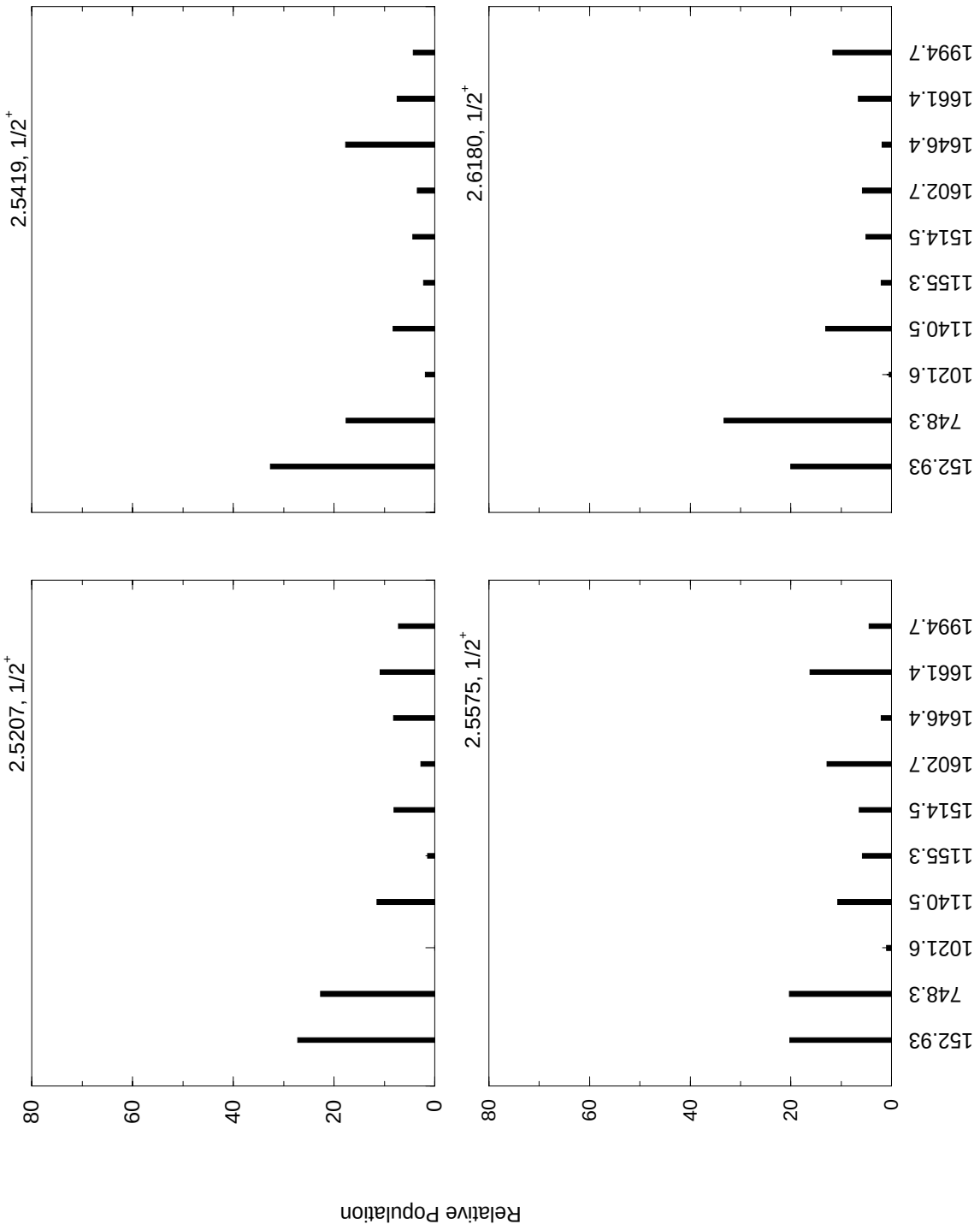

Figure B.2: Relative population of low-lying levels by the 2.0615, 2.2045, 2.2885 and 2.3182 MeV $\frac{1}{2}^+$ resonances.

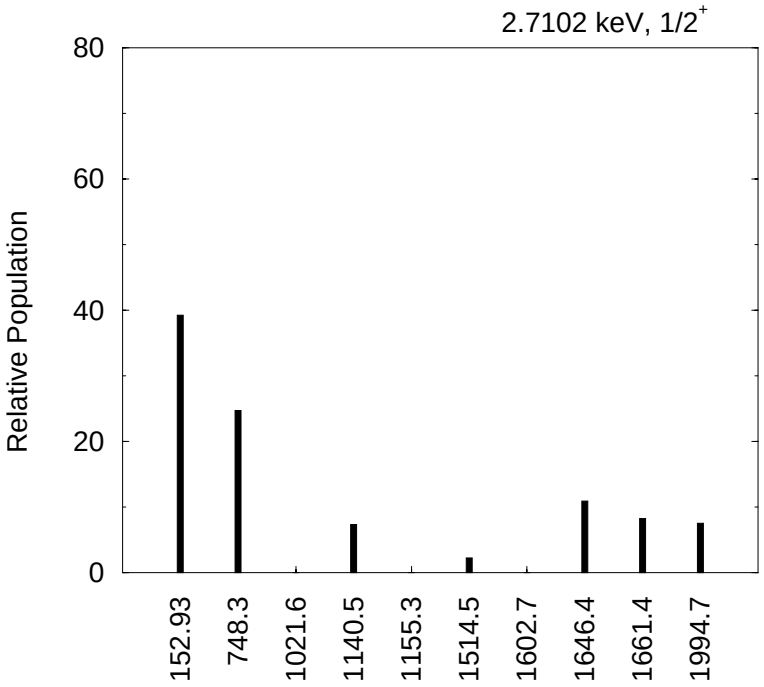

Figure B.3: Relative population of low-lying levels by the 2.7102 MeV $\frac{1}{2}^+$ resonance.

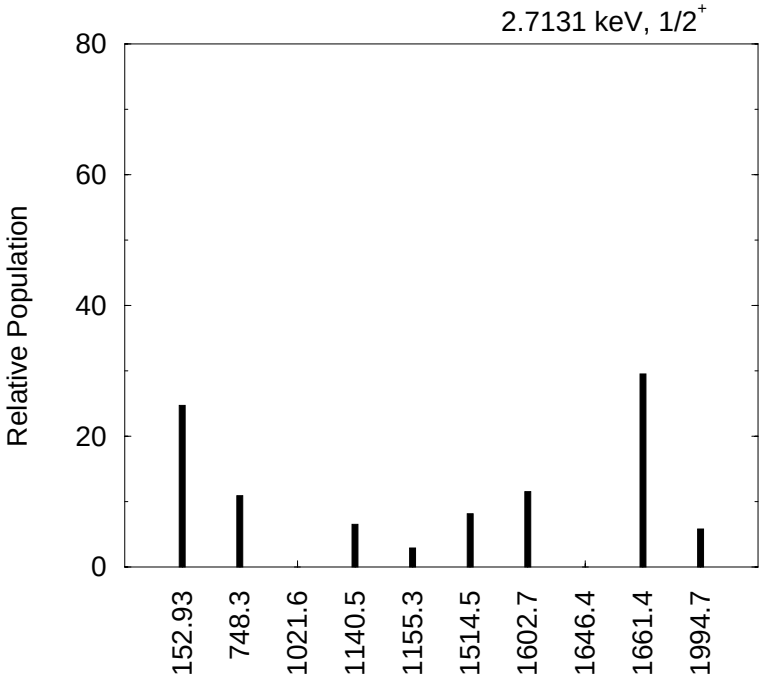

Figure B.4: Relative population of low-lying levels by the 2.7131 MeV $\frac{1}{2}^+$ resonance.

Table B.3: Relative population of low-lying levels by the 2.1163, 2.2108, 2.2121, 2.2308 and 2.2638 MeV $\frac{1}{2}^-$ resonances.

E_{Level} (keV)	2.1163 MeV	2.2108 MeV	2.2121 MeV	2.2308 MeV	2.2638 MeV
152.9	0.29 ± 0.02	0.43 ± 0.01	0.29 ± 0.01	0.25 ± 0.01	0.37 ± 0.02
748.3	0.274 ± 0.009	0.193 ± 0.005	0.318 ± 0.007	0.193 ± 0.007	0.49 ± 0.02
1021.6	0.0049 ± 0.0009	< 0.0001	< 0.0001	< 0.0001	< 0.0001
1140.5	0.094 ± 0.005	0.074 ± 0.005	0.063 ± 0.003	0.074 ± 0.004	0.014 ± 0.004
1155.3	0.008 ± 0.002	< 0.0001	< 0.0001	< 0.0001	< 0.0001
1514.5	0.055 ± 0.005	0.071 ± 0.005	0.012 ± 0.002	0.029 ± 0.002	< 0.0001
1602.7	0.029 ± 0.006	< 0.0001	< 0.0001	0.04 ± 0.02	0.03 ± 0.03
1646.4	0.083 ± 0.009	0.051 ± 0.006	0.17 ± 0.01	0.26 ± 0.02	0.029 ± 0.004
1661.4	0.093 ± 0.005	0.118 ± 0.004	0.094 ± 0.003	0.082 ± 0.003	0.040 ± 0.003
1994.7	0.067 ± 0.006	0.062 ± 0.005	0.057 ± 0.005	0.077 ± 0.006	0.027 ± 0.003

Table B.4: Relative population of low-lying levels by the 2.4660, 2.6371, 2.6525 and 2.6915 MeV $\frac{1}{2}^-$ resonances.

E_{Level} (keV)	2.4660 MeV	2.6371 MeV	2.6525 MeV	2.6915 MeV
152.9	0.53 ± 0.01	0.23 ± 0.01	0.24 ± 0.01	0.247 ± 0.008
748.3	0.065 ± 0.003	0.188 ± 0.008	0.193 ± 0.006	0.235 ± 0.005
1021.6	0.008 ± 0.001	0.017 ± 0.002	< 0.0001	0.013 ± 0.001
1140.5	0.043 ± 0.003	0.081 ± 0.004	0.084 ± 0.003	0.121 ± 0.003
1155.3	0.013 ± 0.001	0.015 ± 0.004	0.002 ± 0.002	0.034 ± 0.001
1514.5	0.100 ± 0.006	0.078 ± 0.006	0.051 ± 0.004	0.063 ± 0.004
1602.7	0.004 ± 0.003	0.023 ± 0.003	0.014 ± 0.002	0.032 ± 0.003
1646.4	0.029 ± 0.004	0.22 ± 0.02	0.23 ± 0.02	0.11 ± 0.01
1661.4	0.155 ± 0.004	0.101 ± 0.005	0.154 ± 0.005	0.099 ± 0.003
1994.7	0.053 ± 0.004	0.042 ± 0.004	0.029 ± 0.003	0.051 ± 0.004

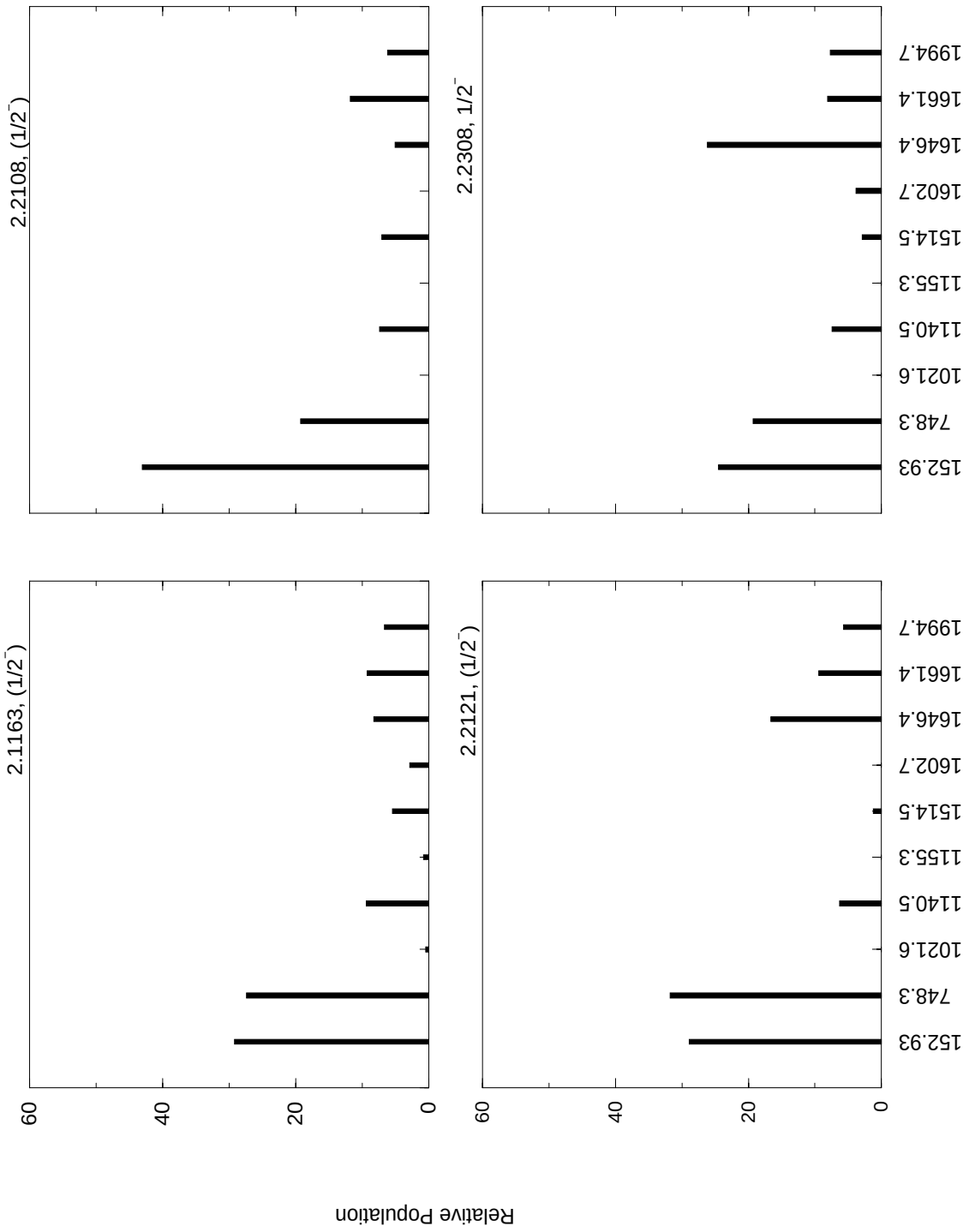

Figure B.5: Relative population of low-lying levels by the 2.1163, 2.2108, 2.2121 and 2.2308 MeV $\frac{1}{2}^-$ resonances.

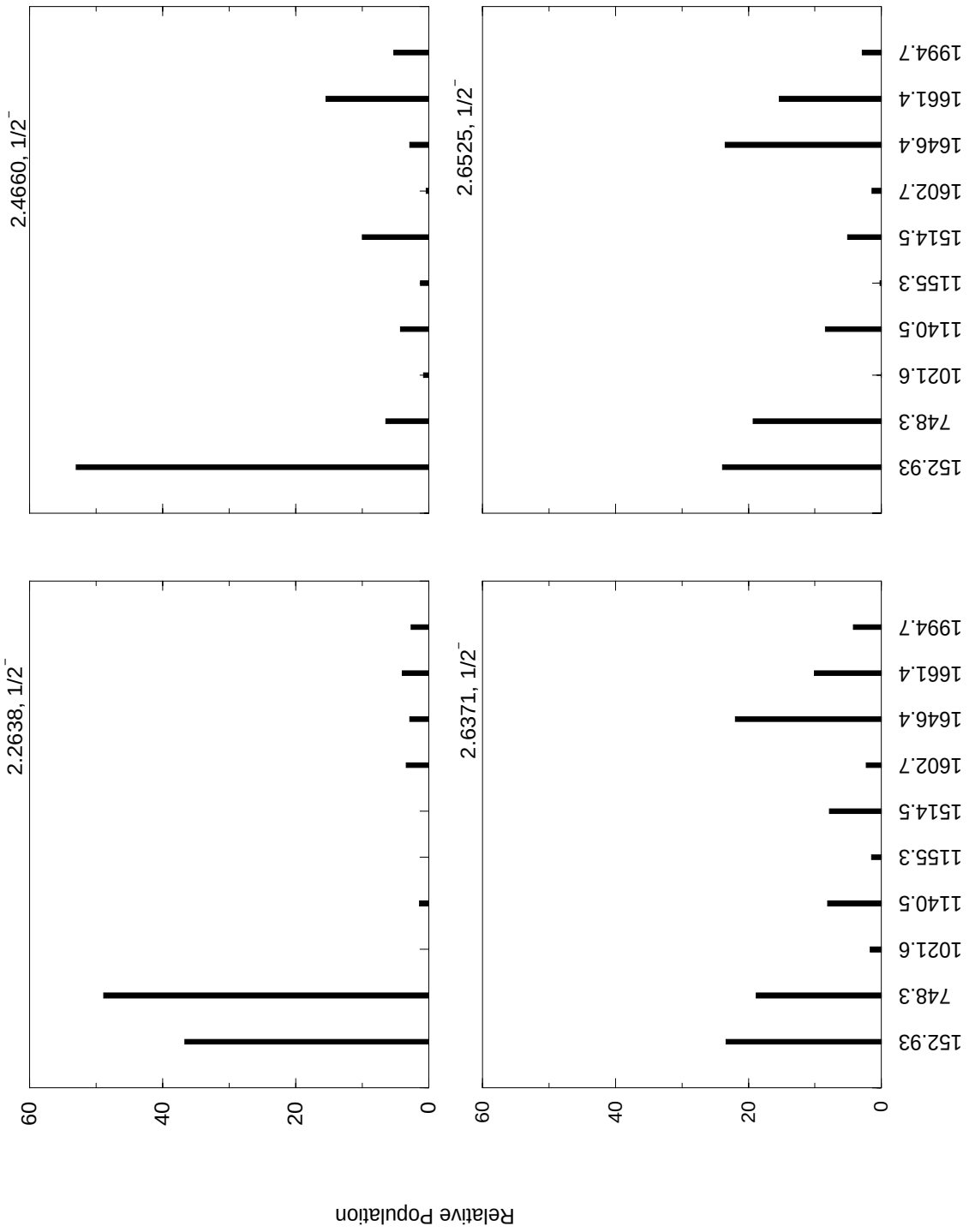

Figure B.6: Relative population of low-lying levels by the 2.2538, 2.4550, 2.5371 and 2.5525 MeV $\frac{1}{2}^-$ resonances.

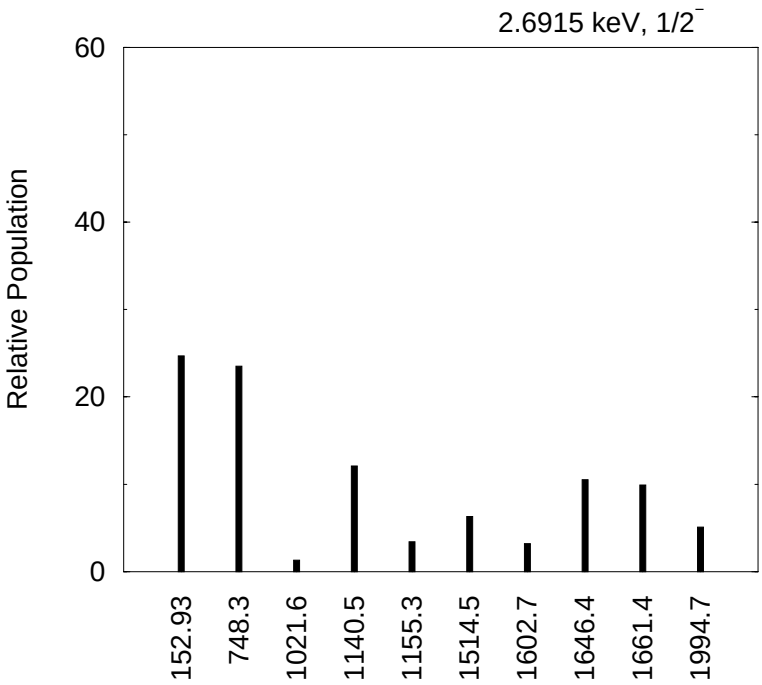

Figure B.7: Relative population of low-lying levels by the 2.6915 MeV $\frac{1}{2}^-$ resonance.

Table B.5: Relative population of low-lying levels by the 2.1936, 2.5004, 2.5344 and 2.6081 MeV $\frac{3}{2}^-$ resonances.

E_{Level} (keV)	2.1936 MeV	2.5004 MeV	2.5344 MeV	2.6081 MeV
152.9	0.29 ± 0.01	0.27 ± 0.01	0.23 ± 0.01	0.677 ± 0.008
748.3	0.161 ± 0.005	0.250 ± 0.007	0.135 ± 0.005	0.087 ± 0.002
1021.6	0.029 ± 0.002	0.055 ± 0.002	0.095 ± 0.003	0.0007 ± 0.0001
1140.5	0.140 ± 0.005	0.077 ± 0.004	0.109 ± 0.004	0.075 ± 0.002
1155.3	0.081 ± 0.003	0.023 ± 0.002	0.065 ± 0.003	0.0049 ± 0.0003
1514.5	0.103 ± 0.007	0.022 ± 0.003	0.068 ± 0.005	0.030 ± 0.002
1602.7	0.037 ± 0.006	0.014 ± 0.003	0.043 ± 0.008	0.014 ± 0.002
1646.4	0.027 ± 0.004	0.15 ± 0.01	0.026 ± 0.004	0.029 ± 0.003
1661.4	0.089 ± 0.004	0.086 ± 0.003	0.138 ± 0.004	0.042 ± 0.001
1994.7	0.048 ± 0.005	0.061 ± 0.005	0.097 ± 0.007	0.040 ± 0.003

Table B.6: Relative population of low-lying levels by the 2.6107, 2.6964, 2.7007 and 2.7153 MeV $\frac{3}{2}^-$ resonances.

E_{Level} (keV)	2.6107 MeV	2.6964 MeV	2.7007 MeV	2.7153 MeV
152.9	0.281 ± 0.009	0.271 ± 0.009	0.189 ± 0.006	0.29 ± 0.01
748.3	0.219 ± 0.004	0.147 ± 0.005	0.170 ± 0.004	0.159 ± 0.005
1021.6	0.0057 ± 0.0006	0.0069 ± 0.0008	0.064 ± 0.002	0.002 ± 0.001
1140.5	0.110 ± 0.003	0.188 ± 0.005	0.116 ± 0.003	0.131 ± 0.004
1155.3	0.017 ± 0.001	0.025 ± 0.001	0.074 ± 0.002	0.015 ± 0.002
1514.5	0.053 ± 0.004	0.059 ± 0.004	0.057 ± 0.004	0.130 ± 0.008
1602.7	0.025 ± 0.003	0.024 ± 0.002	0.093 ± 0.006	0.012 ± 0.004
1646.4	0.065 ± 0.007	0.034 ± 0.004	0.099 ± 0.009	0.10 ± 0.01
1661.4	0.164 ± 0.004	0.109 ± 0.003	0.108 ± 0.003	0.100 ± 0.004
1994.7	0.060 ± 0.005	0.136 ± 0.009	0.031 ± 0.003	0.056 ± 0.004

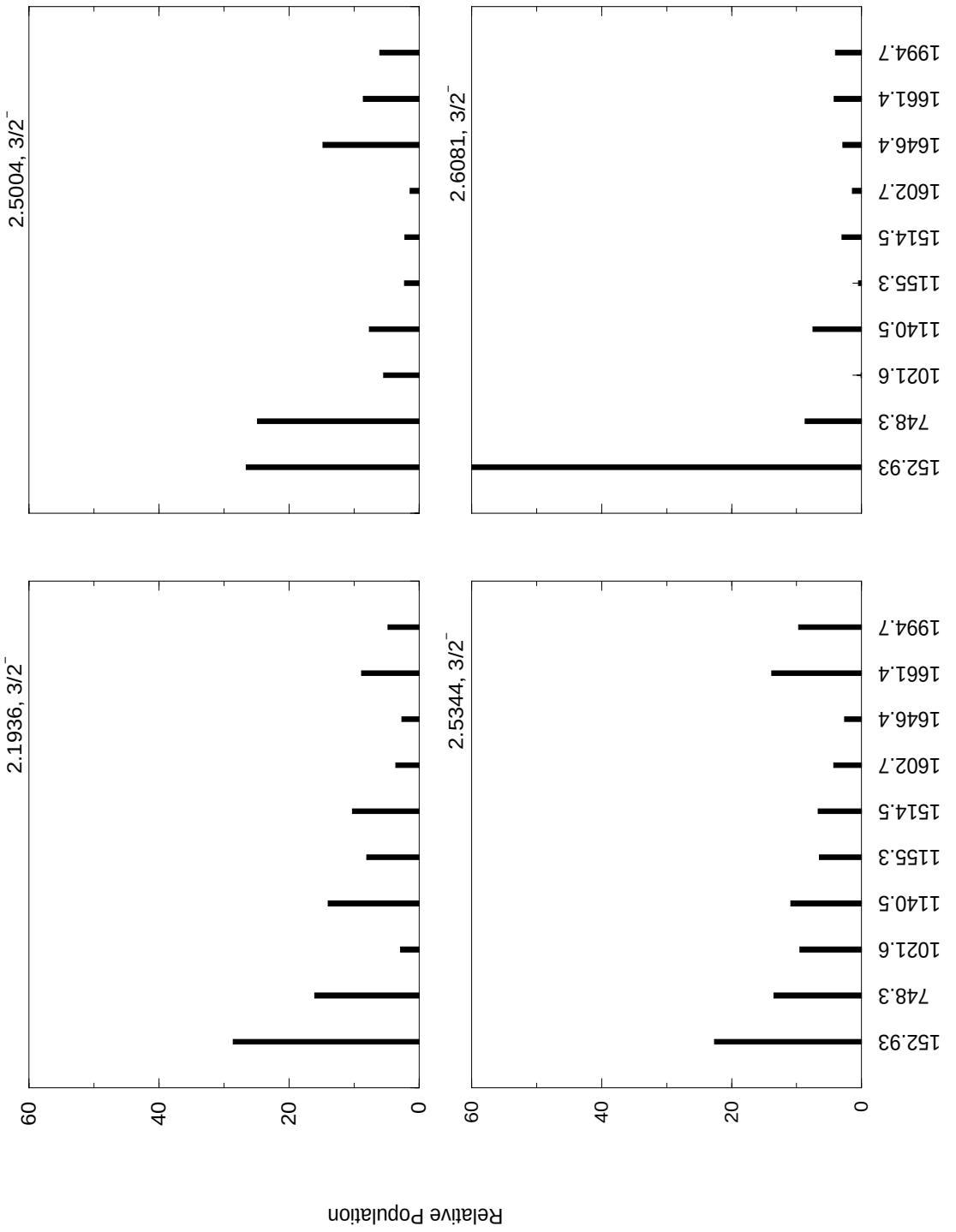

.

Figure B.8: Relative population of low-lying levels by the 2.1936, 2.5004, 2.5344 and 2.6081 MeV $\frac{3}{2}^-$ resonances.

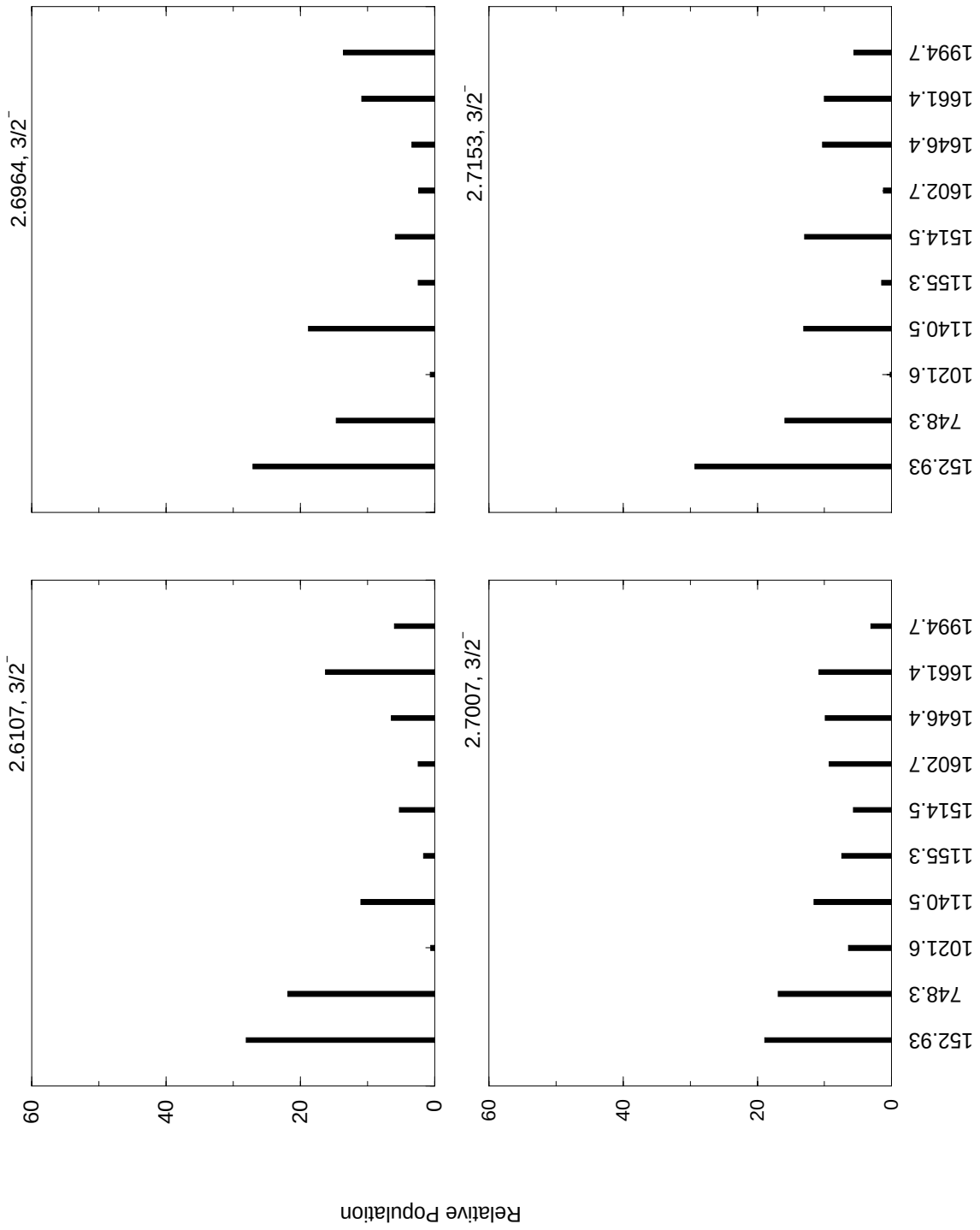

Figure B.9: Relative population of low-lying levels by the 2.6107, 2.6964, 2.7007 and 2.7153 MeV $\frac{3}{2}^-$ resonances.

Appendix C

DICEBOX Relative Populations

This appendix presents the DICEBOX predictions for the relative population of low-lying levels for each of the 27 ^{49}V resonances studied. The information is presented both as plots and tables. The format is the same as for the experimental results presented in Appendix B. See Chapter 8 for discussion of the model parameters used to generate these predictions. Those values less than < 0.0001 are so designated.

Table C.1: DICEBOX predictions for relative population of low-lying levels by the 2.0615, 2.2045, 2.5207, 2.5419 and 2.5575 MeV $\frac{1}{2}^+$ resonances.

E_{Level} (keV)	2.0615 MeV	2.2045 MeV	2.5207 MeV	2.5419 MeV	2.5575 MeV
152.9	0.51 ± 0.09	0.50 ± 0.08	0.5 ± 0.1	0.53 ± 0.08	0.50 ± 0.09
748.3	0.20 ± 0.09	0.23 ± 0.09	0.2 ± 0.1	0.20 ± 0.08	0.22 ± 0.09
1021.6	< 0.0001	< 0.0001	< 0.0001	< 0.0001	< 0.0001
1140.5	0.05 ± 0.03	0.04 ± 0.02	0.04 ± 0.02	0.05 ± 0.02	0.05 ± 0.03
1155.3	0.00016 ± 0.00008	0.00016 ± 0.00009	0.00024 ± 0.00009	0.00025 ± 0.00009	0.00024 ±0.00009
1514.5	0.011 ± 0.004	0.012 ± 0.005	0.012 ± 0.005	0.012 ± 0.004	0.013 ± 0.005
1602.7	0.0007 ± 0.0003	0.0008 ± 0.0004	0.0008 ± 0.0004	0.0009 ± 0.0004	0.0009 ± 0.0004
1646.4	0.09 ± 0.08	0.05 ± 0.05	0.07 ± 0.06	0.06 ± 0.05	0.05 ± 0.05
1661.4	0.07 ± 0.06	0.10 ± 0.07	0.06 ± 0.04	0.07 ± 0.06	0.09 ± 0.08
1994.7	0.08 ± 0.07	0.06 ± 0.05	0.04 ± 0.05	0.08 ± 0.06	0.07 ± 0.07

Table C.2: DICEBOX predictions for relative population of low-lying levels by the 2.2885, 2.3182, 2.6180, 2.7102 and 2.7131 MeV $\frac{1}{2}^+$ resonances.

E_{Level} (keV)	2.2885 MeV	2.3182 MeV	2.6180 MeV	2.7102 MeV	2.7131 MeV
152.9	0.50 ± 0.08	0.51 ± 0.08	0.53 ± 0.09	0.54 ± 0.09	0.52 ± 0.09
748.3	0.24 ± 0.07	0.24 ± 0.09	0.20 ± 0.08	0.22 ± 0.09	0.20 ± 0.09
1021.6	< 0.0001	< 0.0001	< 0.0001	< 0.0001	< 0.0001
1140.5	0.04 ± 0.03	0.04 ± 0.02	0.04 ± 0.02	0.04 ± 0.03	0.04 ± 0.02
1155.3	0.00016 ± 0.00009	0.00016 ± 0.00008	0.00024 ± 0.00009	0.00024 ± 0.00017	0.00024 ±0.00009
1514.5	0.010 ± 0.004	0.011 ± 0.004	0.011 ± 0.005	0.011 ± 0.005	0.011 ± 0.004
1602.7	0.0007 ± 0.0003	0.0008 ± 0.004	0.0008 ± 0.0004	0.0008 ± 0.0004	0.0009 ± 0.0004
1646.4	0.09 ± 0.07	0.07 ± 0.06	0.08 ± 0.07	0.06 ± 0.07	0.09 ± 0.08
1661.4	0.06 ± 0.05	0.07 ± 0.06	0.07 ± 0.06	0.06 ± 0.05	0.08 ± 0.08
1994.7	0.06 ± 0.05	0.06 ± 0.04	0.06 ± 0.06	0.06 ± 0.06	0.06 ± 0.05

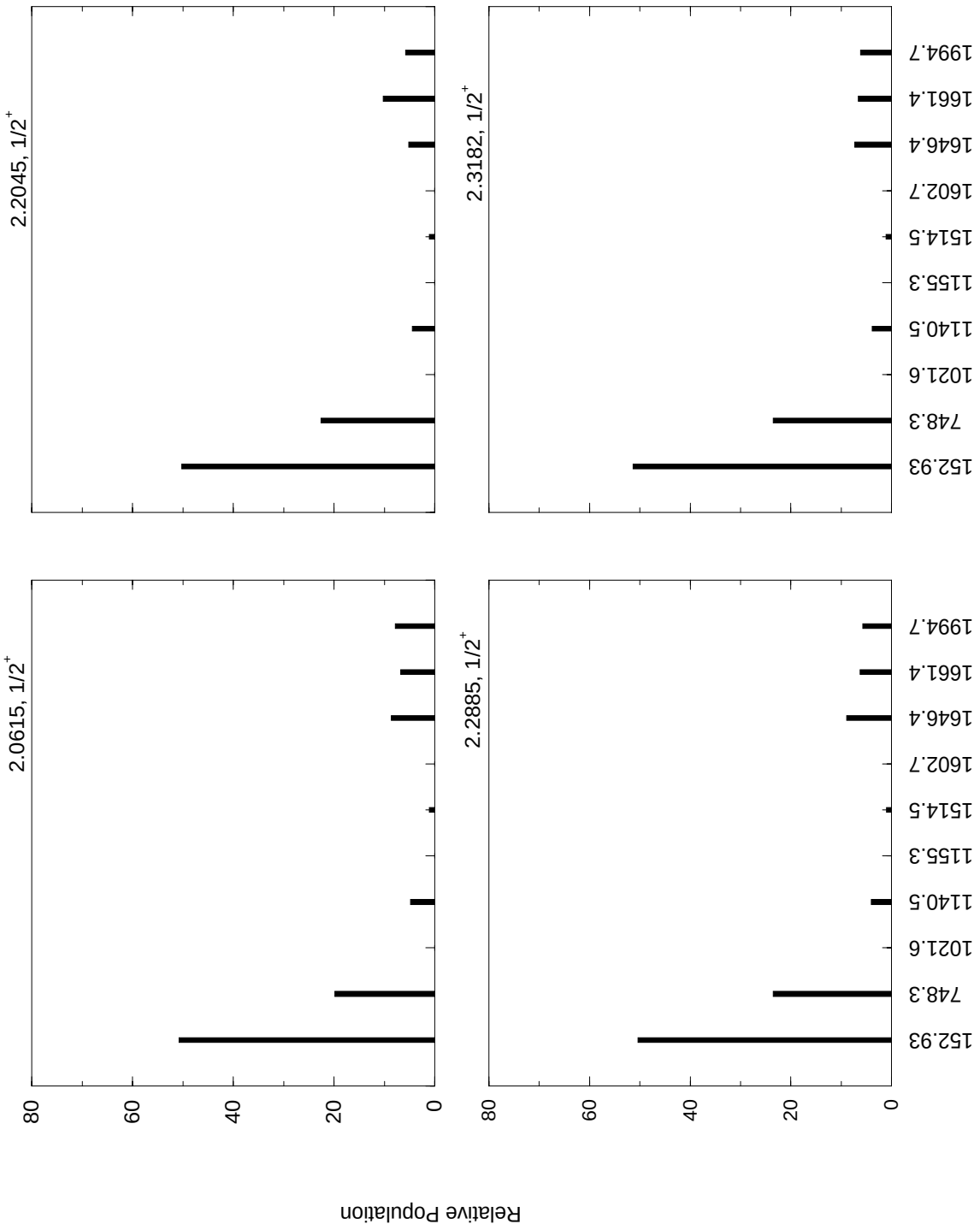

Figure C.1: DICEBOX predictions for relative population of low-lying levels by the 2.0615, 2.2045, 2.2885 and 2.3182 MeV $\frac{1}{2}^+$ resonances.

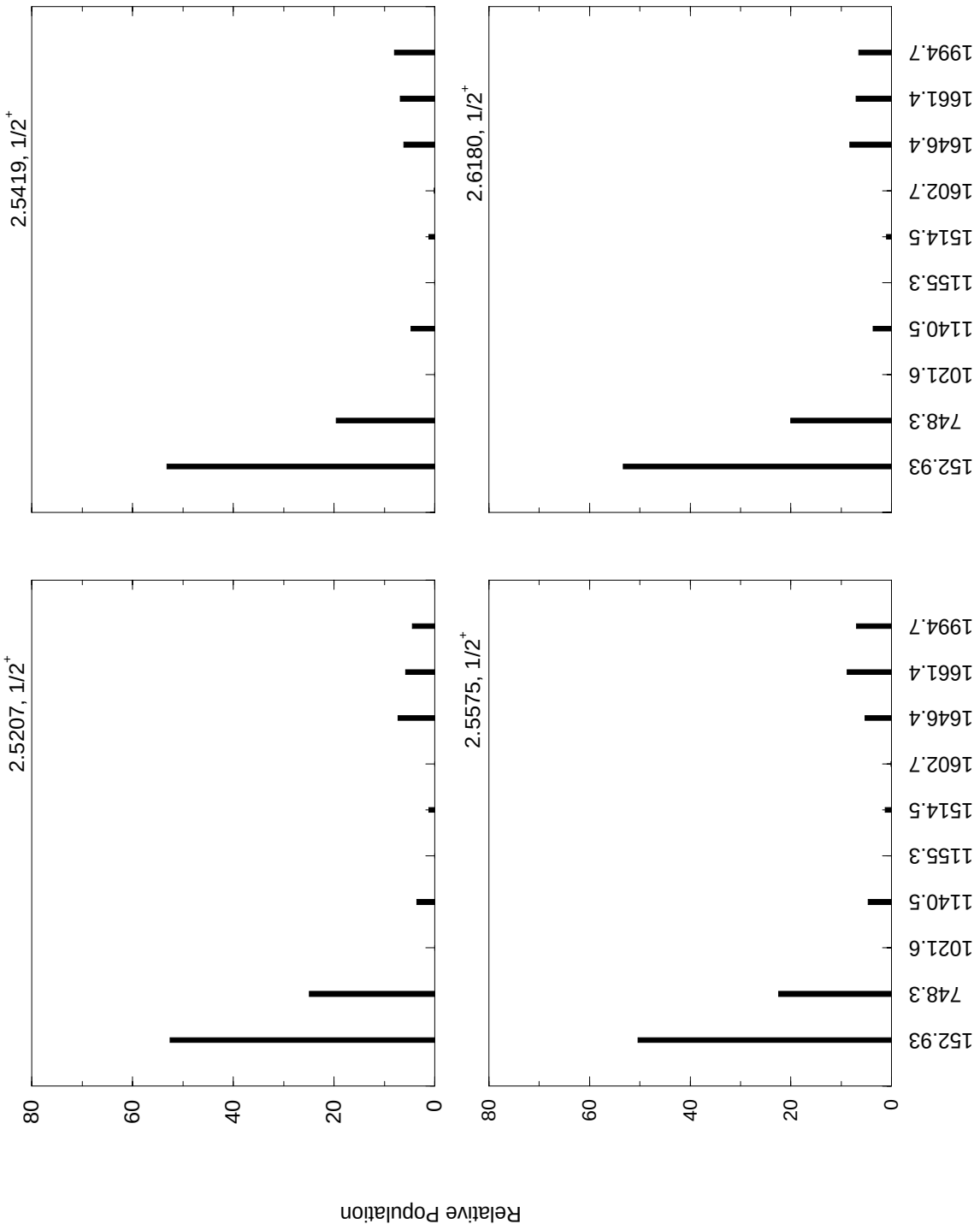

Figure C.2: DICEBOX predictions for relative population of low-lying levels by the 2.0615, 2.2045, 2.2885 and 2.3182 MeV $\frac{1}{2}^+$ resonances.

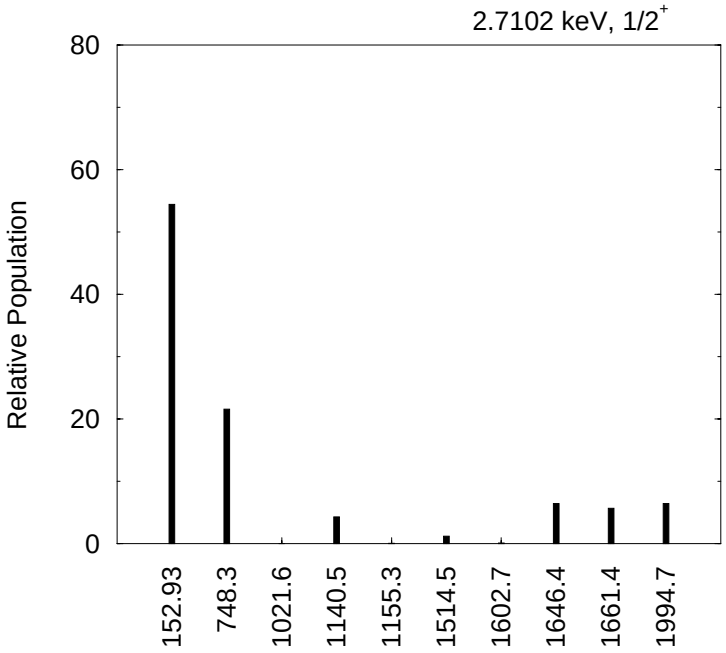

Figure C.3: DICEBOX predictions for relative population of low-lying levels by the 2.7102 MeV $\frac{1}{2}^+$ resonance.

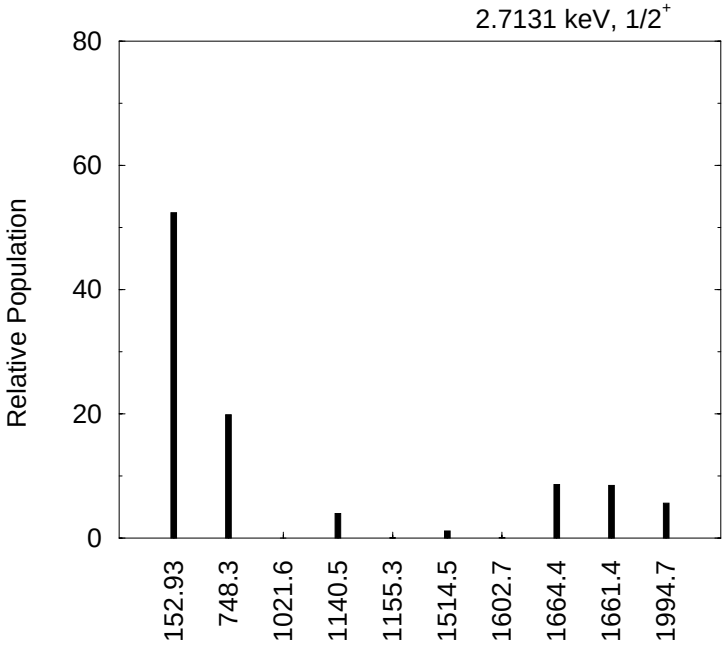

Figure C.4: DICEBOX predictions for relative population of low-lying levels by the 2.7131 MeV $\frac{1}{2}^+$ resonance.

Table C.3: DICEBOX predictions for relative population of low-lying levels by the 2.1163, 2.2108, 2.2121, 2.2308 and 2.2638 MeV $\frac{1}{2}^-$ resonances.

E_{Level} (keV)	2.1163 MeV	2.2108 MeV	2.2121 MeV	2.2308 MeV	2.2638 MeV
152.9	0.53 ± 0.09	0.52 ± 0.09	0.52 ± 0.09	0.5 ± 0.1	0.56 ± 0.09
748.3	0.19 ± 0.07	0.17 ± 0.08	0.21 ± 0.08	0.22 ± 0.09	0.17 ± 0.06
1021.6	< 0.0001	< 0.0001	< 0.0001	< 0.0001	< 0.0001
1140.5	0.33 ± 0.02	0.04 ± 0.02	0.03 ± 0.02	0.03 ± 0.02	0.04 ± 0.02
1155.3	0.00016 ± 0.00008	0.00016 ± 0.00008	0.00016 ± 0.00008	0.00016 ± 0.00008	0.00025 ± 0.00009
1514.5	0.015 ± 0.008	0.02 ± 0.01	0.02 ± 0.01	0.014 ± 0.006	0.02 ± 0.01
1602.7	0.0010 ± 0.0004	0.0011 ± 0.0004	0.001 ± 0.0005	0.0010 ± 0.0005	0.0012 ± 0.0005
1646.4	0.09 ± 0.08	0.07 ± 0.06	0.10 ± 0.10	0.07 ± 0.08	0.09 ± 0.09
1661.4	0.09 ± 0.06	0.09 ± 0.07	0.07 ± 0.06	0.07 ± 0.08	0.06 ± 0.04
1994.7	0.06 ± 0.06	0.09 ± 0.07	0.06 ± 0.05	0.05 ± 0.05	0.07 ± 0.06

Table C.4: DICEBOX predictions for relative population of low-lying levels by the 2.4660, 2.6371, 2.6525 and 2.6915 MeV $\frac{1}{2}^-$ resonances.

E_{Level} (keV)	2.4660 MeV	2.6371 MeV	2.6525 MeV	2.6915 MeV
152.9	0.50 ± 0.08	0.55 ± 0.09	0.58 ± 0.09	0.54 ± 0.09
748.3	0.20 ± 0.08	0.17 ± 0.06	0.18 ± 0.07	0.19 ± 0.07
1021.6	< 0.0001	< 0.0001	< 0.0001	< 0.0001
1140.5	0.03 ± 0.02	0.03 ± 0.01	0.04 ± 0.02	0.03 ± 0.02
1155.3	0.00016 ± 0.00008	0.00017 ± 0.00009	0.00025 ± 0.00009	0.00024 ± 0.00009
1514.5	0.012 ± 0.005	0.017 ± 0.009	0.015 ± 0.008	0.017 ± 0.009
1602.7	0.0010 ± 0.0004	0.0013 ± 0.0005	0.0013 ± 0.0006	0.0012 ± 0.0006
1646.4	0.09 ± 0.07	0.08 ± 0.08	0.06 ± 0.05	0.08 ± 0.09
1661.4	0.10 ± 0.08	0.09 ± 0.08	0.07 ± 0.06	0.08 ± 0.07
1994.7	0.06 ± 0.05	0.06 ± 0.04	0.07 ± 0.06	0.05 ± 0.04

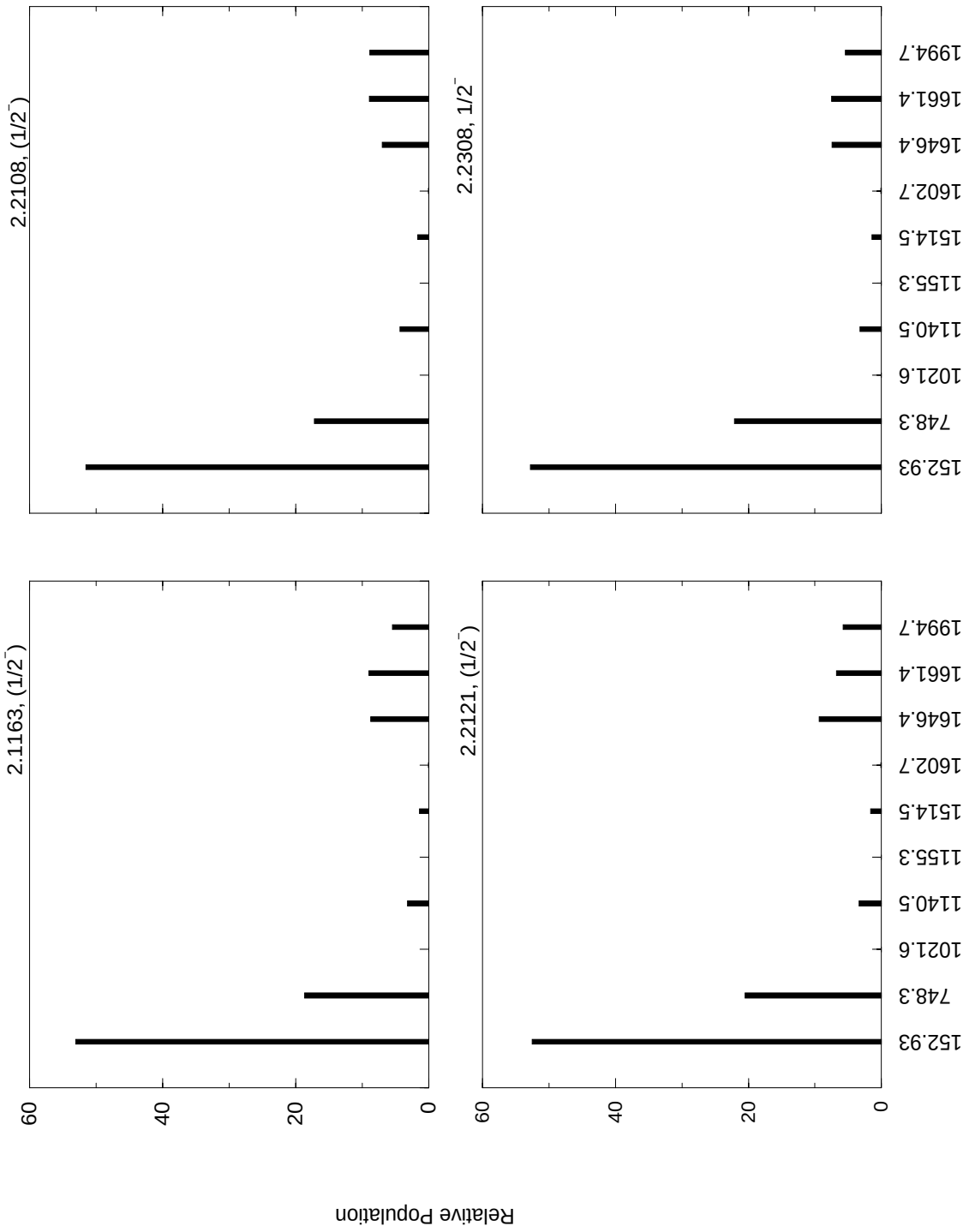

Figure C.5: DICEBOX predictions for relative population of low-lying levels by the 2.1163, 2.2108, 2.2121 and 2.2308 MeV $\frac{1}{2}^-$ resonances.

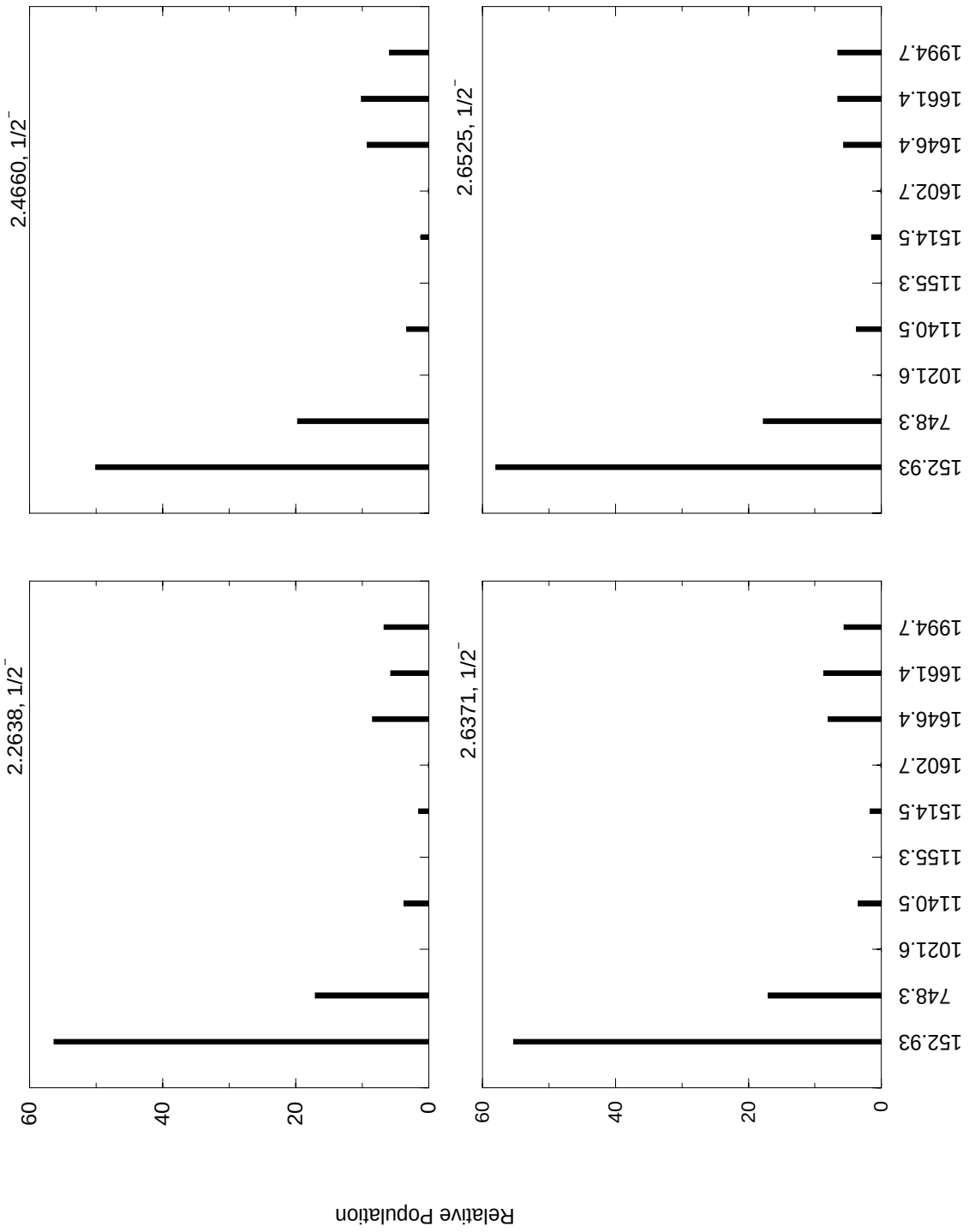

Figure C.6: DICEBOX predictions for relative population of low-lying levels by the 2.2638, 2.4550, 2.5371 and 2.5525 MeV $\frac{1}{2}^-$ resonances.

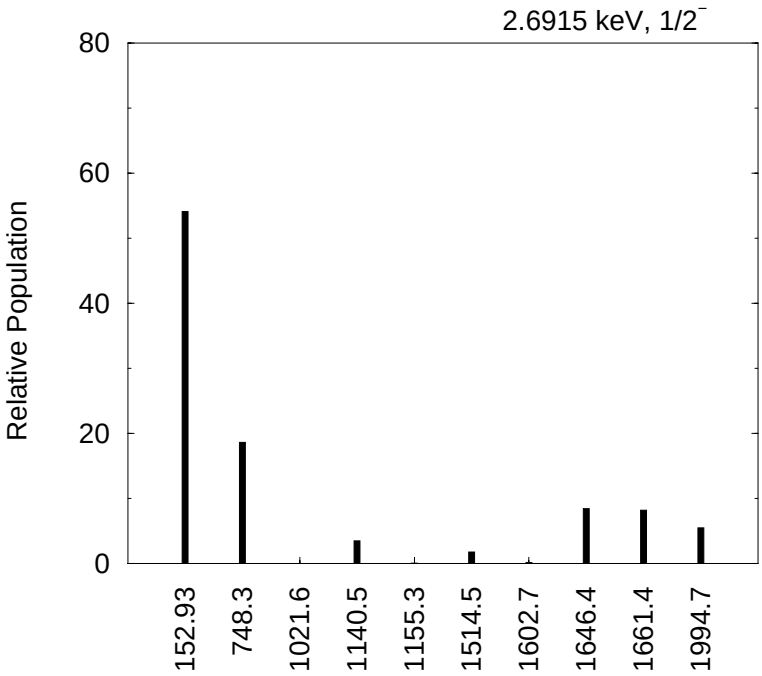

Figure C.7: DICEBOX predictions for relative population of low-lying levels by the 2.6915 MeV $\frac{1}{2}^-$ resonance.

Table C.5: DICEBOX predictions for relative population of low-lying levels by the 2.1936, 2.5004, 2.5344 and 2.6081 MeV $\frac{3}{2}^-$ resonances.

E_{Level} (keV)	2.1936 MeV	2.5004 MeV	2.5344 MeV	2.6081 MeV
152.9	0.49 ± 0.07	0.48 ± 0.09	0.5 ± 0.1	0.51 ± 0.08
748.3	0.19 ± 0.06	0.18 ± 0.07	0.18 ± 0.07	0.16 ± 0.04
1021.6	0.0005 ± 0.0002	0.0005 ± 0.0002	0.0004 ± 0.0002	0.0005 ± 0.0002
1140.5	0.08 ± 0.04	0.11 ± 0.07	0.09 ± 0.07	0.08 ± 0.05
1155.3	0.003 ± 0.001	0.003 ± 0.001	0.003 ± 0.001	0.002 ± 0.001
1514.5	0.06 ± 0.05	0.07 ± 0.05	0.05 ± 0.04	0.06 ± 0.04
1602.7	0.006 ± 0.002	0.007 ± 0.003	0.006 ± 0.002	0.006 ± 0.002
1646.4	0.06 ± 0.04	0.05 ± 0.05	0.06 ± 0.06	0.06 ± 0.04
1661.4	0.06 ± 0.05	0.06 ± 0.06	0.06 ± 0.06	0.07 ± 0.07
1994.7	0.04 ± 0.03	0.05 ± 0.04	0.04 ± 0.04	0.05 ± 0.04

Table C.6: DICEBOX predictions for relative population of low-lying levels by the 2.6107, 2.6964, 2.7007 and 2.7153 MeV $\frac{3}{2}^-$ resonances.

E_{Level} (keV)	2.6107 MeV	2.6964 MeV	2.7007 MeV	2.7153 MeV
152.9	0.5 ± 0.1	0.52 ± 0.08	0.52 ± 0.09	0.5 ± 0.1
748.3	0.18 ± 0.07	0.18 ± 0.07	0.18 ± 0.06	0.18 ± 0.09
1021.6	0.0005 ± 0.0003	0.0005 ± 0.0002	0.0005 ± 0.0002	0.0005 ± 0.0002
1140.5	0.10 ± 0.09	0.09 ± 0.07	0.08 ± 0.05	0.08 ± 0.04
1155.3	0.003 ± 0.002	0.003 ± 0.001	0.003 ± 0.001	0.003 ± 0.001
1514.5	0.05 ± 0.04	0.05 ± 0.05	0.06 ± 0.05	0.05 ± 0.05
1602.7	0.006 ± 0.003	0.006 ± 0.002	0.006 ± 0.002	0.007 ± 0.003
1646.4	0.04 ± 0.03	0.04 ± 0.04	0.05 ± 0.06	0.05 ± 0.05
1661.4	0.05 ± 0.03	0.05 ± 0.04	0.05 ± 0.04	0.06 ± 0.04
1994.7	0.04 ± 0.03	0.05 ± 0.04	0.05 ± 0.04	0.04 ± 0.05

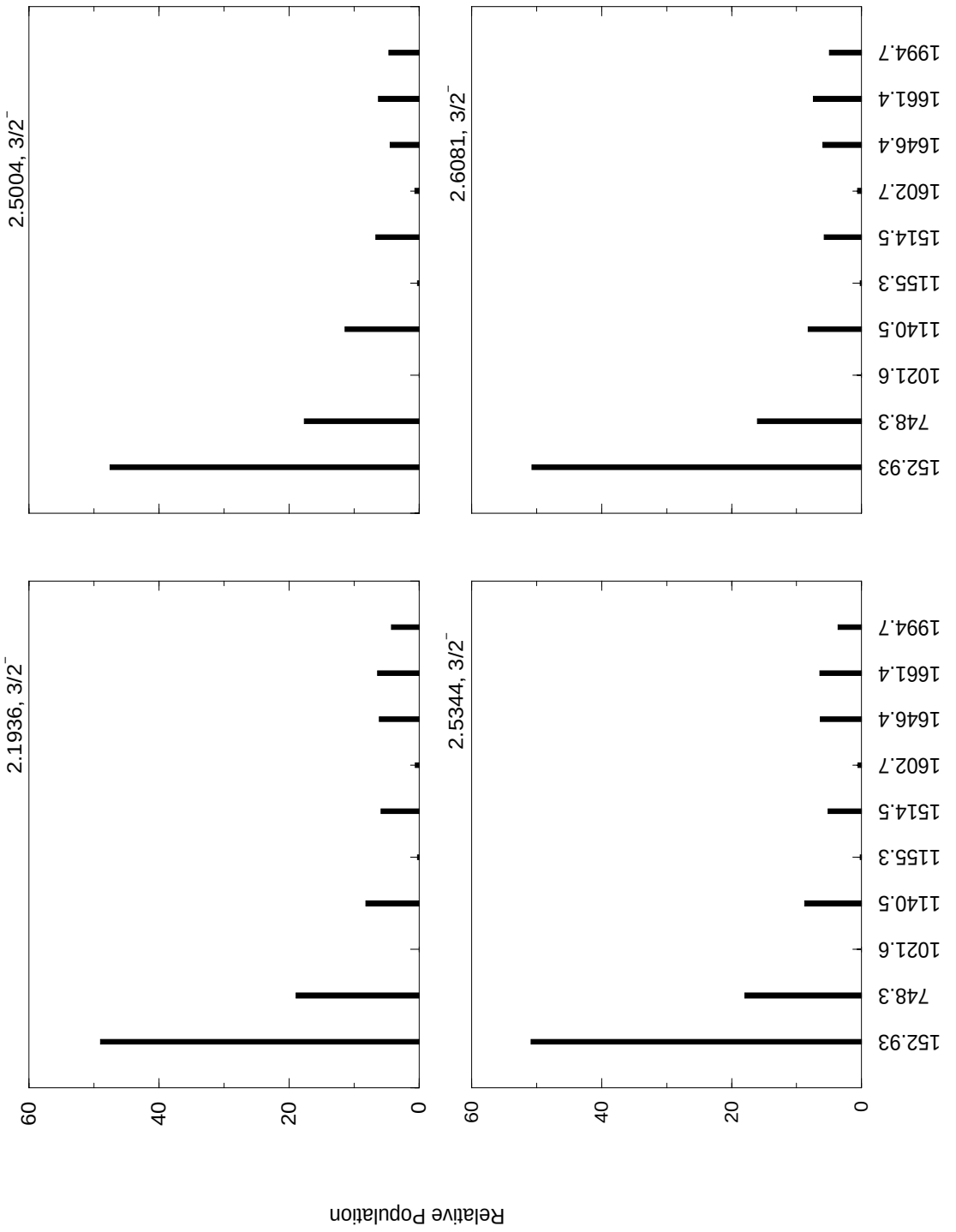

.

Figure C.8: DICEBOX predictions for rleative population of low-lying levels by the 2.1936, 2.5004, 2.5344 and 2.6081 MeV $\frac{3}{2}^-$ resonances.

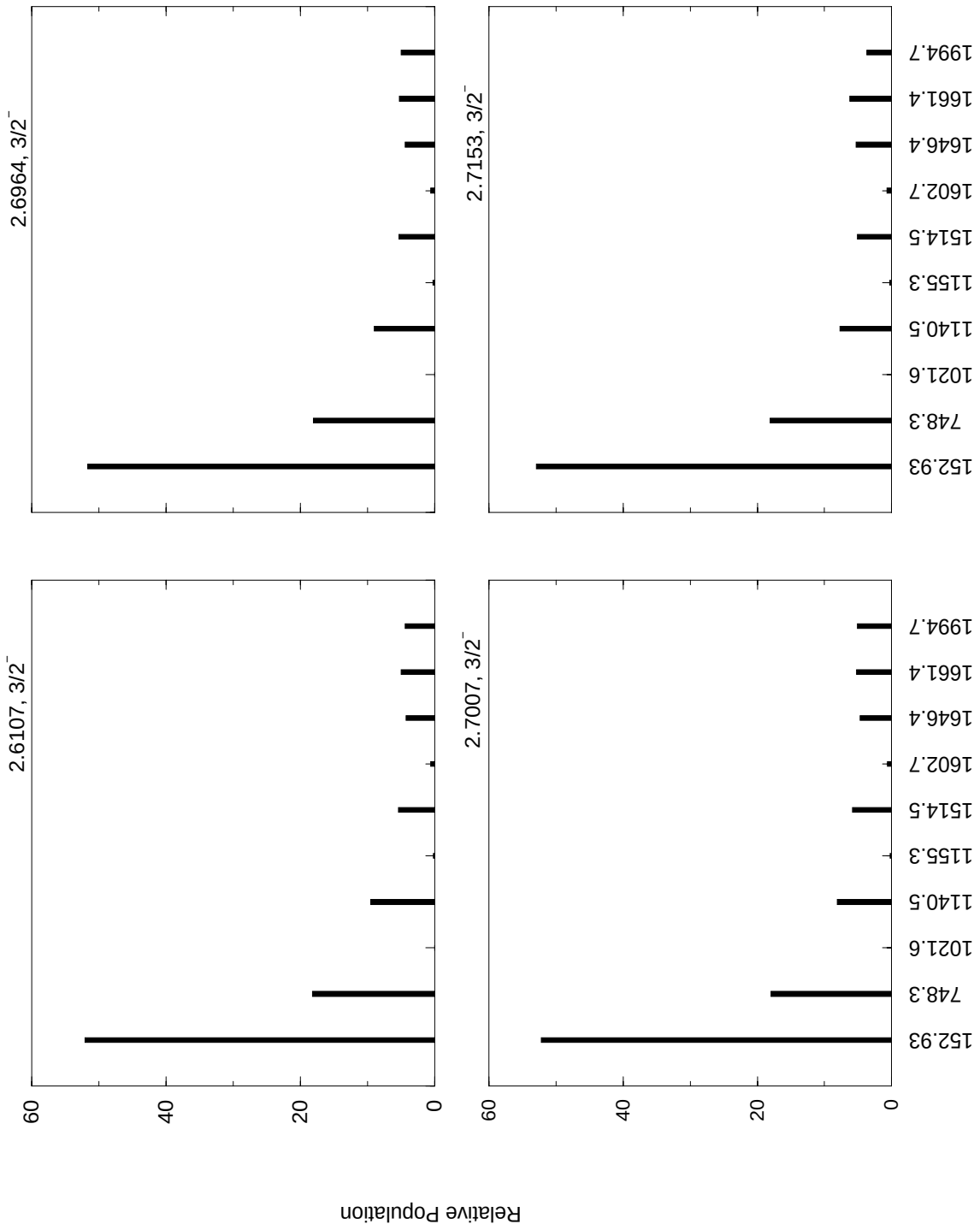

Figure C.9: DICEBOX predictions for relative population of low-lying levels by the 2.6107, 2.6964, 2.7007 and 2.7153 MeV $\frac{3}{2}^-$ resonances.

Appendix D

LLP Method – Prediction and Experiment

This appendix presents DICEBOX predictions (GR model) for the intensity ratios for a number of γ-ray transitions and the experimental results for these ratios. There are several figures (D.1 to D.6) that illustrate the ratios that result when low–lying states of similar spin are populated. No significant difference is anticipated for decay from $1/2^-$ and $3/2^-$ resonances in these cases, and none is observed. By comparison, differences are expected when low-lying states with rather different spin are populated by resonances with different spins. Figures D.7, D.9, D.11, and D.13 illustrate the expected difference in the ratios. However, this difference is not observed experimentally, as shown in Figures D.8, D.10, D.12, and D.14. Results for all of the 27 ^{49}V resonances studied show similar results. The intensities for the 33 γ-rays that were used to calculate the ratios are listed in Appendix A.

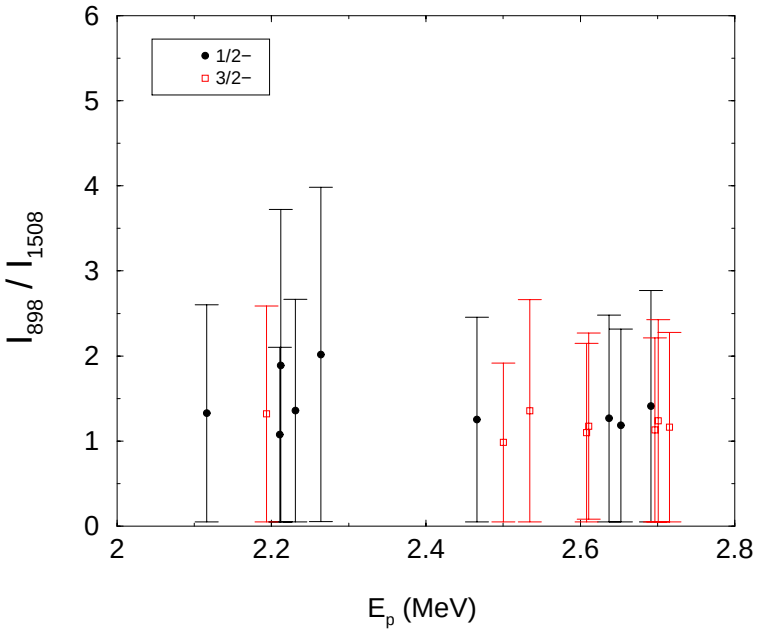

Figure D.1: DICEBOX predictions for the ratio of the intensity of the 898–keV transition ($1/2^+ \rightarrow 3/2^+$) to the intensity of the 1508–keV transition ($3/2^- \rightarrow 3/2^-$).

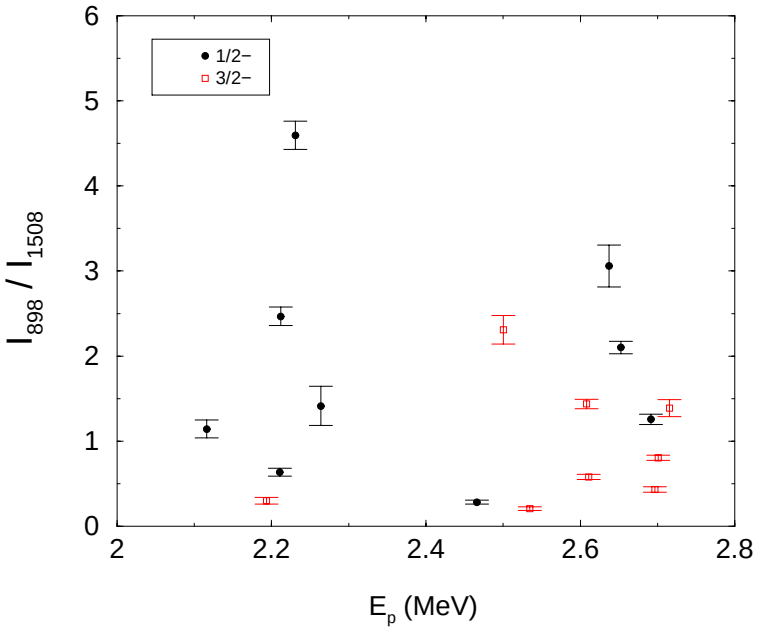

Figure D.2: Experimental ratio of the intensity of the 898–keV transition ($1/2^+ \rightarrow 3/2^+$) to the intensity of the 1508–keV transition ($3/2^- \rightarrow 3/2^-$).

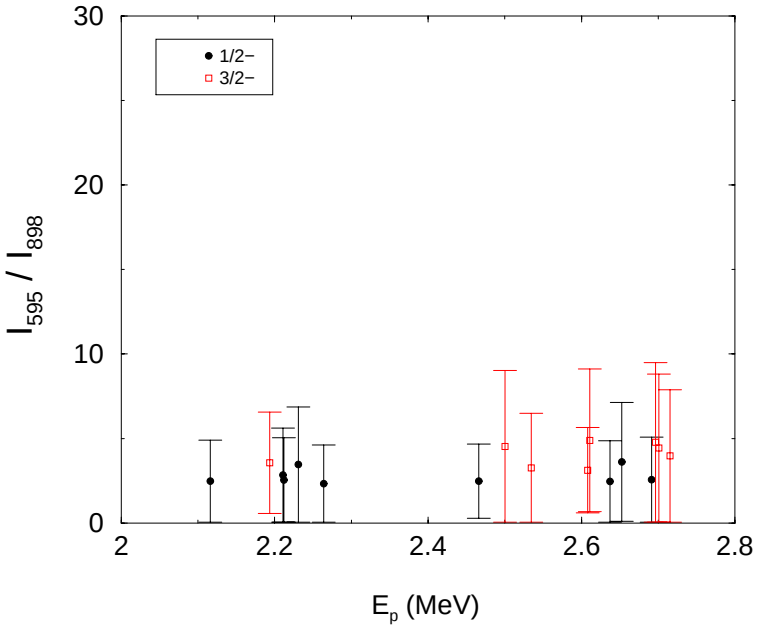

Figure D.3: DICEBOX predictions for the ratio of the intensity of the 595–keV transition ($3/2^+ \rightarrow 3/2^-$) to the intensity of the 898–keV transition ($1/2^+ \rightarrow 3/2^+$).

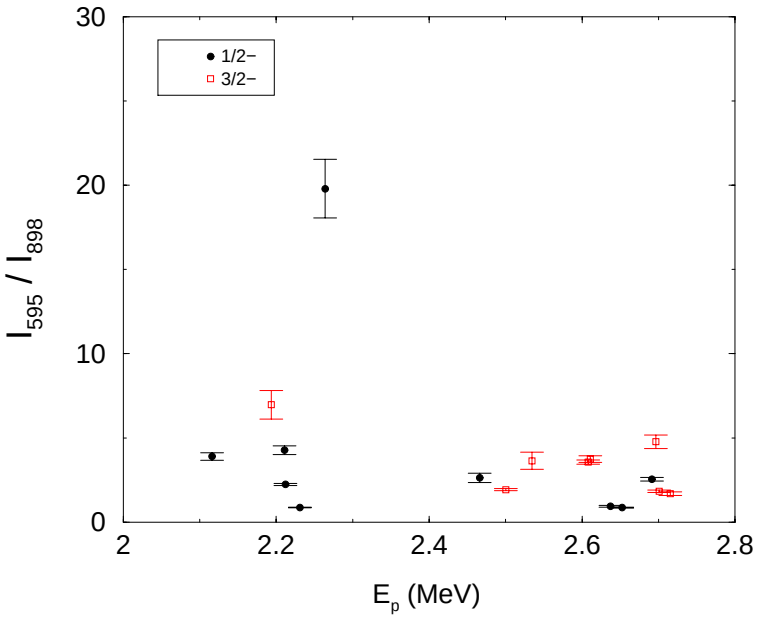

Figure D.4: Experimental ratio of the intensity of the 595–keV transition ($3/2^+ \rightarrow 3/2^-$) to the intensity of the 898–keV transition ($1/2^+ \rightarrow 3/2^+$).

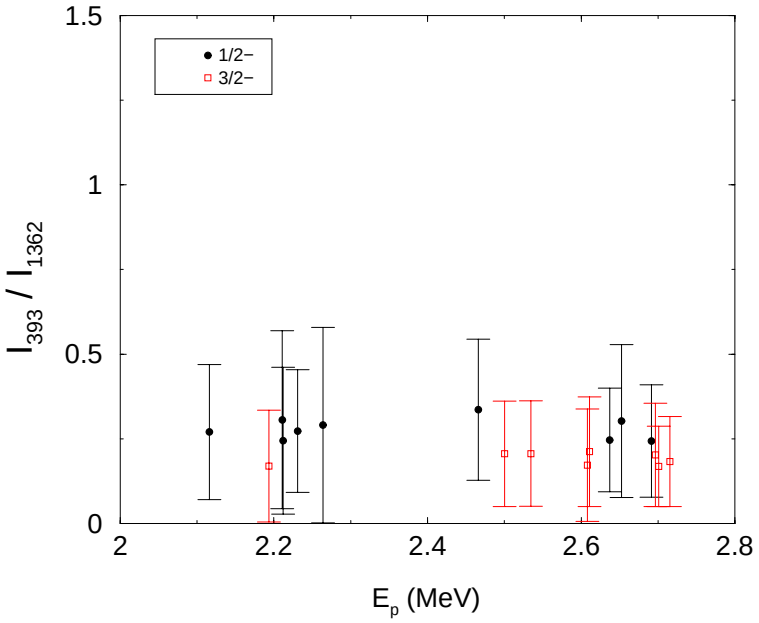

Figure D.5: DICEBOX predictions for the ratio of the intensity of the 393–keV transition ($5/2^+ \rightarrow 3/2^+$) to the intensity of the 1362–keV transition ($5/2^- \rightarrow 3/2^-$).

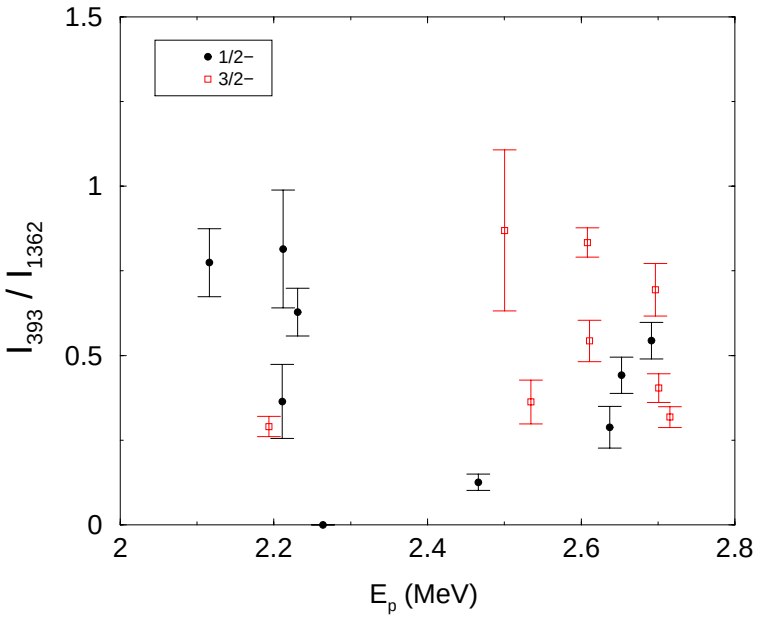

Figure D.6: Experimental ratio of the intensity of the 393–keV transition ($5/2^+ \rightarrow 3/2^+$) to the intensity of the 1362–keV transition ($5/2^- \rightarrow 3/2^-$).

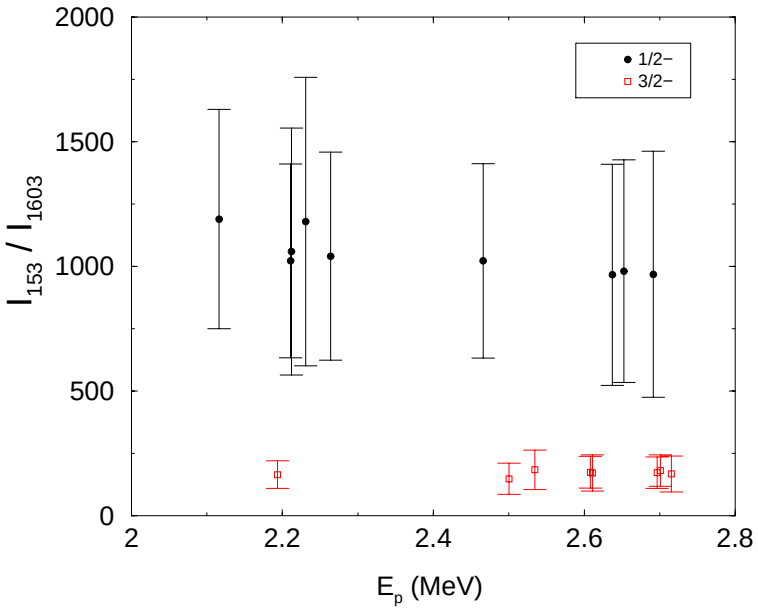

Figure D.7: DICEBOX predictions for the ratio of the intensity of the 153–keV transition ($3/2^- \rightarrow 7/2^-$) to the intensity of the 1603–keV transition ($7/2^+ \rightarrow 7/2^-$).

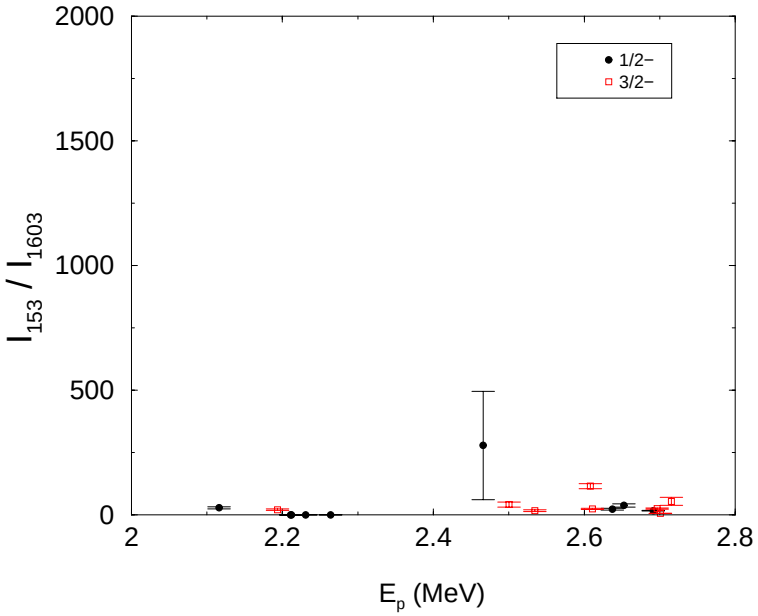

Figure D.8: Experimental ratio of the intensity of the 153–keV transition ($3/2^- \rightarrow 7/2^-$) to the intensity of the 1603–keV transition ($7/2^+ \rightarrow 7/2^-$).

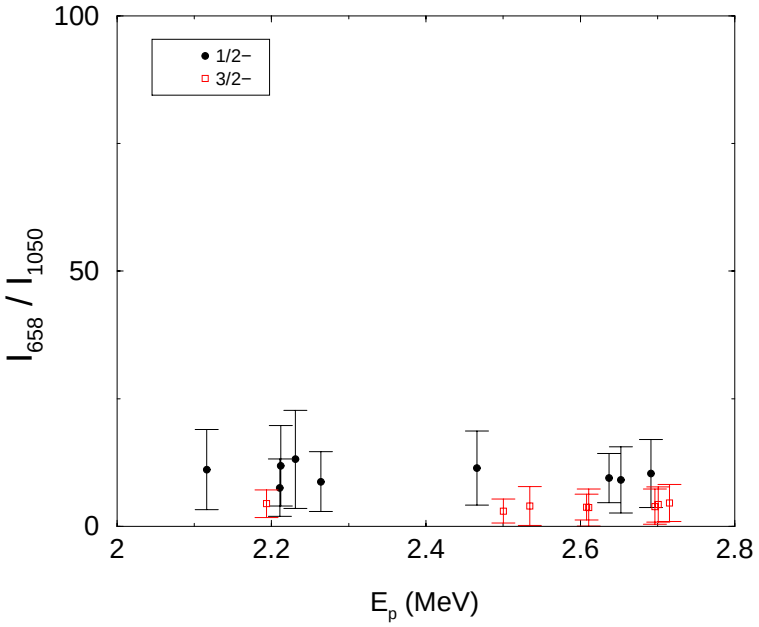

Figure D.9: DICEBOX predictions for the ratio of the intensity of the 658–keV transition ($3/2^+ \rightarrow 5/2^-$) to the intensity of the 1050–keV transition ($5/2^+ \rightarrow 5/2^-$).

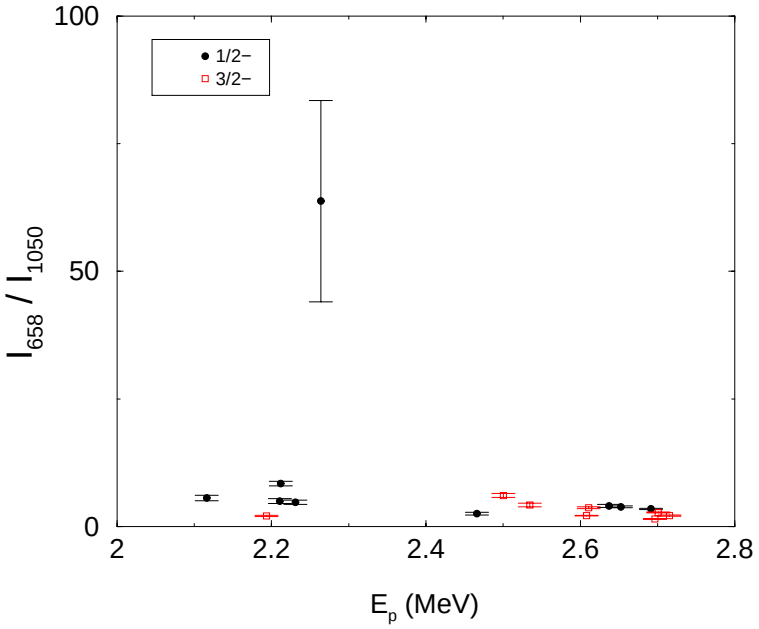

Figure D.10: Experimental ratio of the intensity of the 658–keV transition ($3/2^+ \rightarrow 5/2^-$) to the intensity of the 1050–keV transition ($5/2^+ \rightarrow 5/2^-$).

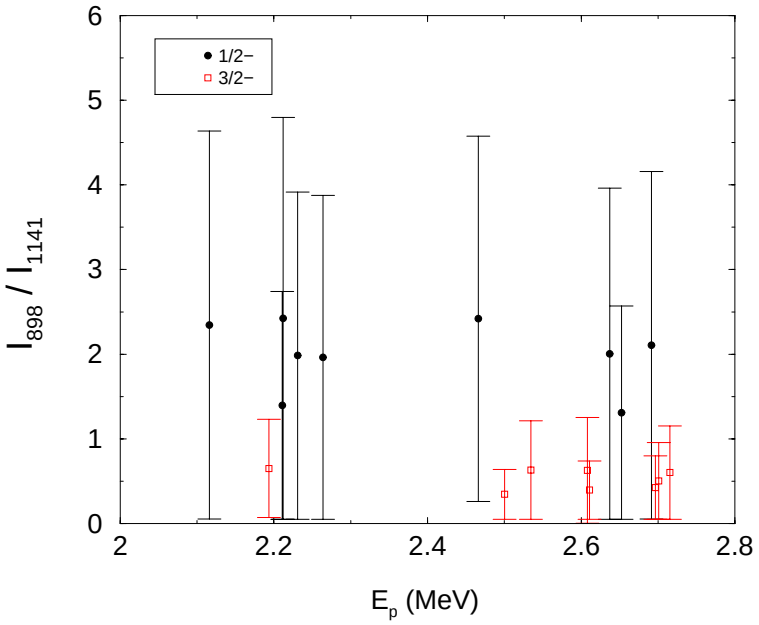

Figure D.11: DICEBOX predictions for the ratio of the intensity of the 898–keV transition ($1/2^+ \rightarrow 3/2^+$) to the intensity of the 1141–keV transition ($5/2^+ \rightarrow 7/2^-$).

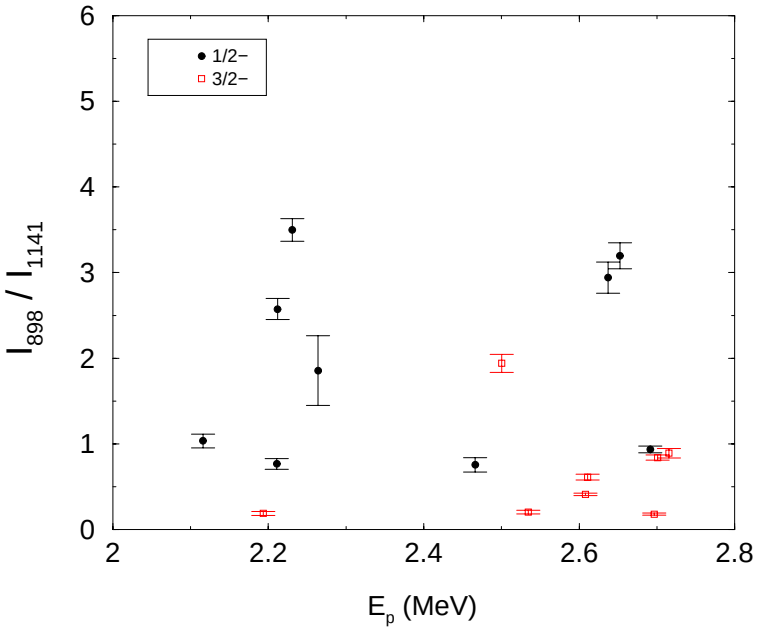

Figure D.12: Experimental ratio of the intensity of the 898–keV transition ($1/2^+ \rightarrow 3/2^+$) to the intensity of the 1141–keV transition ($5/2^+ \rightarrow 7/2^-$).

Appendix E

Excitation Functions

This appendix presents the excitation functions for the (p,p_0), $(p,p_1\gamma)$, and (p,γ) reactions on ^{48}Ti. The elastic scattering data are shown for 165°, while the γ rays were observed at 125°. (In Figure E.7 there is a region in the $(p,p_1\gamma)$ yield above the 2.6641 resonance with no data. This is due to a hardware discriminator briefly set incorrectly.) Some of the (p,γ) yield curves exhibit an undulating background — an effect due to slow beam fluctuations on tantalum slits located just before the γ-ray chamber. The resulting γ rays changed the overall background as the amount of beam on the slits slowly varied. The labeling convention is that the resonance energy refers to the resonance directly below the left-most digit of the resonance energy.

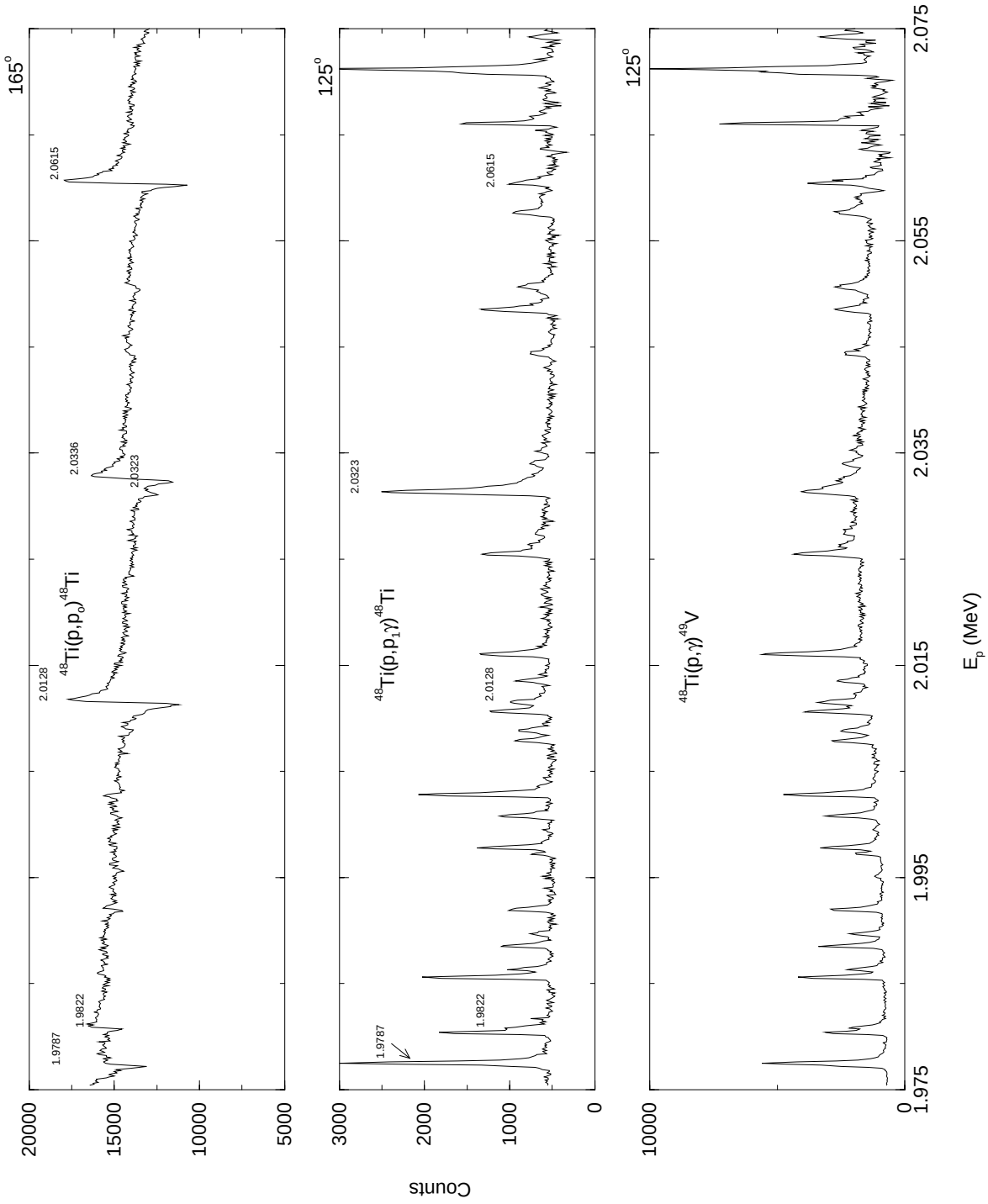

Figure E.1: Elastic, inelastic, and capture yield curves (top, middle, and bottom, respectively) for protons on ^{48}Ti in the energy region E_p = 1.975 to 2.075 MeV.

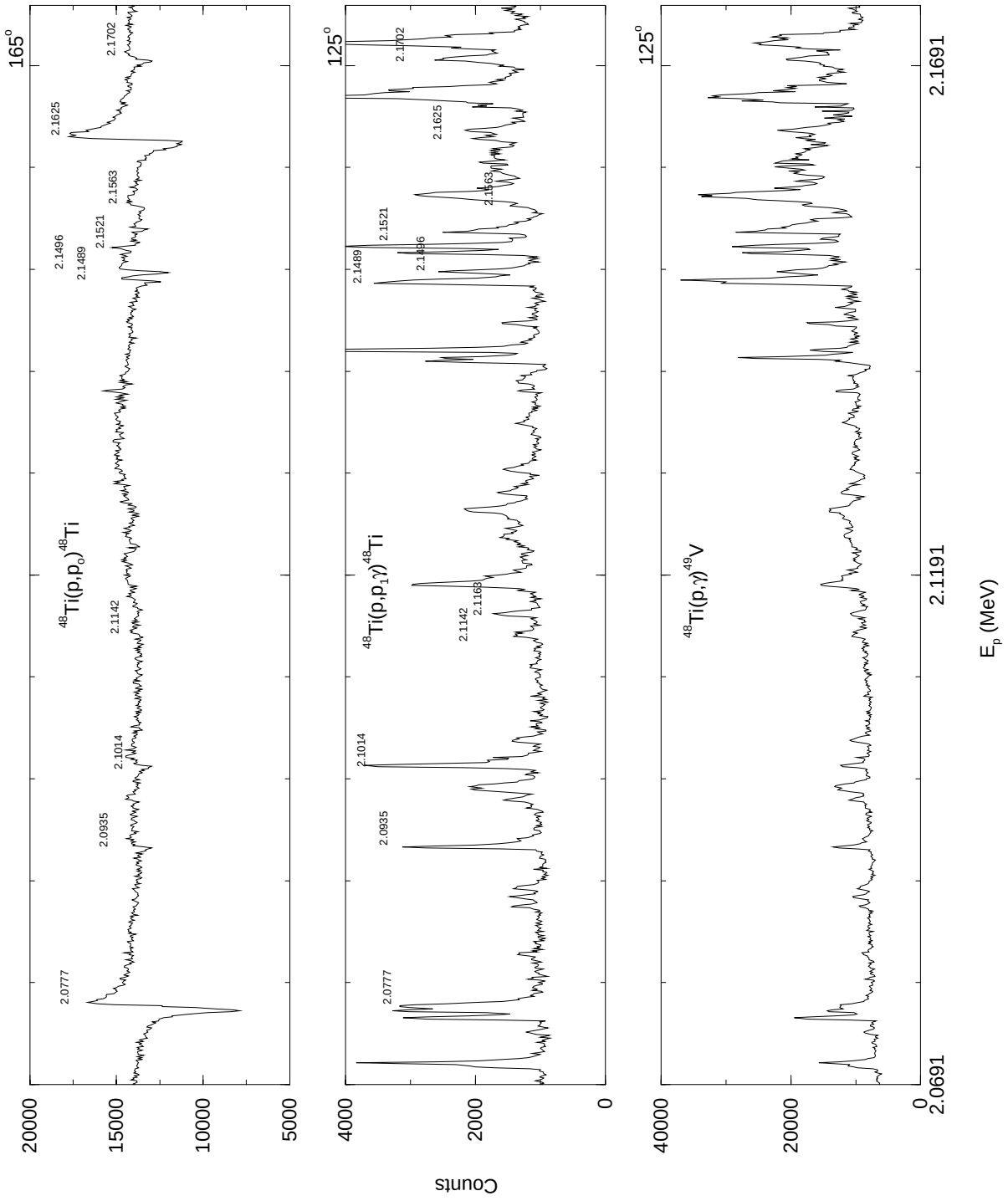

Figure E.2: Elastic, inelastic, and capture yield curves (top, middle, and bottom, respectively) for protons on ^{48}Ti in the energy region E_p = 2.0691 to 2.1750 MeV.

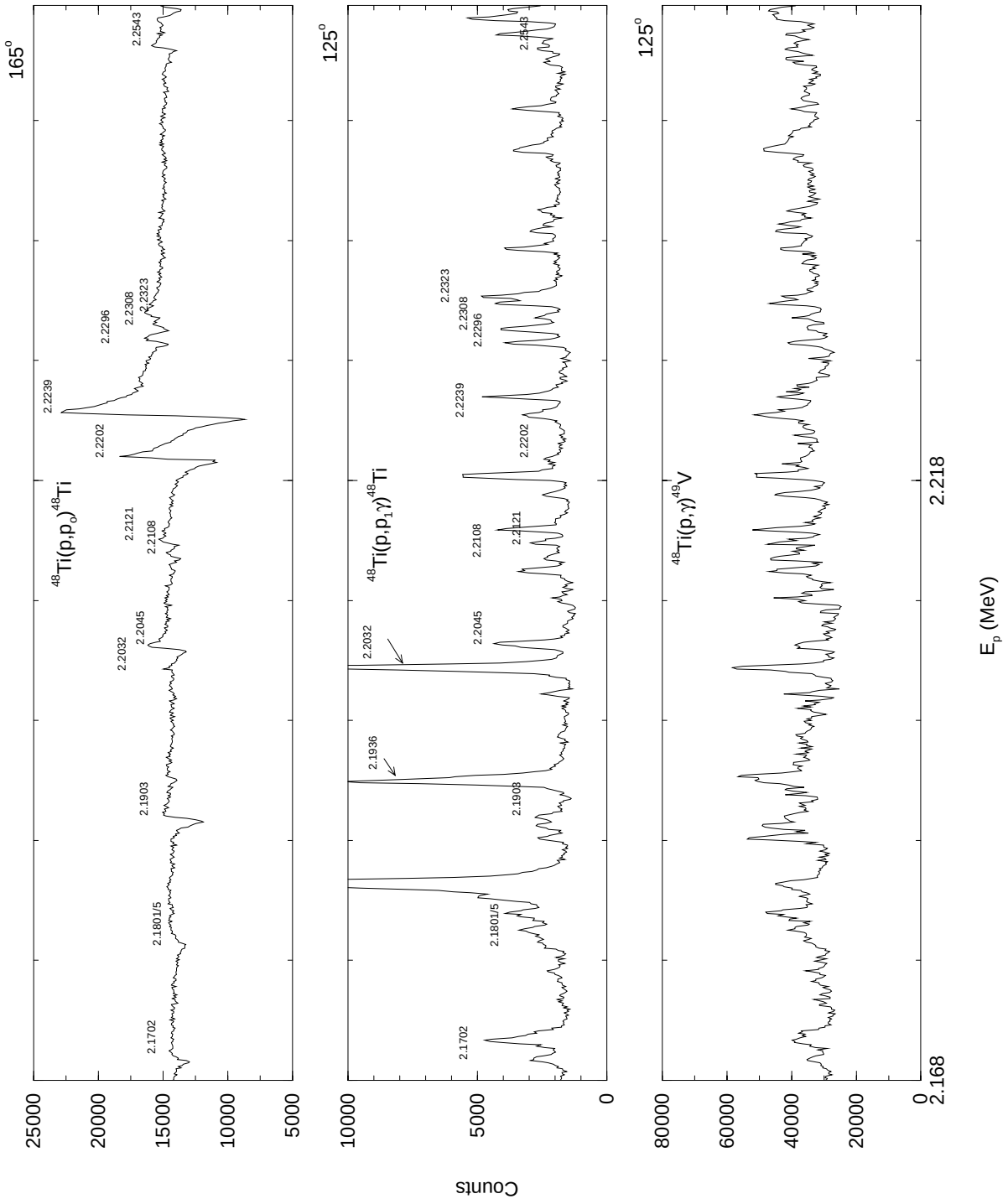

Figure E.3: Elastic, inelastic, and capture yield curves (top, middle, and bottom, respectively) for protons on ^{48}Ti in the energy region E_p = 2.1680 to 2.2576 MeV.

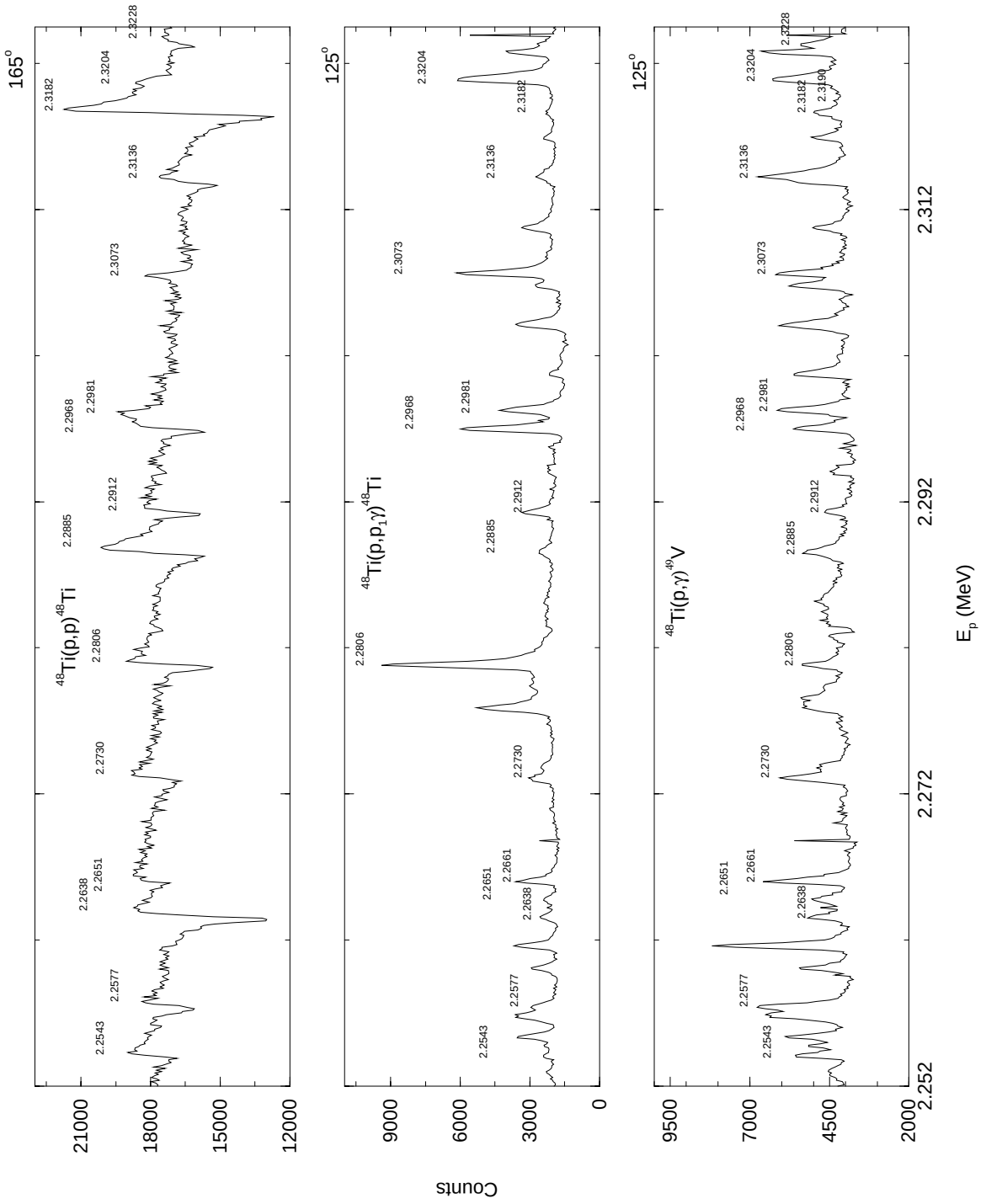

Figure E.4: Elastic, inelastic, and capture yield curves (top, middle, and bottom, respectively) for protons on ^{48}Ti in the energy region E_p = 2.2520 to 2.3245 MeV.

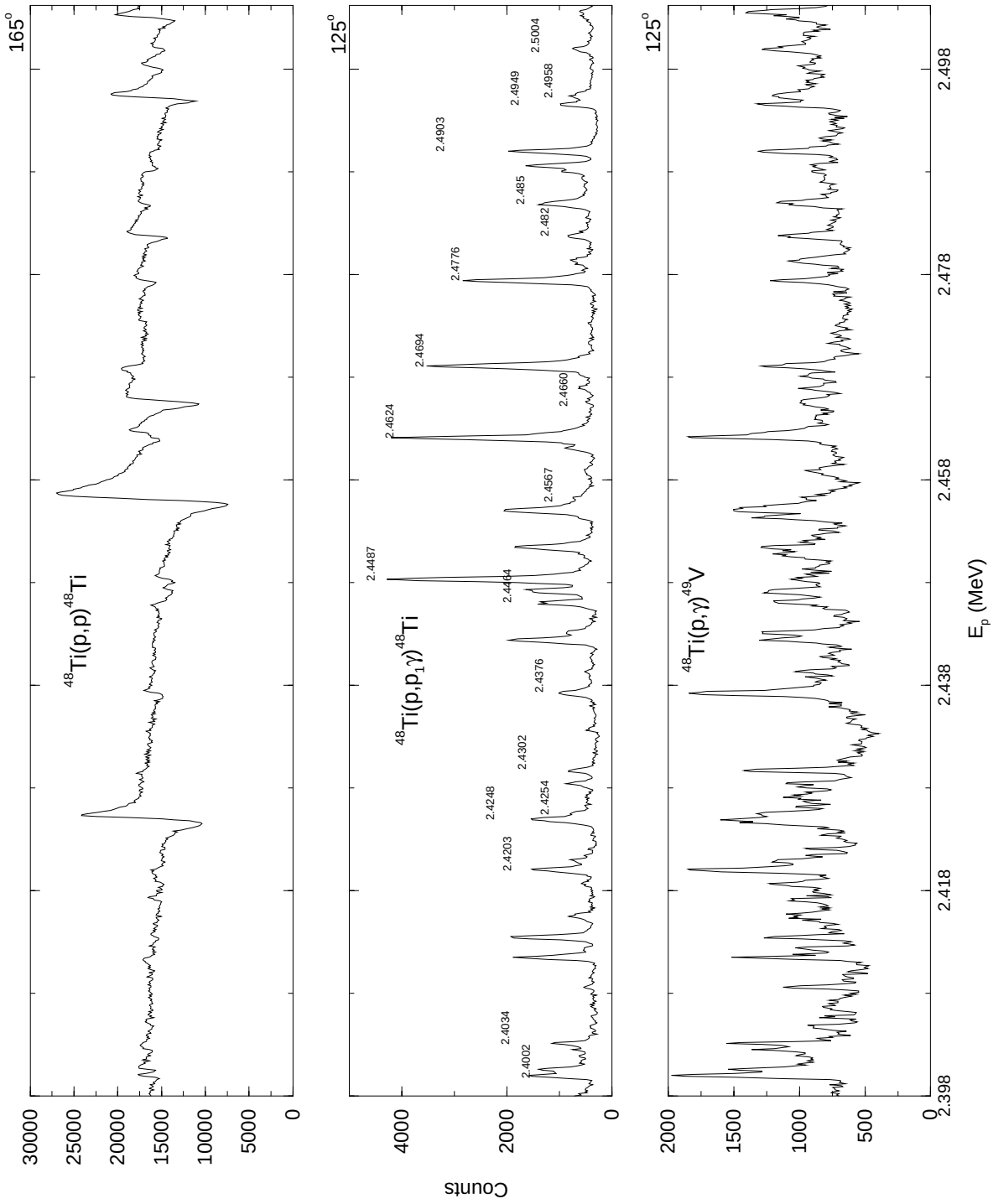

Figure E.5: Elastic, inelastic, and capture yield curves (top, middle, and bottom, respectively) for protons on ^{48}Ti in the energy region E_p = 2.3980 to 2.5042 MeV.

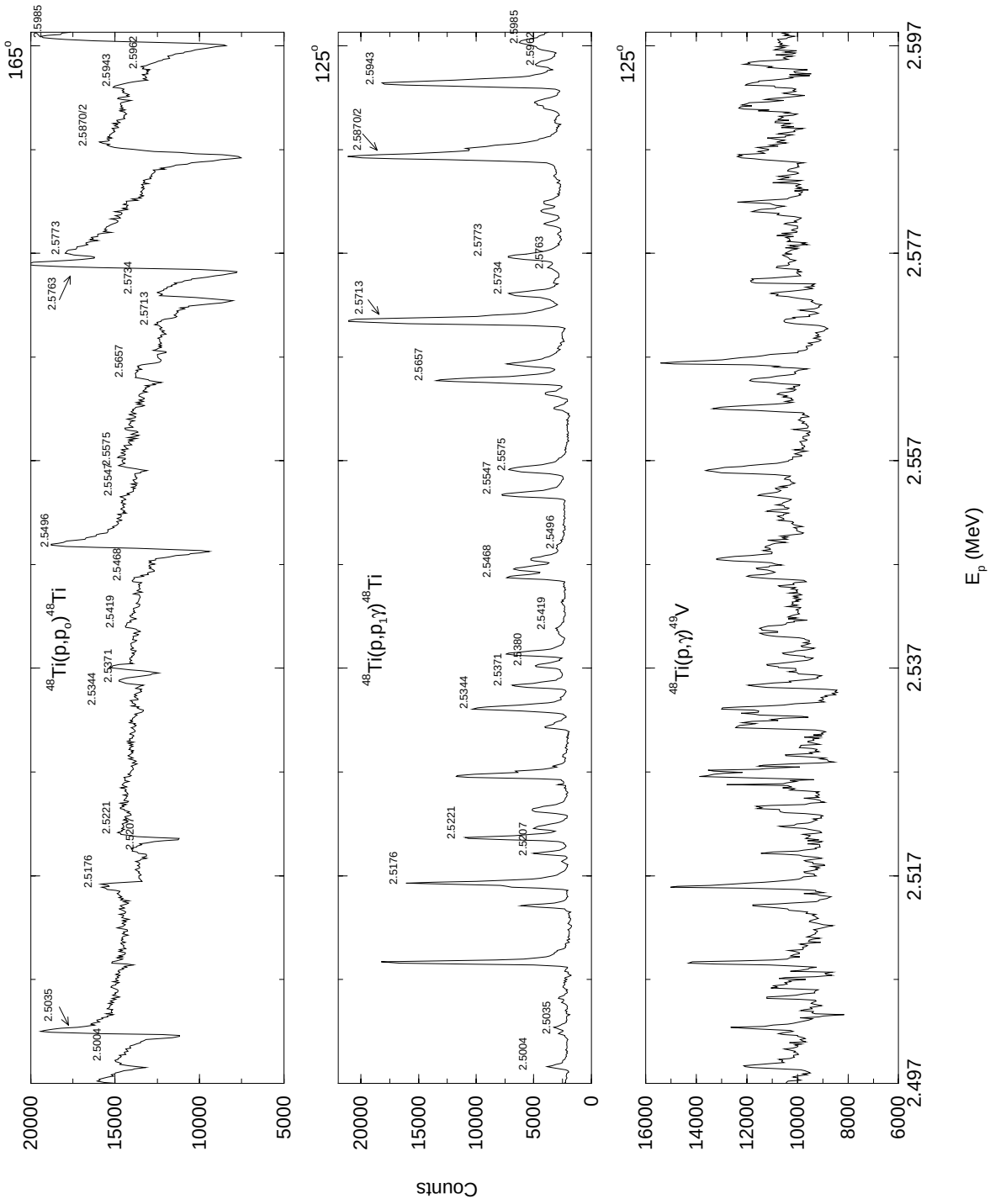

Figure E.6: Elastic, inelastic, and capture yield curves (top, middle, and bottom, respectively) for protons on ^{48}Ti in the energy region E_p = 2.4970 to 2.5983 MeV.

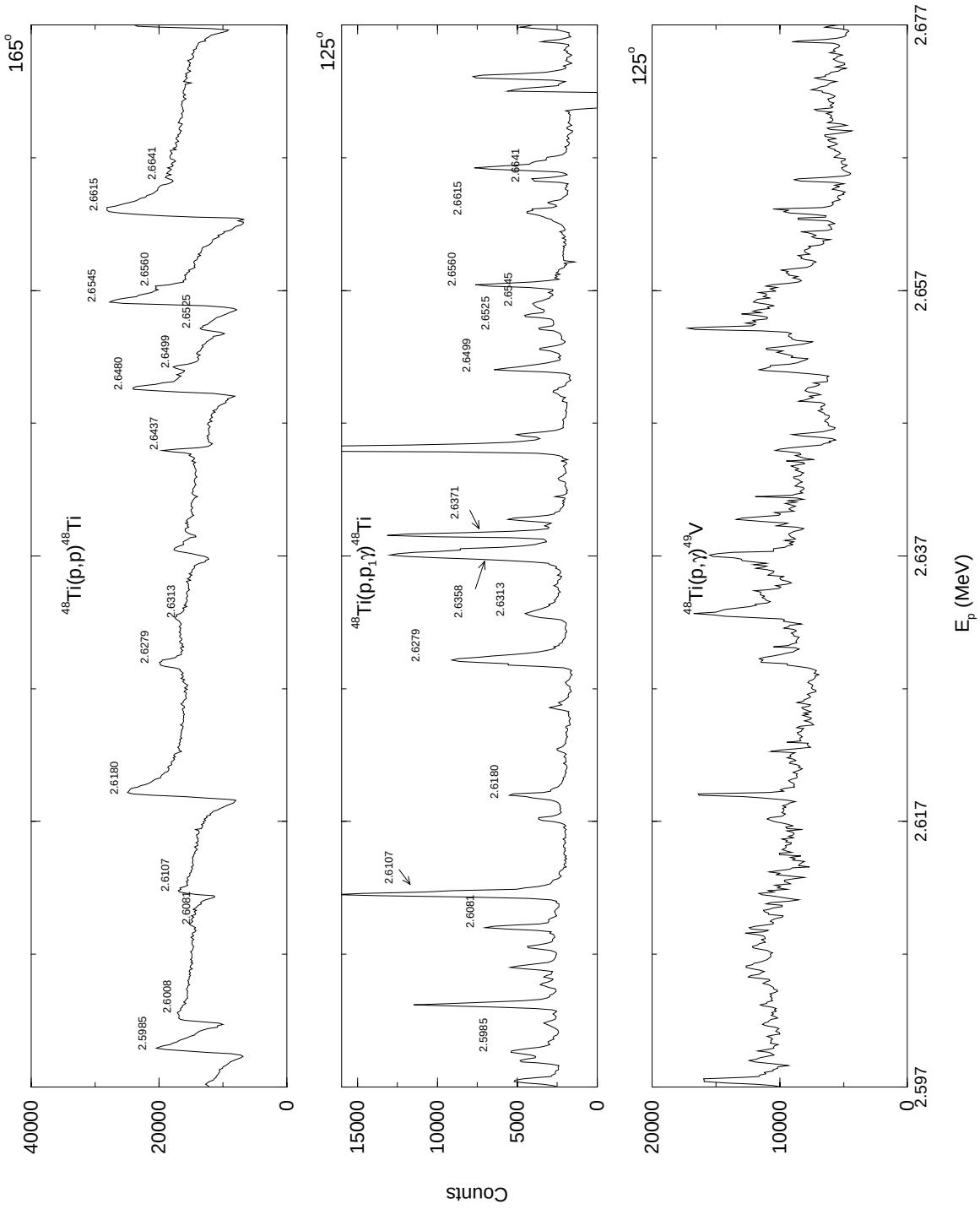

Figure E.7: Elastic, inelastic, and capture yield curves (top, middle, and bottom, respectively) for protons on ^{48}Ti in the energy region E_p = 2.5970 to 2.6770 MeV.

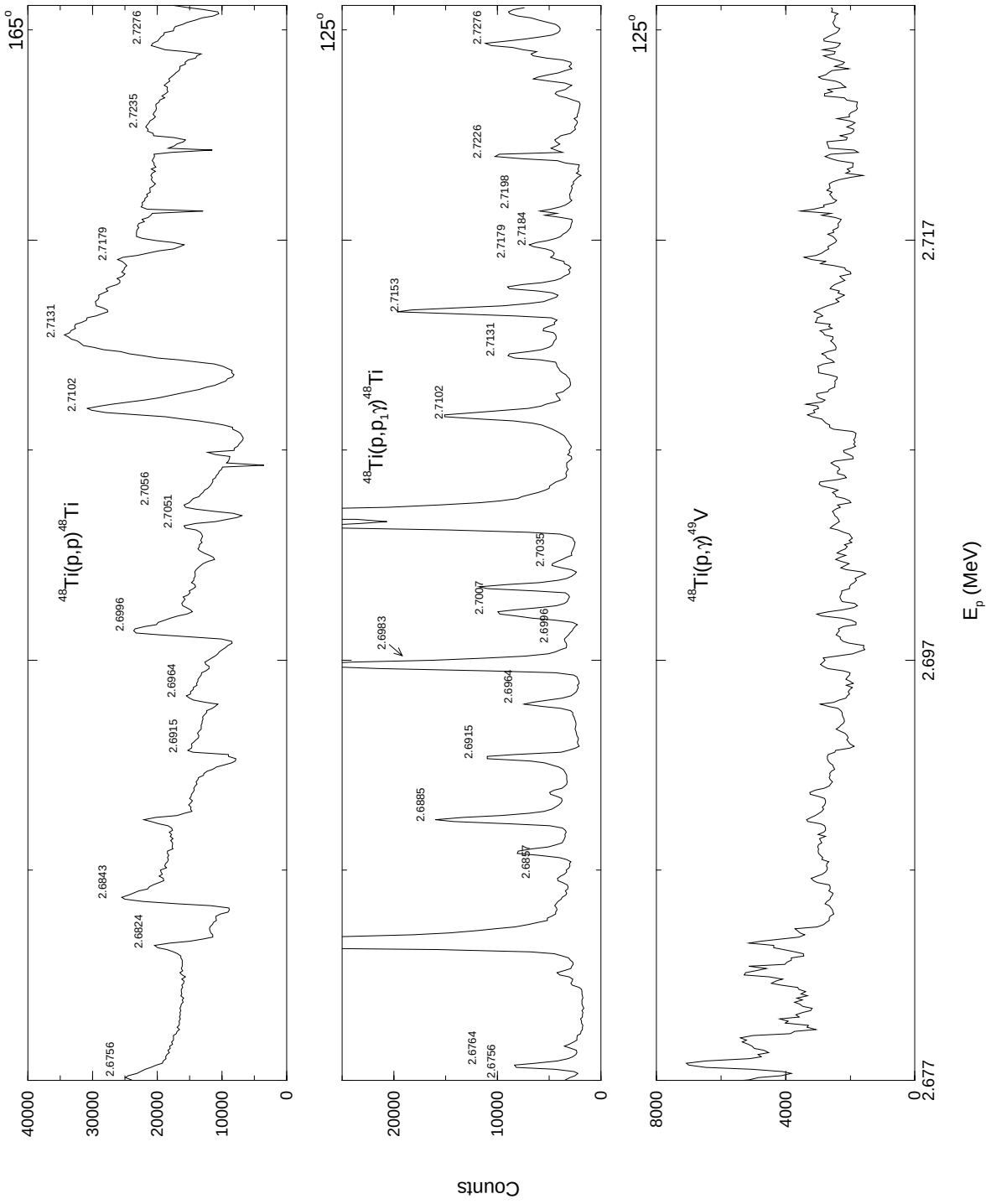

Figure E.8: Elastic, inelastic, and capture yield curves (top, middle, and bottom, respectively) for protons on ^{48}Ti in the energy region E_p = 2.6770 to 2.7281 MeV.

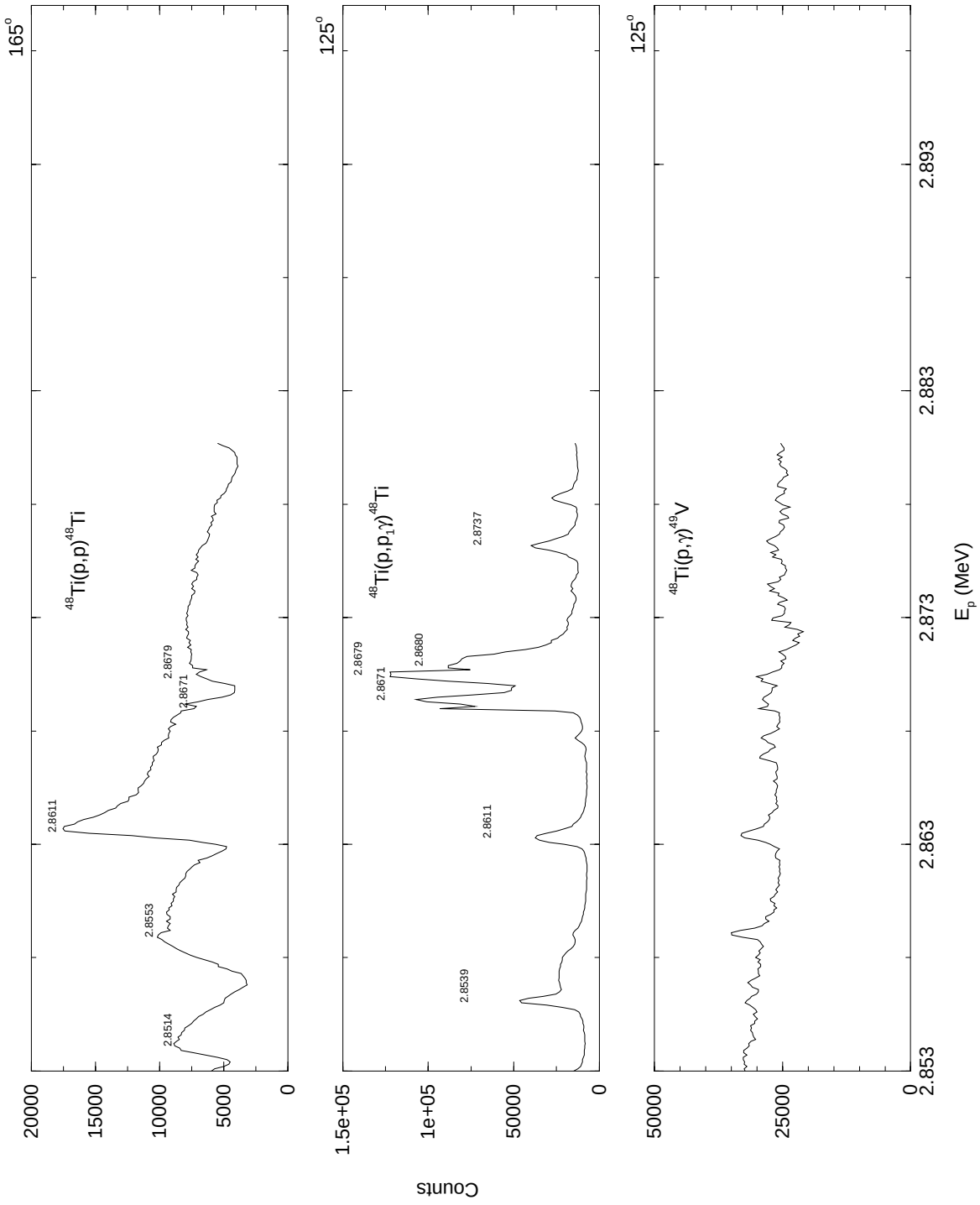

Figure E.9: Elastic, inelastic, and capture yield curves (top, middle, and bottom, respectively) for protons on ^{48}Ti in the energy region E_p = 2.8530 to 2.8805 MeV.